2011-07-21

Biomimetic Synthetic Tissue Scaffolds for Bone Regeneration: A Dissertation

Tera M. Filion Potts
University of Massachusetts Medical School

Let us know how access to this document benefits you.

Repository Citation

BIOMIMETIC SYNTHETIC TISSUE SCAFFOLDS FOR BONE REGENERATION

A Dissertation Presented
By

Tera Marie Filion Potts

Submitted to the Faculty of the
University of Massachusetts Graduate School of Biomedical Sciences, Worcester
in partial fulfillment of the requirements for the degree of

DOCTOR OF PHILOSOPHY

July 21nd, 2011

CELL BIOLOGY

BIOMIMETIC SYNTHETIC TISSUE SCAFFOLDS FOR BONE REGENERATION

A Dissertation Presented
By

Tera Marie Filion Potts

The signatures of the Dissertation Defense Committee signifies
completion and approval as to style and content of the Dissertation

Jie Song, Ph.D., Thesis Advisor

Paul Fanning, Ph.D., Member of Committee

Dale Greiner, Ph.D., Member of Committee

William Kobertz, Ph.D., Member of Committee

George Pins, Ph.D., Member of Committee

The signature of the Chair of the Committee signifies that the written dissertation meets
the requirements of the Dissertation Committee

David Ayers, MD, Chair of Committee

The signature of the Dean of the Graduate School of Biomedical Sciences signifies
that the student has met all graduation requirements of the school.

Anthony Carruthers, Ph.D.,
Dean of the Graduate School of Biomedical Sciences

Cell Biology

July, 21st and 2011

Abstract

Injury to bone is one of the most prevalent and costly medical conditions. Clinical treatment of volumetric bone loss or hard-to-heal bony lesions often requires the use of proper bone grafting materials, with or without adjuvant anabolic therapeutics. Despite significant problems associated with autografting (donor site morbidity, limited supplies) and allografting (disease transmissions, high graft failure rates) procedures, synthetic bone grafts remain the least utilized clinically. Existing synthetic orthopaedic biomaterials rarely possess a combination of bone-like structural and biochemical properties required for robust osteointegration, scalable and user-friendly characteristics indispensable for successful clinical translations. This thesis tests the hypothesis that by recapitulating key structural elements and biochemical components of bone in 3- and 2-dimensional biomaterials, scalable synthetic bone grafts can be designed to enable expedited healing of hard-to-heal volumetric bone loss. Specifically, FlexBone, a 3-dimensional hydrogel scaffold encapsulating 50 wt% of structurally well integrated nanocrylstalline hydroxyapatite, the main inorganic component of bone, was developed. The large surface area of nanocrystalline hydroxyapatite combined with its intrinsic affinity to proteins and its excellent structural integration with the hydrogel matrix enabled FlexBone to both sequester endogenous protein signals upon press-fitting into an area of skeletal defect and to deliver exogenous protein therapeutics in a localized and sustained manner. We demonstrated that FlexBone enabled the functional healing of critical-size long bone defects in rats in 8 – 12 weeks with the addition of a very low dose of osteogenic growth factor BMP-2/7. This promising synthetic bone graft is now being

explored for the delivery of multiple growth factors to expedite the healing of diabetic bony lesions. In addition, a 2-dimensional electrospun cellulose fibrous mesh was chemically modified with sulfate residues to mimic sulfated polysaccharide ECM components of skeletal tissues to enabled progenitor cell attachment and differentiation as well as controlled retention and localized/sustained delivery of protein therapeutics. This sulfated fibrous mesh is currently explored as synthetic periosteum to augment the osteointegration of devitalized structural allografts. Finally, a rat subcutaneous implantation model developed to examine the biocompatibility of newly developed biodegradable shape memory polymer bone substitutes is also presented.

Table of Contents

List of Figures

List of Tables

1

Chapter I: Introduction

This chapter has been adapted from the following published book chapter:

Filion TM and Song J. Scalable Functional Bone Substitutes: Strategic Integration of Key Structural Elements of Bone in Synthetic Biomaterials, Biomedical Engineering - Frontiers and Challenges, Reza Fazel-Rezai (Ed.), ISBN: 978-953-307-309-5, InTech, 2011.

1. Introduction

Over 40% of the disabling medical conditions of persons aged 18 years and over are musculoskeletal related. This number is even higher within the older population.[1] Surgical treatment for age-, trauma- or cancer-induced critical-size bone loss is particularly challenging. Current grafting material options for scaffold-assisted surgical repair of critical-size bone loss include autogenic bone grafts (autografts), allogenic bone grafts (allografts), and synthetic bone substitutes. Still considered the gold standard, autografts, retrieved from patients' own skeleton, are used in approximately 50% of all orthopedic bone grafting procedures. Complications arising from possible donor-site morbidity and insufficient grafting materials are major drawbacks of autografting procedures [2]. In addition, this option is highly limited within the aging population as the elderly are less likely to be qualified for such a procedure due to higher incidences of osteoporosis and metabolic diseases. Allografts, obtained from another human donor or animal cadaver, represent a useful alternate to autografts, and are used in approximately 40% of bone grafting surgeries. However, allografting procedures suffer from risks of rejection and disease transmission, as well as a significant structural failure rate of ~15 – 25% due to poor tissue integration, both structurally and biochemically.[2-6] These limitations, along with the growing aging population, has led to an increasing need for viable synthetic bone substitute alternatives.[7] Current clinically used synthetic bone grafts such as brittle ceramics and weak gel foams are used in only ~10% of all bone grafting procedures,[2] primarily due to their unstable graft fixation and insufficient tissue-graft

interactions.[4, 8-10] In the past two decades, many new synthetic bone grafts, designed to mimic key structural and biochemical properties of bone in order to enhance osteointegration and graft healing, have emerged in the literature. This rapidly evolving field has been extensively reviewed by others, including broad overviews of current requirements and techniques for preparing synthetic bone grafts,[7, 11] calcium phosphate–based bone substitutes,[12] polymeric bone substitutes,[13] and biomimetic nanocomposite orthopedic biomaterials.[14, 15] This introduction chapter highlights the evolvement of non-metallic orthopedic biomaterials from bioinert, biodegradable/bioresorbable, bioactive to tissue-responsive, and emphasizes the strategic integration of key structural elements of bone in the design of organic-inorganic composite bone substitutes with promising biomimetic and therapeutic properties. Within this dissertation, I illustrate the feasibility of accomplishing multifaceted functional requirements of viable synthetic bone substitutes by mimicking key extracellular components of bone.

2. Brief overview of the evolvement of synthetic orthopedic biomaterials

Most synthetic polymers traditionally used in orthopedic care, including poly(ethylene terephthalate) (PET) as implant coating, polyetheretherketone (PEEK) as spacers for cervical fusion, maxillofacial defect repair, and hip prostheses,[16-18] poly(methyl methacrylate) (PMMA) as bone cements, ultra high molecular weight polyethylene (UHMWPE) as total joint replacement components, and polysulfone (PSU) as internal

fracture fixators[12, 16, 19, 20] are considered bioinert. They are primarily designed to provide structural or mechanical support without eliciting significant immune responses. The primary drawback of bioinert implant materials is that they lack the intrinsic ability to promote osteogenesis, thus are unable to structurally or biologically integrate with the host tissue. To overcome such limitations, physical modification (e.g. increasing porosity) or blending bioinert materials with bioceramics or biodegradable polymeric components have been attempted.[20-25]

Calcium phosphate–based bioceramics have long been used clinically as bioactive bone fillers.[12, 26] They are known for good biocompatibility, osteoconductivity and easy surgical handling. However, these bone substitutes suffer from poor mechanical properties such as high brittleness and are often unsuitable for weight-bearing applications.[12, 27] Their integration with the more compliant polymeric matrices, therefore, has been under intense investigation.[28-31]

Biodegradable synthetic polymers have great potential as resorbable orthopedic implants and tissue scaffolds. The *in situ* generated porosity of degradable polymers, as a result of hydrolytic degradation, is thought to be beneficial to tissue penetration / osteointegration. In addition, the gradual resorption of biodegradable polymer-based orthopedic fixation devices, if timed to match with the tissue integration rate, could ensure adequate mechanical integrity at the site of implantation while potentially eliminating the need for a second surgery for implant retrieval. Among all degradable synthetic polymers,

poly(lactic acid) (PLA),[32] poly(glycolic acid) (PGA), poly(lactic-co-plycolic acid) (PLGA),[33-36] polyhydroxybutyrate (PHB),[37] polycaprolactone (PCL),[38] and their co-polymer blends[27] have been the most investigated.

Blending biodegradable polyesters with weakly basic osteoconductive minerals such as tri-calcium phosphate (TCP) or hydroxyapatite (HA) have been widely pursued as a strategy for further enhancing scaffold osteoconductivity, drug retention capacity, and for neutralizing acidic degradation products and mitigating inflammatory tissue responses.[19, 27, 39, 40] Achieving adequate structural integration between the organic matrix and the inorganic minerals, however, remains one of most significant challenges for the clinical translation of these polymer-mineral nanocomposites for orthopedic care. Loosely integrated ceramic particles could not only lead to inferior mechanical properties of the composite, but also cause ectopic bone formation in nearby soft tissues. This is because most polyesters are hydrophobic in nature and exhibit an intrinsically low affinity to bioceramics. Recent development of high-affinity HA-surface mineralization strategies applicable to hydrophilic hydrogels such as poly(2-hydroxyethyl methacrylate) (pHEMA) and pHEMA-based copolymers,[41-43] and identification of novel HA-binding/nucleating ligands, either small molecule-based[44, 45] or peptide-based,[46, 47] could help address this challenge.

The past decade has witnessed an increasingly elaborate trend in the design of bioactive synthetic biomaterials.[48] For bone tissue engineering applications, integrin-binding

peptide sequences for promoting cellular adhesion, phosphorylated ligands for promoting HA-mineralization, heparin-mimicking motifs for drug retention, and degradative enzyme substrate sequences have all been incorporated into multi-modality synthetic scaffold designs.[49-53] Of particular novelty is the design of self-assembling peptide-amphiphile (PA) gels by Stupp and coworkers for simultaneous presentation of cell adhesion peptide sequences, HA-mineral-nucleating sites, reversible crosslinking sites, and other therapeutic agents all within a single PA molecule that self-assembles and dissembles in response to environmental perturbations.[50, 54-56] Likely limitations of these unique PA gels include their relatively high manufacturing cost and low mechanical modulus which could limit their use to treatment of small non-weight bearing skeletal lesions. Another innovative concept introduced by Hubbell and coworkers was to induce scaffold degradation by using peptide substrates of the degradative enzymes matrix metalloproteinases (MMPs) as the chemical crosslinker of a non-fouling crosslinked hydrogel system.[52, 53] Given the elevated expression of some MMPs within both degenerative bony defects and arthritic knee joints, such a hydrogel system could be useful for bone and cartilage repair as the *in situ* increase of scaffold porosity in response to tissue microenvironment-specific enzymatic degradation could promote cellular infiltration and matrix deposition. The selection of MMP substrates with proper degradation kinetics matching with those of the matrix deposition rate, however, is not a trivial task.[57]

Despite the many exciting orthopedic biomaterials emerging in the literature, successful clinical translations are rare. The challenges lie in the difficulty in accomplishing the functional sophistication of viable synthetic bone substitutes (e.g. physical properties enabling easy surgical handling and stable graft fixation, structural and biomechanical properties facilitating its osteointegration, biocompatibility ensuring long-term safety) within an easy-to-fabricate biomaterial that can be reproducibly manufactured at low cost. Our laboratory, as well as some in the orthopedic biomaterials research community, believe that functional sophistication is not synonymous with complicated material designs.[10, 48] Instead, we believe that the key to meeting this challenge lies in the strategic integration of key structural elements of bone, which play multifaceted roles in defining the unique properties of the native tissue, in a low-cost biocompatible synthetic biomaterial.

3. Key structural elements of bone and their multifaceted functions

From a material's perspective, bone is an organic-inorganic composite comprising two major structural components that are hierarchically organized across various length scales: the calcium apatite crystals (primarily as substituted nanocrystalline hydroxyapatite, nHA, but also as crystalline precursors in lower quantities) and the type I collagen matrix [58]. The quantity and quality of the hard calcium apatite crystals (crystal size, maturity and structural integration with the collagen matrices) influence the

mechanical properties of bone.[59] For instance, the bending and compression strength of bone is known to positively correlate to bone mineral content.[60] In addition, bone minerals also support bone cell attachment, serve as an important reservoir of calcium and phosphate ions, and help retain the secreted factors that are indispensable in regulating the biochemical microenvironment of the bony tissue. Thus, HA has long been recognized as an important design element for tissue-engineered bone substitutes.[61] The intrinsic affinity of the dynamic apatite crystal surface for many acidic non-collagenous proteins widely found in calcified tissues[62-64] have also inspired the use of bioceramic scaffolds[65, 66] or polymer-bioceramics composite scaffolds[67, 68] to retain and deliver recombinant proteins for therapeutic use. Overall, HA has been explored for bone tissue engineering applications more as a way to enhance the mechanical strength than as a tool to mediate the biochemical properties of the scaffold.[10, 27] In general, the potential of the large surface areas provided by nHA as opposed to micrometer-sized HA for more efficient therapeutics delivery (e.g. higher retention capacity, more sustained release) has not been exploited to the fullest extent in the design of synthetic bone substitutes.

Type I collagen matrix of bone serves as a compliant template for the structural integration of the calcium apatite crystals, and, along with the mineral component, is responsible for defining the 3-dimensional structure as well as the strong, tough, yet relatively compliant mechanical properties of bone.[58, 69] In addition, it also interacts with many non-collagenous proteins and mediates cellular adhesion and functions.[70] The Gly-Pro-Hyp (Hyp: hydroxyproline) triplet repeats of type I collagen may also play an

important role in template-driven biomineralization. Recent discovery of novel HA-binding oligopeptides using the combinatorial phage display technique reveals a [Pro-(OH)-X] tripeptide pattern (OH: hydroxylated amino acid residues (Ser, Thr, Tyr); X: any amino acid) among the dominant HA-binding motifs.[46, 47] Such a hydroxylated tripeptide pattern resembles that of the type I collagen, underscoring the importance of hydroxylated residues in directing ligand-mineral interactions on a molecular level. These oligopeptides were shown to template the nucleation and growth of HA *in vitro*[46, 47] and may be useful in the design of synthetic polymer scaffolds, enabling template-driven mineralization of HA or the preparation of bulk organic-inorganic bone-like composites with improved interfacial binding affinity. We also showed earlier that polymeric hydrogels displaying hydroxylated (e.g. pHEMA) and acidic residues could be used to template the surface mineralization of HA with excellent interfacial adhesion strength,[41-43] further supporting the favorable interaction between the hydroxyls and the calcium ions. The strategy of modifying the surface of polymers or metallic substrates with hydroxylated or anionic coatings has also been pursued to facilitate the nucleation and growth of calcium apatite.[71, 72]

4. Synthetic bone scaffolds for the delivery of therapeutic agents

A multitude of proteins are known to play roles in the biological healing of bone, including in cellular recruitment and initiating the inflammation / bone remodeling

cascades.[73] Most scaffold-assisted bone repair would require the supplement of exogenous therapeutic agents such as osteogenic growth factors to augment the biological performance of biomaterial scaffolds. The therapeutic agents most commonly used clinically and in the literature to enhance bone repair are the Food and Drug Administration (FDA)-approved osteogenic growth factor bone morphogenetic protein -2 (BMP-2) and BMP-7.[74-76] In addition, vascular endothelial growth factor (VEGF),[77-80] receptor activator of nuclear factor kappa-B ligand (RANKL)[77] and transforming growth factor β (TGFβ)[81, 82] are also used to modulate the graft vascularization, osteoinegration and remodeling. Another recombinant factor that has gained quick attention within the bone tissue engineering community is BMP-2/7, a protein heterodimer of BMP-2 and BMP-7 that is more potent in inducing osteogenic differentiation of pluripotent cells *in vitro* than either homodimer alone.[83, 84] Its higher potency has been attributed to its decreased sensitivity to BMP inhibitors.[85] In particular, BMP-2/7 was found to have decreased sensitivity to Noggin, a BMP antagonist that is secreted from mesenchymal cells in response to BMPs to help control the rate of cellular differentiation. Noggin binds BMP, inhibiting BMP cell surface receptor binding; however, Noggin's binding affinity is lowered in the BMP-2/7 heterodimer. The high potency of BMP-2/7 has important clinical implications, including more cost-effective low-dose treatment with reduced systemic side-effects. A number of laboratories, including our own, have exploited the use of BMP-2/7 for augmenting scaffold-assisted repair of bone *in vivo*.[67, 86, 87]

Most existing biomaterials, however, are not designed for sufficient retention and/or controlled release of recombinant proteins, consequently requiring extremely high loading doses of these expensive agents.[65, 88] The excessive growth factors "burst" released from these scaffolds could cause a variety of adverse systemic side-effects, including ectopic bone formation and potential risks for cancers. Conversely, if the scaffold retains growth factors too tightly, healing may not be expedited. Therefore appropriate release kinetics that enable sustained and localized release of the therapeutic agents,[89] and ultimately lowers their critical loading doses[67, 68, 90, 91] and cost is highly desired.

Recent improvements in biomaterials' therapeutic delivery characteristics for bone repair were accomplished by incorporating nHA in polymeric hydrogel matrices, an approach that our lab has pursued,[91, 92] or by combining thin fibrous film-based physical barriers with 3-dimensional hydrogels[90] to enable the retention and release of growth factors in a more localized and sustained manner. Physical entrapment of therapeutic agents within MMP-degradable poly(ethylene glycol) (PEG)-based hydrogels is another innovative approach that has been established for therapeutic delivery by Hubbell and coworkers.[93] Another, more established, method for therapeutic delivery is the use of electrostatic interactions in hydrogels. For example, gelatin hydrogels can be basic and positively charged, or acidic and negatively charged depending on how the gelatin is extracted from collagen, thus can be designed to interact with a wide range of charged therapeutics.[94] Furthermore, therapeutic release kinetics can be modulated by the extent of gelatin cross-

linking, density, rate of degradation and scaffold porosity. Hyaluronic acid incorporation into hydrogels has also proven to be an affective method for not only therapeutic retention of proteins, such as BMP-2, but also for cellular adhesion, migration and proliferation, as well as binding to collagen and fibrin.[95-97] Sulfates have also been exploited for therapeutic retention. Hydrogels that incorporate negatively charged heparin sulfate can easily interact with many positively charged proteins, such as vascular endothelial growth factor (VEGF), fibroblast growth factor (FGF) and BMP-2.[95, 98, 99] Compared to the latter strategies, the incorporation of nHA has the added advantages of being able to retain and enrich endogenously secreted factors due to its intrinsic affinity to the factors residing in the bony tissue environment and its large surface area available for absorption. This is a key strategy that this dissertation will exploit.

5. Complimentary synthetic scaffolds: 2-Dimensional vs. 3-Dimensional

While biomaterials for bone repair can be enhanced by the addition of exogenous therapeutics, they can also benefit from exogenous cells (e.g. mesenchymal stem cells, hematopoietic cells, osteoblasts) pre-seeded on the biomaterial scaffolds.[100] Functionalization of biomaterials with integrin binding peptides such as RGD, and mimetics of extracellular matrix components, such as collagenous protein mimetics, have been used to improve cellular attachment of both endogenous cells and pre-seeded exogenous cells.[93, 101] In addition, cellular fate (e.g. stem cell differentiation) is also

known to be profoundly impacted by the chemical, structural and mechanical properties of the biomaterials.[102, 103] Overall, materials possessing the ability to support cellular encapsulation (e.g. 3-D constructs) or surface attachment (e.g. 2-D films or fiber meshes) and that favor specific stem cell differentiation pathways, in addition to the ability to act as a therapeutic delivery vehicle, are attractive for bone repair.

Both 3-D and 2-D constructs have been explored towards this goal,[104-106] although greater focus has been placed on engineering 3-D scaffolds. Among the 2-D platforms explored, a focus has been centered on supporting cellular attachment and differentiation (due to the relative ease of cell attachment on 2-D compared to 3-D scaffolds), as well as delivery of osteogenic factors in culture.[38, 107-109] The unique handling characteristics of 2-D scaffolds could enable versatile *in vivo* uses, including as a stand-alone graft overlying a fracture, a filler being press-fit into an area of small bony defect, or a synthetic membrane wrapped around a 3-D bone graft (Fig. 2.4). The combination of 2-D and 3-D constructs has recently been explored by Robert Guldberg and colleagues to achieve spatio-temporal control of growth factor release profiles,[81, 110] and by others to create hierarchical composites.[111] From a biomimetic perspective, 2-D scaffolds that can be wrapped around a 3-D bone scaffold, if engineered properly, can recapitulate some of the important functions of periosteal tissues surrounding long bone in harboring stem cell and directing their differentiation upon injury. This scenario, as depicted in Figure 1, offers a unique opportunity to create a spatial and kinetic hierarchy to deliver multiple therapeutics and/or support adhesion of different cell types at the interface of the 2-D and

3-D graft components. For example, BMP-2 is known to play a critical role in initiating early bone healing,[112] while BMP-7 may be more suitably used for stimulating later stages of bone healing.[113, 114] One could envision using a 3-D scaffold designed for slower release of BMP-7 in combination with a 2-D scaffold designed for faster release of BMP-2. Alternatively, different cell types could be seeded on each construct, such as seeding bone marrow-derived stem cells on the 2-D construct to more efficiently initiate graft healing while seeding hematopoietic stem cells on the 3-D construct to promote the vascularization of the graft for better tissue incorporation. In cases where the 3-D grafts (i.e. allografts) cannot readily support the seeding of exogenous cells, a cell-laden 2-D construct could be readily wrapped around the 3-D graft.
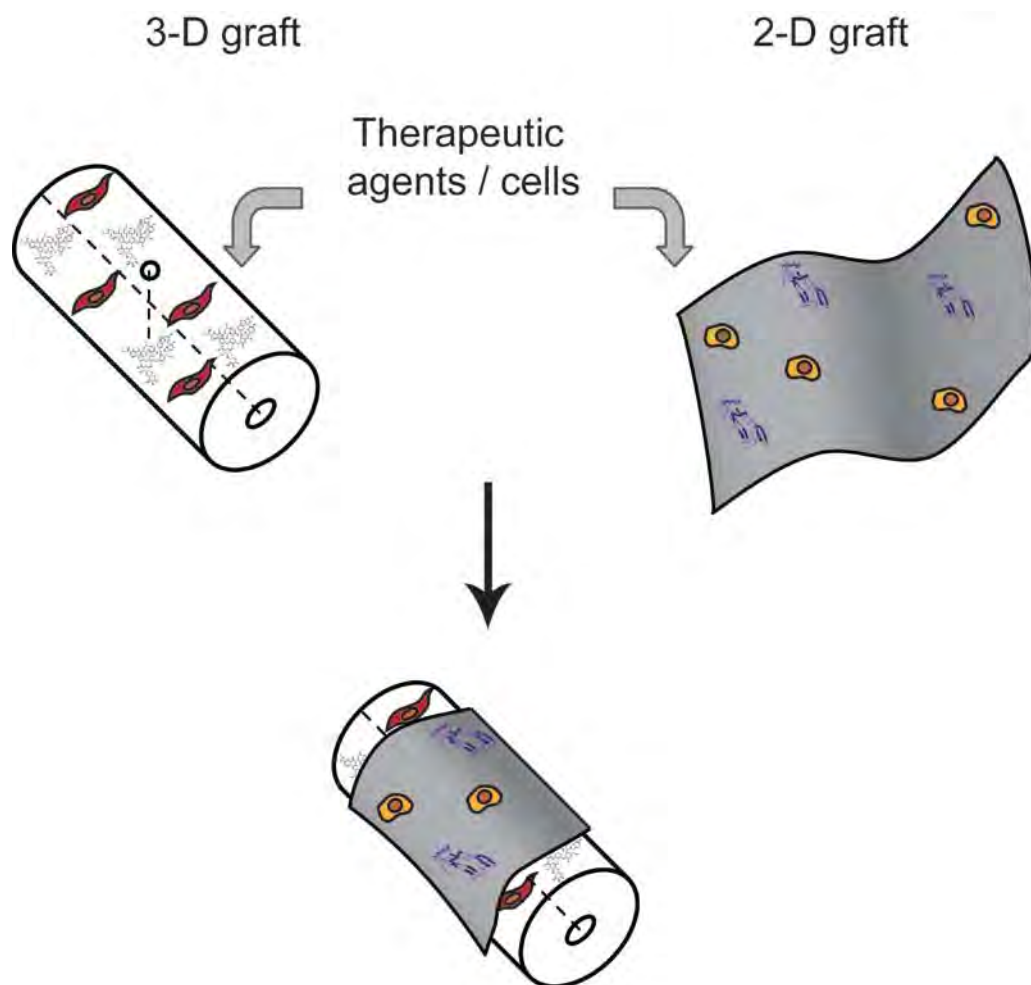
Figure 1.1. Cartoon depiction of complementary 3-D and 2-D grafts.

A common method for preparing a 2-D fibrous mesh scaffold with controlled fiber dimension, mesh thickness and porosity is by electrospinning. When the polymer fibers are properly chosen, they can be subjected to further chemical modifications to render specific biological properties and/or mechanically strengthened to improve their handling characteristics.[115-117] This is another area that this dissertation will focus on.

6. Overview of dissertation content

The central theme of this dissertation is the development of scalable 2-D and 3-D scaffolds for facilitating the repair of critical-size bone defects.

Chapter 2 will focus on FlexBone, a 3-D elastomeric composite bone substitute integrating hydroxylated biocompatible pHEMA hydrogel with 50 wt% of nHA. The design was inspired by the multifaceted roles of nHA in defining the unique structural, mechanical and biochemical properties of bone. Here we show that FlexBone can enable either functional repair of critical-size femoral defects in rats with the addition of a very low dose of rhBMP-2/7, and partial healing in the absence of exogenous therapeutics in 8-12 weeks.

Chapter 3 will focus on the development and characterization of a 2-D electrospun sulfated cellulose fibrous mesh for use as a delivery vehicle for growth factors and as a

platform for supporting the attachment and differentiation of bone marrow derived mesenchymal stem cells (MSC). The chemical design of this construct was inspired by sulfated polysaccharides which are known for their high affinity for many protein signals within the extracellular matrix environment of bone and cartilage tissues. We show that this mesh can support cellular attachment and differentiation of MSCs to osteogenic lineage, and can act as a suitable delivery vehicle for protein therapeutics.

Chapter 4 will examine the biocompatibility of a biodegradable, thermal-responsive shape memory polymer (SMP) scaffold developed in our laboratory, for use in minimally invasive surgical applications. Using a rat subcutaneous implantation model, we established the *in vivo* degradation profile of this class of SMP as a function of the biodegradable polyester chain length, and demonstrated that these materials and their degradation products exhibited immunogenicity similar to those of polylactide (resorbable suture) controls. The methods used in this study can be extended for the characterization of the biocompatibility of other novel synthetic orthopaedic biomaterials.

Chapter 5 will conclude the thesis with some ongoing work highlighting the future directions of applying FlexBone to the treatment of hard-to-heal diabetic bony defects and the 2-D sulfated fibrous mesh as synthetic periosteum to augment the healing of structural allografts or 3-D synthetic bone grafts.

Chapters 2, 3 and 4 are based on my first-authored publications resulting from my dissertation research. The appendix section will include a list of my other co-authored publications as well as a first-authored publication on a different topic, all accomplished during my graduate school career.

Chapter II: Elastomeric osteoconductive synthetic scaffolds with acquired osteoinductivity expedite functional repair of critical rat femoral defects

This chapter has been adapted from the following published manuscripts:

Song J, Xu J, <u>Filion T</u>, Saiz E, Tomsia AP, Lian JB, Stein GS, Ayers DC, Bertozzi CR. Elastomeric high-mineral content hydrogel-hydroxyapatite composites for orthopedic applications. J Biomed Mater Res A., volume: 89A, Issue: 4, pages 1098-1107, 2009.

<u>Filion TM</u>, Li X, Kreider JM, Goldstein SA, Ayers DC, Song J. A Synthetic Alternative to Structural Bone Allograft. Elastomeric osteoconductive synthetic scaffolds with acquired osteoinductivity expedite the repair of critical femoral defects in rats. *Tissue Eng. Part A,* volume: 17, issue: 3-4, pages 503-511, 2011.

Abstract

Regenerative medicine aspires to reduce reliance on or overcome limitations associated with donor tissue-mediated repair. In orthopedic care, the prevalently used structural bone allografts are known for failures due to poor tissue integration. This problem is aggravated among elderly, those suffering from metabolic conditions, or those undergoing cancer therapies that compromise graft healing. Towards this end, we developed a synthetic graft named FlexBone where nanocrystalline hydroxyapatite (nHA, 50 wt%) was structurally integrated with crosslinked poly(hydroxyethyl methacrylate) hydrogel that provides dimensional stability and elasticity. It recapitulates the essential role of nHA in defining the osteoconductivity and biochemical microenvironment of bone due to its affinity for biomolecules. Here we demonstrate that FlexBone effectively absorbed endogenously secreted signaling molecules associated with the inflammation/graft healing cascade upon being press-fit into a 5-mm rat femoral segmental defect. Furthermore, when preabsorbed with a single dose of 400-ng rhBMP-2/7, it enabled the functional repair of the critical-sized defect by 8-12 weeks. FlexBone was stably encapsulated by the bridging bony callus while the FlexBone-callus interface was continuously remodeled. In summary, FlexBone combines the dimensional stability and osteoconductivity of structural bone allografts with desirable surgical compressibility and acquired osteoinductivity in an easy-to-fabricate and scalable synthetic biomaterial.

Introduction

Synthetic scaffolds designed to assist tissue repair should exhibit useful surgical handling characteristics, biochemical microenvironment promoting proper cellular response and tissue integration, and structural/chemical properties ensuring long-term stability and safety. Existing clinical synthetic bone substitutes (e.g. brittle ceramics, weak polymer gel foams) rarely possess essential bone-like structural and biochemical properties. In addition, they often lack desirable physical properties facilitating convenient surgical insertion / stable graft fixation or generate immunogenic/inflammatory degradation products *in vivo*. In fact, in orthopedic care, no single synthetic scaffold can yet meet the multiple requirements to functionally replace/outperform structural bone allografts. There is a huge disconnect between the many proof-of-concept synthetic bone substitutes reported in literature and the translation of these materials into clinical practice.[9] The over-reliance of existing scaffolding materials and the sub-optimum methods for delivering therapeutics fail to enable sufficient integration of these materials with host bone or generate new bone structure *in vivo*. On the other hand, the many exciting new biomaterial scaffolds emerged from academic labs often fail to address the high manufacturing cost associated with the complicated engineering design, which is a major hurdle in their bench-to-bedside translations. In contrast, FlexBone, with nHA structurally integrated within a crosslinked carbon network that is not hydraulically degradable, can withstand repetitive functional-compressive loads with excellent shape recovery under physiological conditions.[118] As a result of the high surface area of the nHA component and its intrinsic affinity for proteins

and small molecule therapeutics,[63, 64] FlexBone is also a suitable vehicle for delivering growth factors and antibiotics in a sustained and localized manner *in vitro* (Fig. 2.2).[68] FlexBone is also scalable, and easy and inexpensive to prepare. In this study, we test the hypothesis that the elasticity, osteoconductivity, and dimensional stability exhibited by FlexBone, combined with its osteoinductivity acquired from preabsorbed bone morphogenetic protein-2/7 heterodimer (rhBMP-2/7), makes it an effective scaffold in enabling the functional repair of critical femoral defects in rats.

A 5-mm rat femoral segmental defect model[119] was chosen to evaluate the efficacy of FlexBone in facilitating the repair of the critical defect due to its non-healing nature in the absence of proper intervention. In addition, the periosteum of the cortical bone adjacent to the femoral defect was circumferentially removed to emulate challenging clinical scenarios where this important source of progenitor cells and growth factors for bone regeneration is lost. FlexBone with a given mineral composition, 50wt% nHA (FB-50), or 25wt% nHA plus 25wt% tricalcium phosphate (TCP) (FB-25-25), with or without pre-absorbed rhBMP-2/7, was press-fit into the defect. BMP-2 and BMP-7 are both FDA-approved protein therapeutics for promoting skeletal repair.[120] BMP-2 plays a critical role in initiating fracture healing,[112] and is clinically used for tibial fractures and spinal fusions. BMP-7 may play a larger role in the later stages of bony repair,[113, 114, 121] and is routinely used for spinal fusions and non-unions. It has also been used in revision surgeries following inadequate repairs by BMP-2 treatment. Here we hypothesize that rhBMP-2/7 heterodimer could be more effective than either homodimer in augmenting the osteointegration and graft healing of FlexBone. The graft healing as a function of

mineral composition and growth factor treatment was monitored by radiography and histology for 12 weeks. Functional repair of the defect was assessed by end-point micro-CT analyses and torsion tests.

Methods

Graft Preparation

FlexBone with two mineral compositions, 50wt% nHA (FB-50) or 25wt% nHA-25wt% tricalcium phosphate (TCP) (FB-25-25), were prepared to examine the potential impact of the faster dissolution of TCP[122] on graft remodeling. FB-50 and FB-25-25 were prepared as previously described,[118] in rigid acrylic tubing of an inner diameter of 3.2 mm (United States Plastic Corp.; tubes were washed with absolute ethanol to remove radical inhibitors, and air-dried prior to use). The retrieved cylindrical FlexBone was cut into segments ~ 5.5 mm in length, and drilled with 2 intersecting orthogonal drill holes (a longitudinal channel 1.19 mm in diameter and an orthogonal channel 0.79 mm in diameter as illustrated in Fig. 2.4A) to allow bone marrow access upon implantation. FlexBone was then thoroughly equilibrated in MilliQ water to remove residual radical initiators, unreacted monomers, ethylene glycol, and debris from the drilling. After being sterilized with 70% ethanol, FlexBone was dried for storage. Prior to surgical implantation, FlexBone was hydrated with saline for ~0.5 h (Fig. 2.3) before an additional 8-μL saline or reconstituted rhBMP-2/7 solution (R&D Systems) was uniformly applied to give a final loading dose of 0 or 400-ng rhBMP-2/7 per graft.

Rat bone marrow stromal cells (MSC) attachment and differentiation on FlexBone using a rat subcutaneous implantation model

MSC were isolated from long bones of 4-week old male Charles River SD strain rats. Briefly, marrow was flushed from femur with a syringe. After lysing red blood cells with sterile water, the marrow cells were centrifuged and resuspended in minimum essential medium (MEM) supplemented with 20% FBS, 0.2% penicillin-streptomycin and 1% L-glutamine, and passed through a sterile metal filter. Cells were expanded on tissue culture plates (10 million cells per 100-mm plate initial seeding density) with media change on day 4 and every other day thereafter before they were lifted off for plating on FlexBone.

Thin half discs (7 mm in diameter, 1 mm in thickness) of FlexBone containing 40% nHA were sterilized in 70% ethanol, re-equilibrated with sterile water before being seeded with MSC and used for subcutaneous implantation in rats. Fifty microliters of MSC suspension (in culture media described above) was loaded on the surface of thin disks of FlexBone to reach 5,000-cells/cm^2 or 20,000-cells/cm^2 seeding density. The cell-seeded FlexBone were incubated at 37 °C in humidified environment with 5% CO2 without additional media for 6 h to allow cell attachment to the FlexBone substrate. Additional media were then added and the cells were cultured on the substrates for 2 days before being used for implantation. Four sets of samples were used for each cell seeding treatment. Thin discs of FlexBone without pre-seeded MSC were also used for

implantation as controls. Rats were anesthetized by intraperitoneal (IP) injection of ketamine / xylazine (50 mg / 5 mg per kg). They were shaved and swabbed with betadine before two 1/4" bilateral skin incisions were made over the rib cage for insertion of the FlexBone discs with and without preseeded MSC. The skin was closed with surgical staples and buprenorphine (0.02 mg/kg) was given subcutaneously. The rats were sacrificed by CO_2 inhalation and cervical dislocation at day 14 and day 28 for the retrieval of FlexBone. After removing the fibrous tissue encapsulation, the retrieved FlexBone was fixed in 4% paraformaldehyde (0.1 M phosphate buffer, pH 7.4) for 5 h at 4 ℃ before being analyzed by SEM, XRD, and histology.

Environmental Scanning electron microscopy (ESEM)

The microstructures of the composites were characterized using environmental scanning electron microscopy (ESEM) on a Hitachi S-4300SEN microscope (Hitachi, Japan). The chamber pressure was kept ~35 Pa to avoid complete sample dehydration and surface charging during the observation.

X-ray powder diffraction (XRD)

The crystalline phases of the mineral in the FlexBone composites before and after

subcutaneous implantation in rats were evaluated by XRD with a Siemens D500 instrument using Cu Kα radiation. Phases were identified by matching the diffraction peaks to the JCPDS files.

In vitro characterization of the release of rhBMP-2/7 from FlexBone (FB-50) using the C2C12 osteogenic trans-differentiation culture model

The ability of FB-50 to locally release pre-absorbed rhBMP-2/7 in a sustained manner was examined as previously described for FB-25-25.[68] Briefly, mouse myoblast C2C12 cells were seeded at 5,000 cells/cm^2 in a 24-well plate in expansion media (DMEM, 10% FBS, 1% Pen-Strep) and allowed to adhere overnight. The culture was then continued in low mitogen media (DMEM, 5% FBS, 1% Pen-Strep), with a cylindrical FB-50 graft pre-loaded with 40-ng rhBMP-2/7 (R&D Systems) added to each well (n=3 per experimental group). Positive control wells were supplemented with 40-ng/well rhBMP-2/7 without a graft carrier. Cultures were continued for 3 or 4 days without media change, before the graft was removed and the cells were stained for ALP, a marker of osteogenic differentiation, using a leukocyte alkaline phosphatase kit (Sigma Aldrich). In a subset of experiments, grafts retrieved after 4-day culture were placed into fresh wells of C2C12 culture for 3.5 days to assess long-term sustained release of rhBMP-2/7 from the FlexBone grafts. As shown in Fig. 2.2, the release of rhBMP-2/7 from FB-50 was achieved in a localized manner over 7 days, similar to that observed with FB-25-25.[68]

Water uptake of freeze-dried FlexBone over time and determination of the proper loading volume of rhBMP-2/7 solution per graft

To enable convenient surgical press-fitting of FlexBone graft (FB-25-25 or FB-50) into the 5-mm rat femoral defect, freeze-dried grafts must be partially hydrated to render necessary elasticity while still leaving enough room for absorbing rhBMP-2/7 solution prior to implantation. To determine the optimal hydration time and proper loading volume of rhBMP-2/7 solution to be applied to each graft prior to implantation, freeze-dried FB grafts were first hydrated in water over 3.5 days to determine their water uptake profiles over time (Fig. 2.3). Pre-weighed, freeze-dried grafts (FB-25-25 and FB-50, dimension shown in Fig. 2.4A) were placed in deionized water and retrieved every half hour for weighing. The grafts placed in water for 3.5 days were considered to be fully hydrated. As shown in Fig. 2.3, each freeze-dried FlexBone graft could absorb >20-µL water when fully hydrated (3.5 days in water), with half of this volume absorbed by the graft in the first 30-min exposure to water. We thus chose to hydrate freeze-dried FlexBone grafts for 0.5 h prior to the surgery, and the rhBMP-2/7 (400 ng) was loaded to the partially hydrated FlexBone in 8-µl loading volume immediately before the press-fitting of the graft into the defect.

Femoral segmental defect model – study design and surgical procedure

A 5-mm rat femoral segmental defect model[119] (Fig. 2.4B) was chosen to evaluate FlexBone-mediated skeletal repair as a function of mineral composition and osteogenic growth factor delivery. Four groups of FlexBone grafts (FB-50 and FB-25-25, with or without 400-ng rhBMP-2/7) were press-fit in 5-mm rat femoral defects, and the osteointegration of the grafts were examined over time. A no-graft control group was used to ensure the non-healing nature of the 5-mm defect without graft treatment. The rats were euthanized at 4 days, 2, 4, 6, 8 and 12 weeks for histological examination. In a subset of 8- and 12-week rats, fresh frozen explanted femurs were evaluated by microCT and then tested to failure in torsion. A total of 140 defects were generated: 5 groups (4 exp. groups + 1 no-graft control group)×[6 time points×3(N = 3, histology)+2 time points×5(N = 5, MicroCT & torsion test)] =140 defects. Four intact femurs were collected for torsion from healthy un-operated rats that were of the same age as the rats receiving the grafts for 12 weeks.

All animal procedures were approved by the University of Massachusetts Medical School Animal Care and Use Committee. Briefly, sedated male Charles River SASCO-SD rats (289-300 g) were maintained by 2% isoflurane-oxygen throughout the surgery. The shaft of a femur was exposed by a combination of sharp and blunt dissections and the periosteum of the exposed femur was circumferentially removed to emulate a challenging clinical scenario where this important source of progenitor cells and signaling molecules is lost. A radiolucent PEEK internal plate fixator was secured to the exposed femur with 4 bicortical screws into pre-drilled holes. A 5-mm mid-diaphyseal defect was then

created using an oscillating Hall saw with parallel blades (Fig. 2.4B). The defect site was thoroughly irrigated with saline to remove bone debris and residue detached periosteum before it was press-fit with a FlexBone graft with or without 400-ng rhBMP-2/7. The wounds were closed with sutures and the rats were given cefazolin (20 mg/kg) and bupenorphine (0.08 mg/kg) injections subcutaneously over the next 2 days. Rats were radiographed post-op to ensure proper graft positioning, and every 2 weeks thereafter to monitor the mineralized callus formation over time. On dates of scheduled explant retrieval, rats were sacrificed by isoflurane and cervical dislocation. The repaired femur, with the PEEK plate fixator intact, was carefully separated from the adjacent hip and knee joints by an oscillating saw.

Histology and Microscopy

To evaluate cellularity, new bone formation, remodeling and vascularization of the FlexBone over time, histochemical and immunohistochemical staining of the explants for hematoxylin and eosin (H&E), osteogenic differentiation marker alkaline phosphatase (ALP), osteoclast lineage marker tartrate-resistant acid phosphatase (TRAP), and chondrocytes (by toluidine blue) were performed on 6-μm paraffin sections. All explanted femurs were fixed in a periodate-lysine-paraformaldehyde fixative[123] at 4 °C for 2 days, and decalcified in 18% EDTA (0.1 M Tris, pH 7.0) at 4 °C for 4 weeks before they were bisected longitudinally for paraffin embedment and sectioning. Polarized light

microscopy was used to assess the orientation of collagen fibrils and thus the maturity of new bone formation.

Quantification of bone remodeling activities at the FlexBone-callus interface as a function of time and growth factor treatment

The active bone remodeling which occurred at FlexBone-callus interface was quantified as the number of nuclei from TRAP positive cells (osteoclastic activity) and the number of nuclei from ALP positive cells (osteoblastic activity) detected along each millimeter of FlexBone-callus interface (within 100-μm thickness of the callus adjacent to the implant surface). Reporting of the number of nuclei of TRAP positive cells was chosen over the determination of the number of osteoclasts due to the difficulty in discerning the whole contour of the multinucleated cells as the sectioning often sliced through these cells. For each graft treatment at 2 and 6 weeks, 7-9 consecutive 200× fields of view (FOV) across the length of the external callus-FlexBone interface were examined with ALP/TRAP-stained and corresponding H&E stained tissue sections. Counts in all FOVs were averaged and reported as mean+/-standard deviation per 0.1mm^2 rather than summed as a whole to reflect the heterogeneity of bone remodeling activity along the graft-callus interface.

Detection for endogenous proteins absorbed on FlexBone

FB-50 grafts and un-mineralized pHEMA controls were press-fit into the 5-mm critical-size rat femoral defects in a subset of experiment. The grafts were harvested and fixed at 0.5 hours, 1 day, 2 days, 4 days, and 1 week, during which the inflammatory/graft healing cascade was initiated. Antibodies for TGFβ (detects precursor and mature TGFβ1, 2 and 3 isoforms; Santa Cruz, Santa Cruz, CA), TNF-α (Novus Biologicals, Littleton, CO), IL-1β (Santa Cruz), VEGF (Santa Cruz), RANKL (Abcam, Cambridge, MA), BMP-2 (Novus Biologicals), BMP-7 (Abcam), and SDF-1 (Santa Cruz) were used to detect the endogenous proteins absorbed on FB-50 and pHEMA at each time point. Unimplanted FB-50 were stained for the same panels of antibodies and IgG isotype (rabbit or mouse IgG) control stains were performed on all FB-50 explants retrieved at various time points (Fig. 2.7). For the TGFβ detection, positive control stain was performed on a FB-50 graft loaded with 10-ng rhTGFβ1 (R&D systems), and negative control stain using the blocking peptide (Santa Cruz) along with the primary antibody was also carried out. The immunohistochemical detection was performed on paraffin embedded sections as described above.

MicroCT and Biomechanical Tests

Fresh frozen explants were scanned on a cone-beam eXplore Locus SP microCT system. The effective voxel size of the reconstructed images was 18×18×18 μm^3. Images were globally thresholded and analyzed to measure bone to callus volume and bone mineral content. Both ends of the same explants were then potted in aluminum pots with molten bismuth and mounted in a custom mini-torsion tester. PEEK fixators were carefully bisected using a high speed burr under irrigation before the explants were loaded to failure (0.5°/sec) to determine failure torque and energy to failure.

Statistical analyses

The Wilcoxon-Mann-Whitney ranked-sum test was used to make all statistical comparisons and p-values < 0.05 were considered significant. All analyses were performed using STATA (version 9.0) software.

Histological examination of vital organs retrieved 12 weeks post-op

To identify potential adverse systemic effect of the implanted FlexBone grafts on vital organs, heart, kidney, liver and lung tissues were retrieved from the sacrificed rats 12 weeks post-op (with or without the implantation of FlexBone) and fixed in a

periodate-lysine-paraformaldehyde fixative[123] at 4 °C for 2 days before they were paraffin-embedded, sectioned and stained for H&E.

Results

In vivo osteogenic differentiation of bone marrow stromal cells (MSC) supported by FlexBone

To test the cytocompatibility and the *in vivo* resorption of FlexBone, we seeded hydrated composites with MSC isolated from rat femurs, and implanted them subcutaneously (SC) in 4-week old male Charles River SD strain rats. The composites were retrieved at 14 and 28 days, with a degree of fibrous tissue encapsulation observed in all cases. After removing the fibrous tissue, the morphology and mineral phase of the retrieved implant were examined by SEM and X-ray powder diffraction. Little macroscopic change in shape or size of the retrieved FlexBone was observed, reflecting the non-degradable nature of the hydrogel scaffold that defines the overall shape of the composite. However, surface roughening was observed with both 14- and 28-day explants regardless whether they were pre-seeded with MSC prior to implantation (Figs. 2.1A & 2.1B). This is likely a combined outcome of slow dissolution of the mineral component and the extracellular matrix deposition from cells either pre-seeded on or newly attracted to the substrate *in vivo*. XRD analyses performed with the explanted composite (Fig. 2.1C) revealed a diffraction pattern matching with that of the nHA powder, suggesting that the major mineral phase remained unchanged 4 weeks after the SC implantation. To determine whether the composite can support the osteogenic

differentiation of MSC *in vivo*, the explanted composites with pre-seeded MSC were stained histochemically for alkaline phosphatase (ALP) activity, a marker for osteogenic differentiation.[124] To avoid the harsh paraffin embedding conditions that may compromise ALP enzymatic activity,[125] frozen sectioning was performed on the explants prior to ALP staining. As shown in Figure 4D, ALP activity (indicated by red stains) was detected 14 days post-implantation on the periphery of the FlexBone pre-seeded with 5000-cells/cm^2 MSC. More extensive ALP activity was also detected 28 days after the implantation on FlexBone pre-seeded with 20,000-cells/ cm2 BMSC. These data suggest that FlexBone was able to support the attachment and *in vivo* osteoblastic differentiation of osteoblast precursor cells.
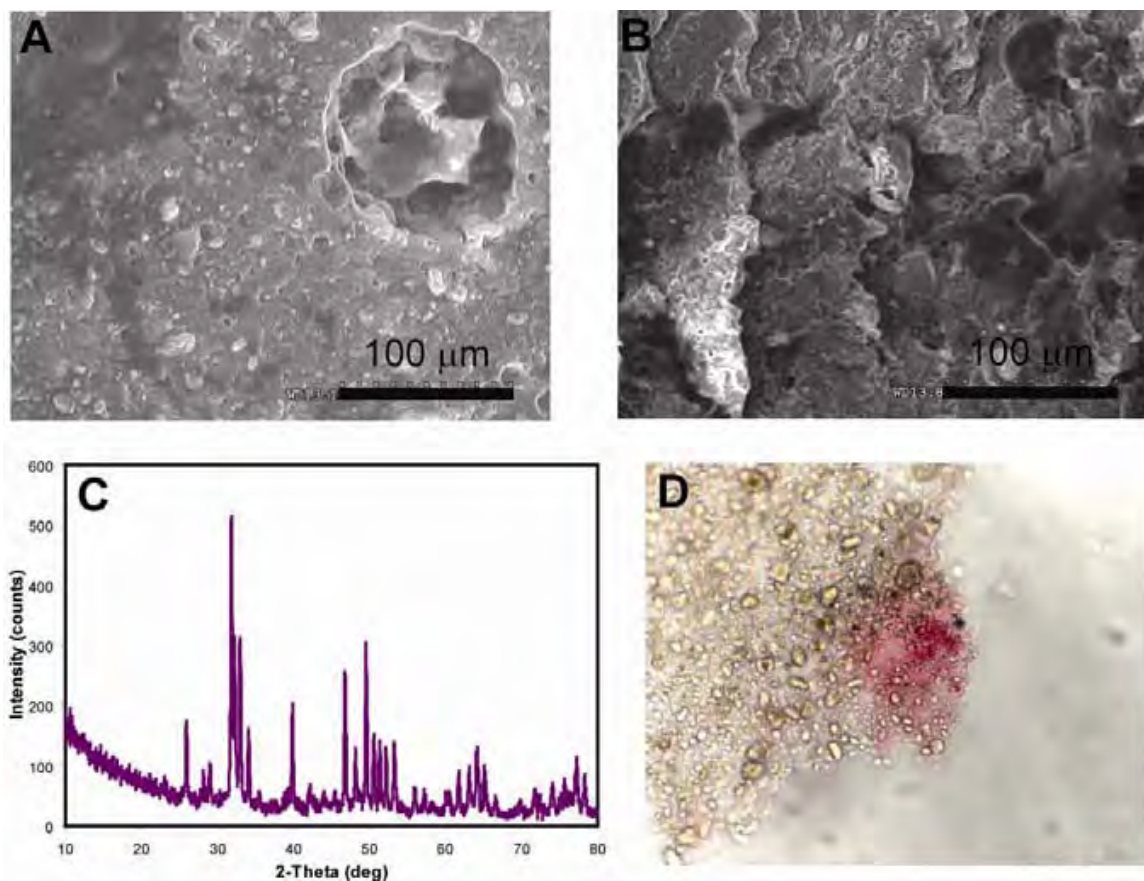
Figure 2.1. *In vivo* resorption and osteogenic differentiation of bone marrow cells supported by FlexBone. (A) SEM micrograph of a composite (pre-seeded with 20,000-cells/cm^2 MSC) retrieved 28 days after SC implantation in rat; (B) SEM micrograph of a composite (without pre-seeded MSC) retrieved 14 days after SC implantation in rat; (C) XRD of the explanted sample shown in (A), with diffraction patterns matching with that of the nHA powder; (D) ALP staining (red) of a 12-µm frozen section of an explanted composite (pre-seeded with 5,000-cells/cm^2 MSC) on day 14. Magnification: 400×.

Partial healing of femoral critical defects by FlexBone in the absence of exogenous growth factors.

Elastomeric FlexBone grafts of either mineral composition, pre-drilled with 2 intersecting orthogonal channels for marrow penetrations (Fig. 2.4A), were readily press-fit into the 5-mm defects with excellent alignment to adjacent bones (Fig. 2.4B). Radiographic monitoring of the graft healing by X-ray (Fig. 2.4C) showed that the grafts remained stably positioned throughout the study, with calcified callus partially or completely bridging over the defect by 12 weeks.
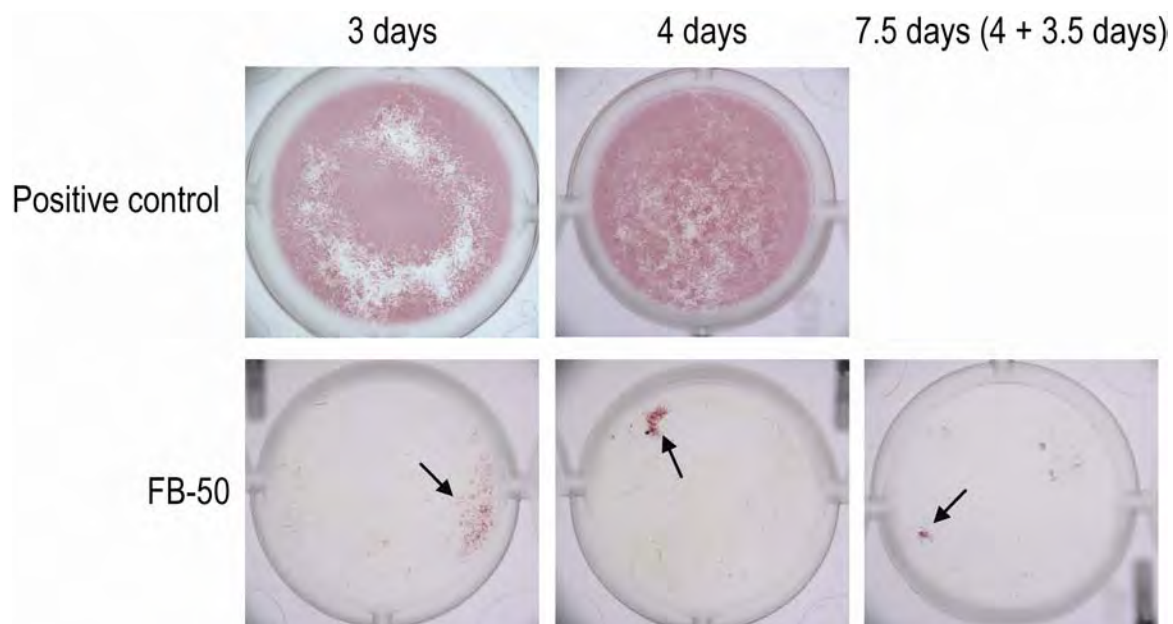
Figure. 2.2. FB-50 released pre-absorbed rhBMP-2/7 (40-ng/graft) in a sustained and localized manner over a 7.5 day period, and induced osteogenic transdifferentiation of C2C12 cells. Localized ALP staining (red), next to where the FB-50 graft was placed, was observed 3 and 4 days after the FB-50 pre-absorbed with 40-ng rhBMP-2/7 was placed in culture. When FB-50 retrieved from the day 4 time point was placed in a fresh well of C2C12 cells, localized ALP staining was observed after 3.5 days, indicating sustained release of rhBMP-2/7 from FB-50 over 7.5 days. Positive control wells were supplemented with 40-ng/well rhBMP-2/7 without a graft carrier.
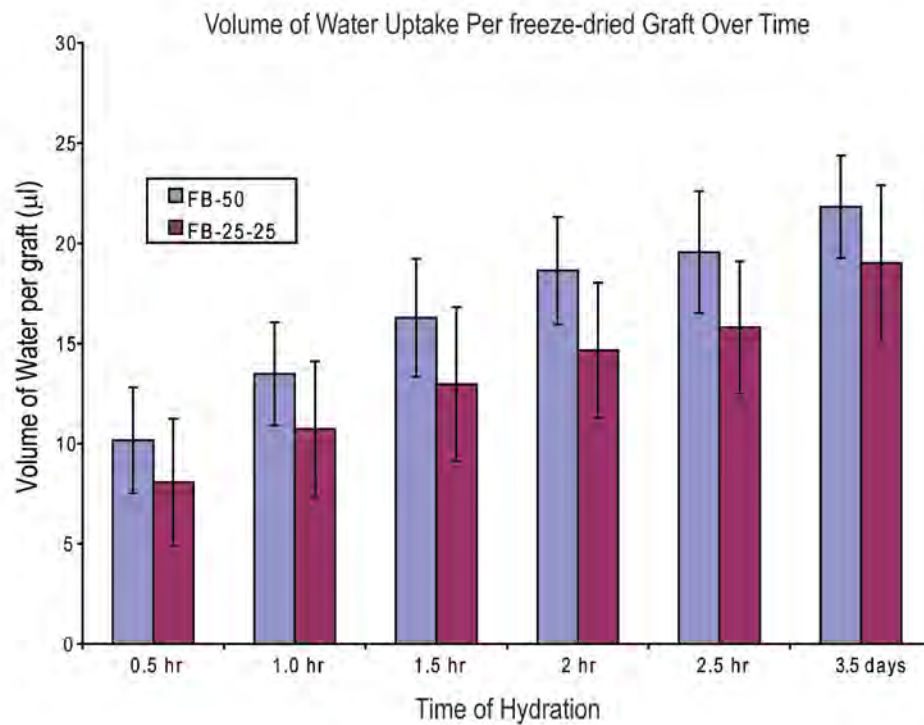
Figure 2.3. Volume of water uptake per freeze-dried graft over time. Error bars represent standard deviation of the mean (n=5).
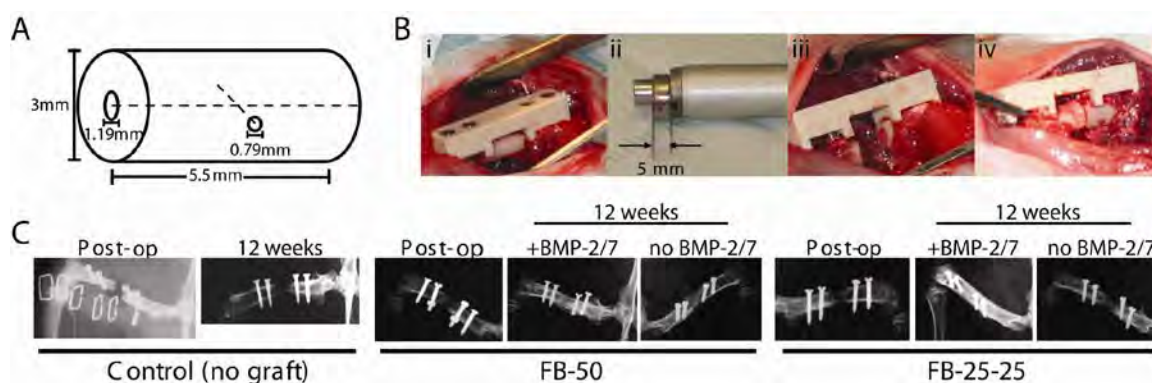
Figure 2.4. Graft design (A), surgical procedure (B) and radiographic follow-ups (C). The femoral segmental defect was surgically created by (i) securing a radiolucent PEEK plate fixator to the exposed femur (the periosteum was circumferentially removed from the femur to which the PEEK plate was attached with bicortical screws); (ii, iii) generating 5-mm mid-diaphyseal defect under the plate fixator with an oscillating Hall saw with parallel blades; and (iv) press-fitting a 5.5-mm long FlexBone (with or without 400-ng BMP-2/7) into the defect. Radiographic follow-ups confirmed the alignment and stability of the press-fit graft and the formation of a healing callus over 12 weeks. FB-50, FlexBone with 50wt% nanocrystalline hydroxyapatite; FB-25-25, FlexBone with 25wt% nanocrystalline hydroxyapatite plus 25wt% tricalcium phosphate; BMP-2/7, bone morphogenetic protein-2/7 heterodimer.

Histological analyses and polarized light microscopy (Fig. 2.5) revealed that the osteoconductivity of FlexBone facilitated healing in the absence of exogenous osteogenic growth factors. Bone marrow penetration throughout the orthogonal drill holes of the graft (FB-50), the emergence of an external callus, and the formation of an internal/medullary callus (within the graft drill hole and adjacent medullary cavity, Fig. 2.5A) was evident at 4 days post-op (Fig. 2.5B). By 2 weeks, the external callus bridging over the defect was partially mineralized, with ossification extending from the graft-cortical bone interfaces towards the center of the callus. Cartilage, stained purple by toluidine blue (Fig. 2.6), was prominently present at the mineralizing ends of the external callus, underscoring the endochondral ossification mechanism. Fig. 2.6 shows that the purple-staining cartilage was detected within the external callus of the FB-50 explants at 2-week (with and without rhBMP-2/7) and 6-week (without rhBMP-2/7) post-op, supporting endochondral ossification of the external callus. The purple-staining chondrocytes, however, were not detected within the internal callus at the time points examined (2-, 6- and 12-week post-op). Similar results were observed with the FB-25-25 explants. By 6 weeks, both the external and internal calluses were significantly remodeled and matured as evidenced by the recanalization[126] and the formation of oriented collagen fibrils revealed by polarized microscopy.[127] Although even greater orientation of collagen fibrils within the external callus was observed beyond 6 weeks, bridging of the defect by fully mineralized callus was not achieved by 12 weeks without rhBMP-2/7.

Figure 2.5. Cartoon depiction (A), histological analyses (B) of the callus formation surrounding a femoral segmental defect fit with FB-50 without recombinant human (rh) BMP-2/7, and immunohistological detection (C) of endogenous proteins absorbed on FB-50. Longitudinal sections of the explants obtained at various time points were stained for H&E, ALP (blue), and TRAP (red) to assess the cellularity and tissue types and to monitor osteoblastic and osteoclastic activities within the healing callus. Polarized light microscopy was used to assess collagen fibril orientation within the callus. Panel C selectively shows the absorption of endogenous TGFβ (Fig. 2.7 for a panel of additional proteins) on FB-50 within 1 week of implantation in rat femoral defects. Negative control stains of the 2-day FB-50 explant using TGFβ blocking peptide and rabbit IgG isotype control, respectively, are selectively shown. Endogenous TGFβ detected on pHEMA retrieved on day 2 is representatively shown (see Fig. 2.7 for other time points). Scale bars = 200 μm. H&E, hematoxylin and eosin; ALP, alkaline phosphatase; TRAP, tartrate-resistant acid phosphatase; TGFβ, transforming growth factor β; pHEMA, poly(2-hydoxyethyl methacrylate).

A

EC = external callus
(periosteum was surgically removed)
IC = internal callus
(formed within the graft drill hole)
MC = medullary (endosteal) callus

CB = cortical bone
FB = FlexBone
NB = new bone
BM = bone marrow
* = unmineralized callus

B

IC & MC within FB drill hole

EC bridging over FB

4 days · 2 weeks · 6 weeks · 2 weeks · 6 weeks · 12 weeks

H&E

Pol. light microscopy

ALP and TRAP

C

Endogenously secreted proteins absorbed on FB implant over 1 week

TGFβ

0.5 hours · 1 day · 2 days · 4 days · 1 week

Control stains on retrieved FB (2 days)

Blocking peptide · Rabbit IgG

Retrieved pHEMA implant
(2 days)

TGFβ

Figure 2.6. Cartoon depiction (A) and histological analyses (B) of the endochondral-mediated callus formation surrounding a femoral segmental defect fitted with FB-50 with or without rhBMP-2/7. Scale bars = 200 μm.

Remodeling activity (indicated by positive ALP and TRAP stains) was detected within internal, external, and medullary calluses throughout the 12-week study. A line of osteoclastic activity (red TRAP stain) was typically observed at the FlexBone-callus interface followed by a distinct line of osteoblastic activity (blue ALP stain), suggesting coordinated remodeling and osteointegration of FlexBone. Quantification of the numbers of TRAP positive cell nuclei and ALP positive cell nuclei at the graft-callus interface over time (Table 2.1) revealed persisting active graft remodeling activities by 6 weeks as evidenced by the increased osteoclastic activities compared to those detected at 2 weeks. Intense TRAP and ALP stains were still detected at the FlexBone-callus interface at 12 weeks, suggesting that the graft remodeling would continue over an extended period of time. Histological analysis of the FB-25-25 graft healing over time revealed similar observations.

	With no GF		With rhBMP-2/7	
	2 wk	**6 wk**	**2 wk**	**6 wk**
# TRAP-positive cell nuclei/0.1mm^2	101 +/- 134	118 +/- 38	158 +/- 55	43 +/- 83
# ALP-positive cell nuclei/0.1mm^2	202 +/- 144	67 +/- 79	113 +/- 59	38 +/- 26

Table 2.1. Quantification of TRAP positive nuclei (osteoclastic activity) and ALP positive nuclei (osteoblastic activity) detected at each millimeter of the FlexBone-callus interface as a function of time and growth factor treatments. n = 7-9; values are expressed as means +/- standard deviation.

In a subset of experiments (Fig. 2.7), we showed that FlexBone effectively absorbed a number of endogenously secreted factors (TGFβ, IL-1β, TNF-α, VEGF, RANKL, BMP-2, BMP-7 and SDF-1) associated with the initiation of the inflammation[73, 128] /graft healing cascade[129] and the recruitment of progenitor cells.[77, 130] Whereas the majority of these factors were initially (0.5 h after implantation) detected on the surface of the graft where progenitor cells were recruited to, the secreted molecules quickly penetrated throughout the 3-dimensional network and were effectively retained by the nHA component (Fig. 2C). By contrast, the un-mineralized pHEMA controls were not able to attract and retain these endogenously secreted molecules within its 3-dimensional network. Unimplanted FB-50 stained for the same panel of antibodies, as well as IgG isotype control (rabbit or mouse IgG) stains performed on all FB-50 explants retrieved at various time points, revealed minimal staining (Fig. 2.7C).

Figure 2.7. Immunohistological detection for endogenous proteins absorbed on FB-50 (A) or pHEMA control (B) retrieved at 0.5 hours, 1, 2, and 4 days, and 1 week after being press-fit into 5-mm femoral segmental defects in rats. For pHEMA control, only stains for TGFβ were representatively shown. IgG isotype control (rabbit and mice) stains of FB-50 retrieved at 2 days are shown in (C). Scale bars = 200 μm.

A

Negative control
(Unimplanted FB-50)

Endogenously secreted proteins absorbed on FB-50 implant over 1 week

| | 0.5 hours | 1 day | 2 days | 4 days | 1 week |

TGFβ

TNFα

IL-1β

VEGF

RANKL

BMP-2

BMP-7

SDF-1

B

Endogenously secreted proteins absorbed on pHEMA implant over 1 week

| 1 day | 2 days | 4 days | 1 week |

TGFβ

C

IgG isotype control stains on FB-50 (2 days)

Mouse IgG   Rabbit IgG
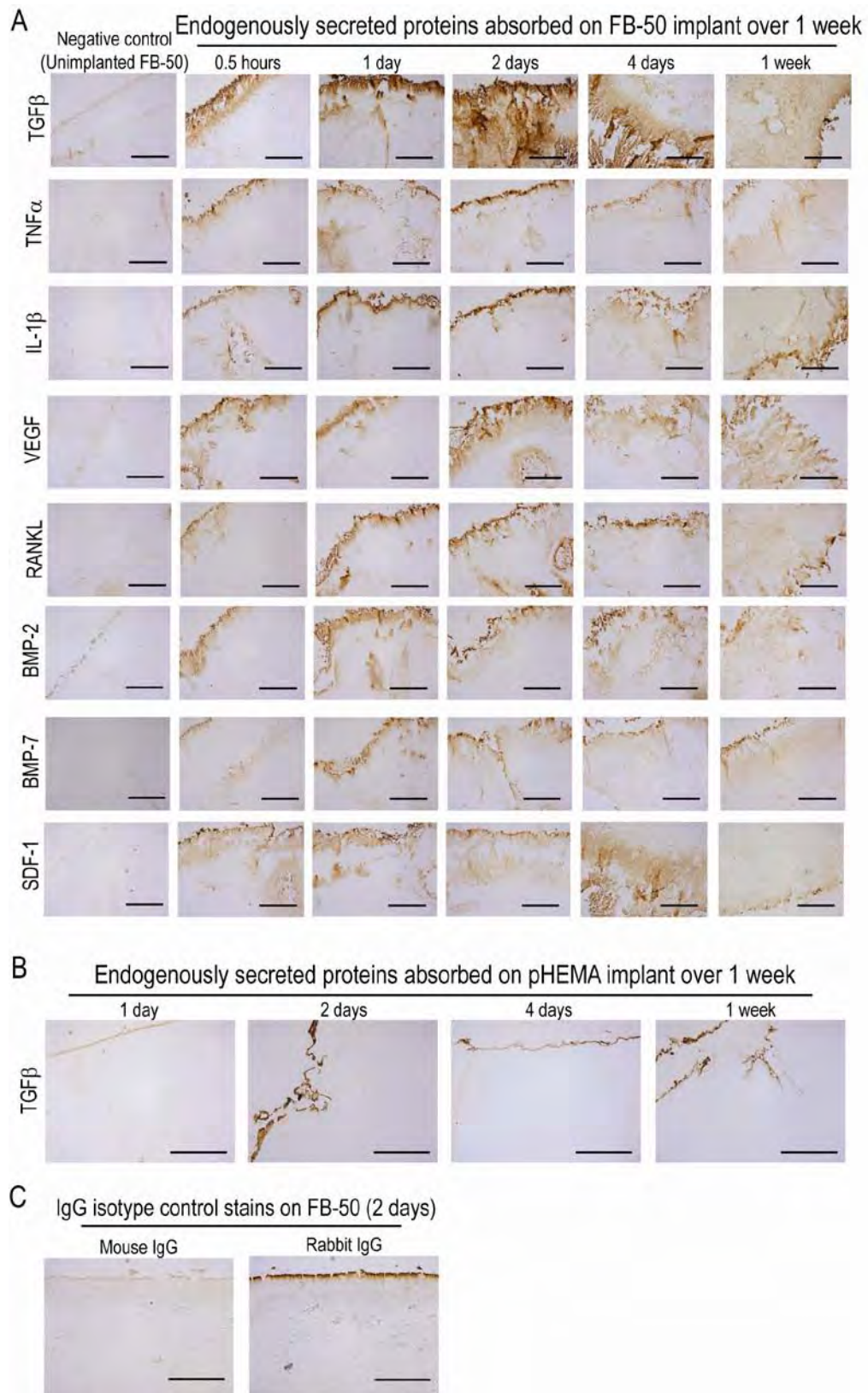
Expedited healing of femoral critical defects by FlexBone in the presence of rhBMP-2/7.

Acceleration of the graft healing by delivery of rhBMP-2/7 using FlexBone was examined with each mineral composition. The capacity of FlexBone to locally deliver exogenous rhBMP-2/7 enhanced the graft osteoinductivity and led to expedited repair of the critical-size femoral defects by 8 weeks (Fig. 2.8). When press-fit with FlexBone (FB-50) containing 400-ng rhBMP-2/7, the defect was completely bridged by maturing and recanalizing internal and external bony calluses at 6 weeks. By 8 weeks, the collagen fibrils in the healing calluses exhibited excellent alignment with little change observed beyond that point. FB-25-25 supplemented with 400-ng rhBMP-2/7 enabled the formation of bridging bony calluses in a similar fashion. The accelerated active graft remodeling in the presence of rhBMP-2/7 was evidenced by >50% higher counts of TRAP-positive cell nuclei at 2 weeks post-op, and a more rapid drop of the number by 6 weeks as compared to those observed for the group without BMP-2/7 treatment (Table 2.1).
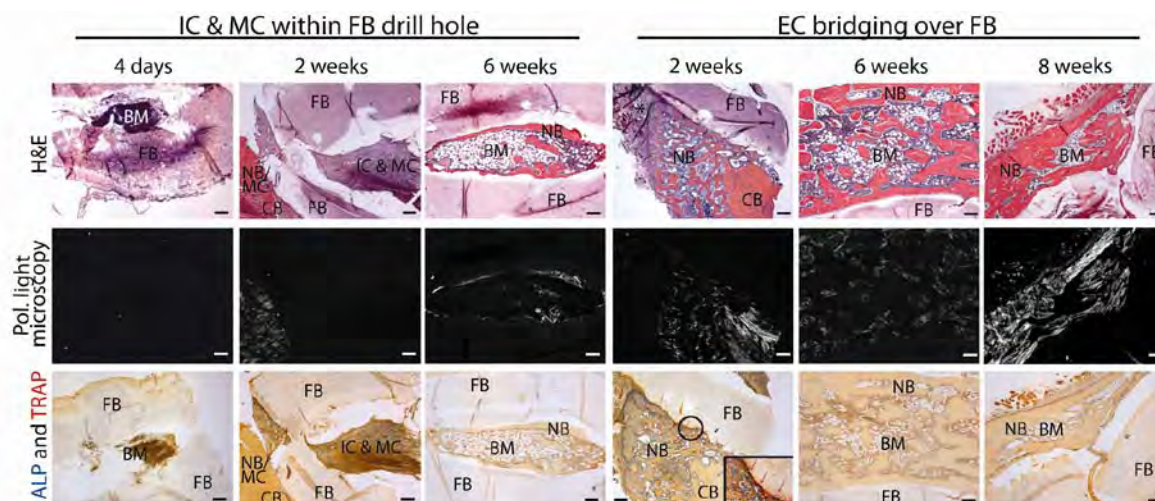
Figure 2.8. Histological analyses of the callus formation surrounding a femoral segmental defect fit with FB-50 with recombinant human (rh) BMP-2/7 (400 ng). Longitudinal sections of the explants obtained at various time points were stained for H&E, ALP (blue), and TRAP (red) to assess the cellularity and tissue types and to monitor osteoblastic and osteoclastic activities within the healing callus. Polarized light microscopy was used to assess collagen fibril orientation within the callus. Scale bars = 200 μm.

Quantitative assessment of the repair of femoral critical defects by FlexBone as a function of mineral composition and rhBMP-2/7 treatment.

Quantitative assessment of the healing callus formation by microCT (Fig. 2.9A) and torsion testing (Fig. 2.9B) indicated successful functional repair of the critical-sized femoral defects by 12 weeks using FlexBone augmented with 400-ng rhBMP-2/7. Three-dimensional reconstruction of the microCT scans revealed robust mineralized external callus completely bridging over the FlexBone-filled defects when supplemented with rhBMP-2/7. Two-dimensional color maps of the center cross-sections confirmed that the mid-point of these grafts was fully encapsulated with mature and recanalized external and internal mineralized calluses. By contrast, defects filled by FlexBone of either mineral composition without rhBMP-2/7 treatment were only partially bridged by mineralized calluses. With the treatment of a single dose of 400-ng BMP-2/7, bone volume fractions and bone mineral contents of the 12-week explants increased by >100%. From 8 weeks post-op to 12 weeks post-op, defects treated with FB-50 and rhBMP-2/7 showed little increase in bone mineral content (Fig. 2.10B) but a 20% increase in bone volume fraction (Fig. 2.10A), suggesting continued remodeling of the bony callus beyond 8 weeks.

Figure 2.9. Microcomputed tomography analyses (A) and torsion tests (B) of 12-week explants as a function of graft mineral composition and BMP-2/7 treatment. Effective voxel size of 18x18x18 μm^3 was applied to the reconstructed three-dimensional isosurface images and the two-dimensional color maps of the center slice of the explants (red representing a higher degree of mineralization). Graphed data are presented as boxplots, where red dots indicate median values and blue dots represent sample outliers. Note that FB explants without BMP-2/7 treatment did not fail during the torsion test (likely due to the lack of a fully bridging stiff bony callus and the elasticity of underlying FlexBone). Explants were loaded to failure at a rate of 0.5°/s. [#]The values reported represent the torque and energy at which the testing was stopped. *p<0.05 is considered significant.

53
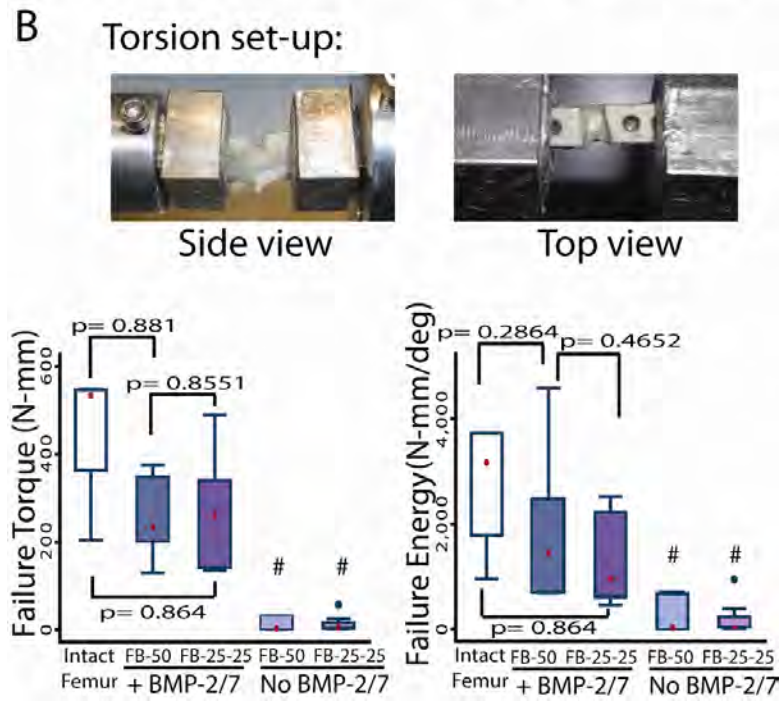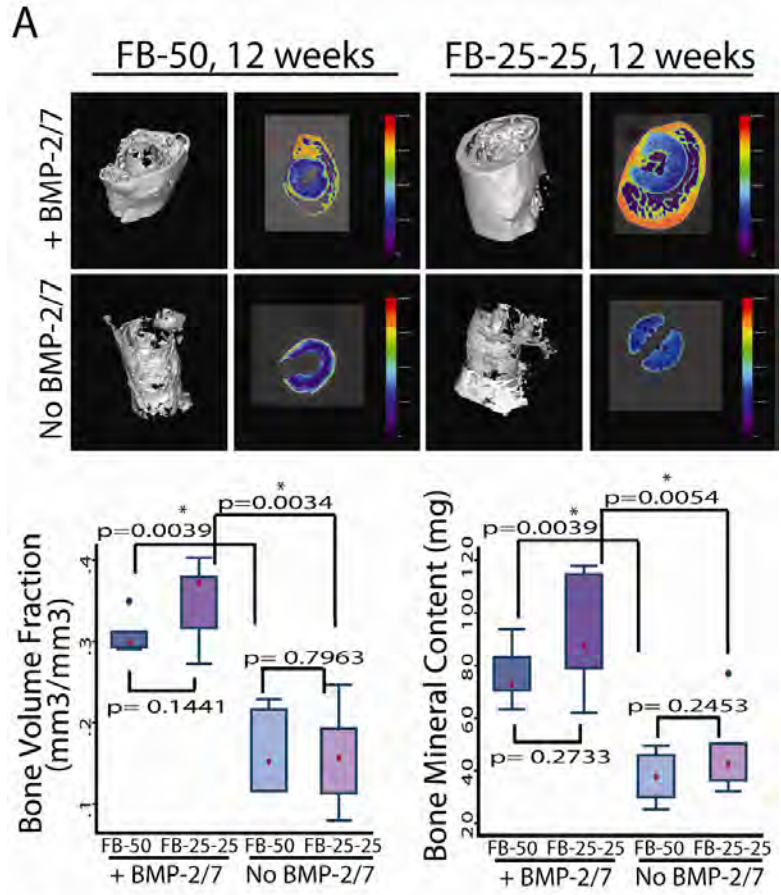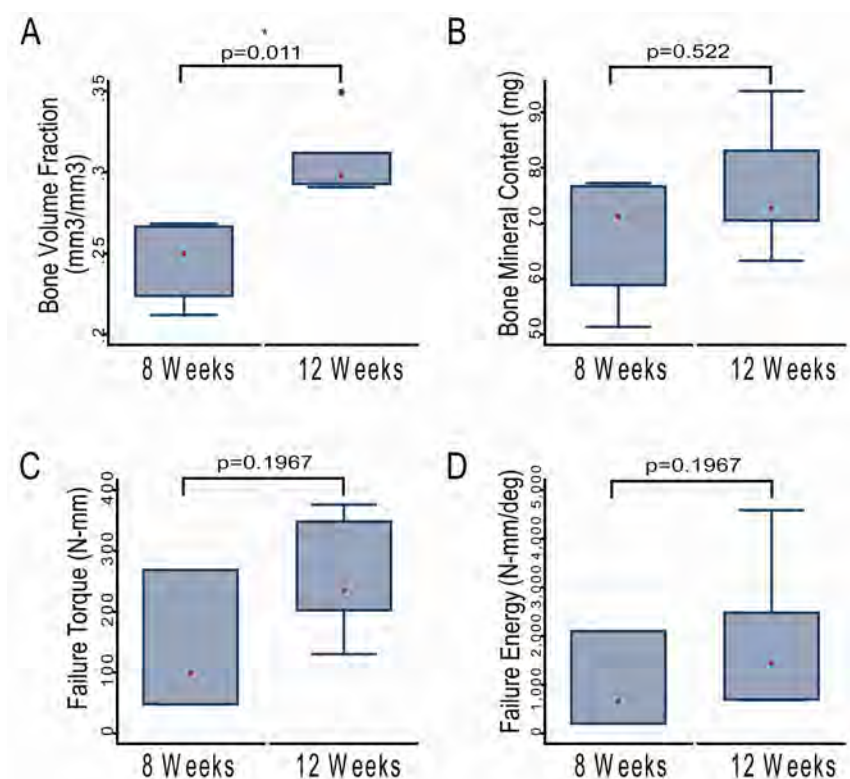
Figure 2.10. Micro-CT analyses and torsion tests of 8- and 12-week explants press-fit with FB-50 grafts supplemented with 400-ng BMP-2/7. **(A)** Bone volume fraction over time; **(B)** bone mineral content over time; **(C)** failure torque over time; **(D)** failure energy over time. Explants were loaded to failure at a rate of 0.5°/s. Graphed data are presented as boxplots, where red dots indicate median values and blue dots represent sample outliers. $P < 0.05$ is considered significant. 8- and 12- week explants were harvested for microCT analysis at $n = 4$ and $n = 6$, respectively, and torsion testing at $n = 3$ and $n = 6$, respectively.

The remarkable healing achieved by a combination of osteogenesis and osteoconduction in the growth factor-treated group translated into the restoration of torsional strength of the femoral defects. The maximum torque and energy to failure values of the explants in the rhBMP-2/7-treated group approximate those of intact femurs (Fig. 2.9B)[131] or the femoral defects repaired by gene therapy,[129, 132] and surpass those accomplished by allograft-mediated repair.[133] Despite an upward trend over time, the observed difference in failure torque or failure energy between the 8- and 12-week explants was statistically insignificant (Figs. 2.10C & 2.10D), suggesting that the bony callus formed at 8 weeks already possessed adequate strength.

Discussion

We have shown that FlexBone, a structural composite of nHA and hydrophilic pHEMA hydrogel matrix, possessed unique properties desired for the repair of critical-sized femoral defects. The compressibility of FlexBone allowed for its convenient and stable press-fitting into a critical-sized femoral defect, and its pre-drilled interconnected channels facilitated bone marrow penetration and enabled the stabilization of the defect via the formation of both internal and external calluses. Effective recruitment of bone marrow progenitor cells via the drill holes and the affinity of the nHA component for endogenously secreted signals required for initiating the inflammation/graft healing cascade are likely contributors to the partial repair enabled by FlexBone in the absence of any exogenous osteogenic factors.

Further, we demonstrate that the local delivery of low-dose rhBMP-2/7 via FlexBone (400-ng/graft) enabled expedited functional repair of the critical defect by 8-12 weeks via its acquired osteoinductivity. The biomechanical function of the defect was restored to the level comparable to those achieved by successful gene therapy, but without the common risks associated with the latter.[129, 132] This was likely achieved due to the robust host-to-host junction of the bridging bony callus and the increase in cross sectional area (callus volume) and the degree of mineralization of the new bone collar. The low rhBMP-2/7 working dose accomplished in this study is 1-2 orders of magnitude lower than those utilized in rhBMP-2 therapy in treating similar defects,[65, 88] likely resulting from a combination of higher potency of the heterodimer and the ability of FlexBone to release it in a more sustained and localized manner.[68] This feature could be translated into FlexBone-mediated delivery of protein therapeutics in a more cost-effective and safer fashion (e.g. with less proteins rapidly diffused away from the carrier), potentially benefiting the clinical treatment of hard-to-heal bony lesions.

No significant difference in the functional outcome (based on microCT and torsion data) of FlexBone-assisted repair of critical femoral defects was observed between the two mineral compositions examined (FB-50 vs. FB25-25). Thus, the choice for mineral composition will likely be dictated by the desired physical properties of the scaffold for any given application. For instance, FB25-25 has higher compressability than FB-50 under physiological conditions, achieving 25% strain (as opposed to 10% for FB-50[68]) under 0.5 MPa compressive load,[118] making it easier to be press-fit into a defect

with limited accessibility. The stiffer properties of the FB50, on the other hand, could enable the graft more tightly fit within an open defect.

The dimensional stability and biocompatibility of FlexBone, along with the persistent remodeling observed at the graft-callus interface, resemble some of the best features of structural allografts.[134] Patients receiving a successful structural allograft implantation would often live with the allograft for life, with the graft being slowly remodeled over time generating little inflammatory degradation product. Unlike the overwhelming numbers of biodegradable polymeric bone substitutes designed for tissue engineering applications,[135] the crosslinked pHEMA hydrogel network in FlexBone is not hydrolytically degradable by design. Vital organs collected from the rats receiving FlexBone implants for 12 weeks were pathologically indistinguishable from age-matched control organs harvested from un-operated rats (Fig. 2.11). We argue that biodegradability is not a functional requirement of viable synthetic bone grafts. To further explore the clinical potential of FlexBone, however, *in vivo* studies using large animal models and full toxicological analyses to determine the longer term remodeling pattern and safety (longer-term systemic effects) of FlexBone need to be carried out.
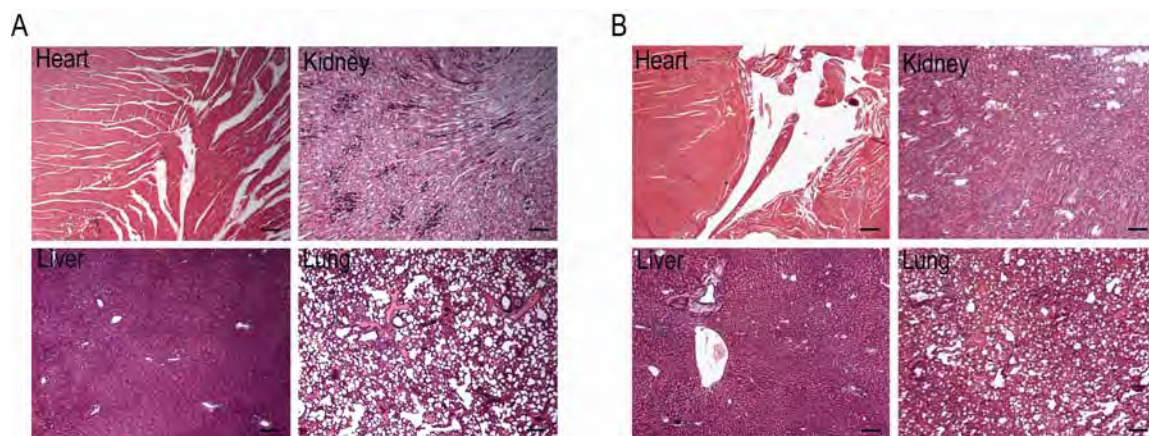
Figure 2.11. H&E staining of the vital organs collected from a rat 12 weeks after receiving femoral FB-50 implantation (A) vs. that of the control organs collected from an un-operated rat (B). Scale bars = 200 μm.

In summary, FlexBone combines some of the best features of structural allografts (osteoconductivity and dimensional stability)[4, 135, 136] with desirable surgical compressibility and scalability of synthetic biomaterials. The ability of FlexBone to locally deliver biological therapeutics in a significantly reduced effective dose to enable expedited functional repair of the critical defect opens the door to engineer the biochemical properties of the graft[77] based on individual needs. More broadly, our work supports the notion that functional sophistication of synthetic tissue grafts is not synonymous with complicated chemical/engineering designs.[9] We show that by recapitulating the multifaceted roles that key extracellular matrix components play in defining tissue-specific microenvironment, easy-to-prepare biomaterials can be designed to facilitate functional tissue repair.

Acknowledgements

Author Disclosure Statement

No competing financial interests exist.

Chapter III: Chemically modified cellulose fibrous meshes for use as tissue engineering scaffolds

This chapter has been adapted from the following published manuscript:

Filion TM, Kutikov A, Song J. Chemically modified cellulose fibrous meshes for use as tissue engineering scaffolds. *Bioorg Med Chem Lett.*, volume: 21, issue: 17, pages 5067-70, 2011.

Abstract

Cellulose and sulfated cellulose fibrous meshes exhibiting robust structural and mechanical integrity in water were fabricated using a combination of electrospinning, thermal-mechanical annealing and chemical modifications. The sulfated fibrous mesh exhibited higher retention capacity for human recombinant bone morphogenetic protein-2 than the cellulose mesh, and the retained proteins remained biologically active for at least 7 days. The sulfated fibrous mesh also more readily supported the attachment and osteogenic differentiation of rat bone marrow stromal cells in the absence of osteogenic growth factors. These properties combined make the sulfated cellulose fibrous mesh a promising bone tissue engineering scaffold.

Electrospinning is a robust technique for fabricating polymer fibrous meshes mimicking the extracellular matrices (ECM) of natural tissues.[117] By adjusting the viscosity and surface tension of the polymer solution as well as the voltage, speed and duration of the electrospinning process, polymer fibrous meshes of varied fiber dimensions and mesh thicknesses and porosities could be obtained.[137, 138] For *in vivo* tissue engineering applications, however, these fibrous meshes should also be engineered with proper biochemical microenvironment (e.g. via the retention of tissue-specific biological cues) to help support cellular attachment, direct stem cell differentiation, and guide tissue integration.

Covalent modification of synthetic scaffolds with growth factors was previously attempted for expediting bone tissue repair.[139, 140] This approach, however, risks compromising the bioactivity of the proteins due to substantial structural perturbation.[141, 142] By contrast, strategies for retaining protein therapeutics through non-covalent electrostatic interactions are more biomimetic in nature. For instance, sulfated polysaccharides are known for their high affinity for many endogenous proteins within the ECM environment such as various isoforms of bone morphogenetic proteins (BMPs),[143-146] presumably through favorable electrostatic interactions between the sulfate residues and the basic amino acid residues of the proteins. Such biopolymers are ideal candidates for the fabrication of synthetic tissue scaffolds. Indeed, chondroitin sulfate, an important sulfated structural component of cartilage tissue, has been shown to enhance bone remodeling of musculoskeletal defects when used in combination with other bone grafting materials.[147] The application of electrospun chondroitin sulfate fibrous meshes to

augment the performance of 3-dimensional tissue engineered constructs, however, has proven challenging due to their exceptionally high solubility in water. In our hands, methacrylating chondroitin sulfate with glycidyl methacrylate [138] prior to electrospinning, followed by covalent crosslinking of the electrospun meshes, failed to improve the stability of the mesh in water.

Here we report a practical method for preparing water-stable sulfated polysaccharide fibrous meshes from readily accessible electrospun cellulose acetate. The electrospun meshes are thermal-mechanically annealed to sustain sequential chemical modifications (Fig. 3.1A) and to exhibit adequate tensile modulus for use as a flexible 2-dimensional tissue engineering scaffold (e.g. to be wrapped around 3-dimensional tissue grafts or embedded within a tissue defect). The ability of the sulfated fibrous meshes to retain human recombinant bone morphogenetic protein-2 (rhBMP-2) and to support the *in vitro* attachment and osteogenic differentiation of bone marrow stromal cells (MSCs) for potential bone tissue engineering applications are examined and compared with those of the uncharged cellulose meshes.

Cellulose is chosen as the candidate for sequential chemical modifications because it is an affordable natural polysaccharide known for its abundance, aqueous stability, cytocompatibility, and chemical functionalizability.[148, 149] Cellulose itself, however, is not soluble in most organic solvents, thus unsuitable for electrospinning. Thus, we first electrospun cellulose acetate (CA) fibrous mesh by ejecting tetrafluoroethylene solution of CA (150 g/L) at a rate of 2.4 mL/h under 15 kV with a distance of 10 cm between the ejection tip and the collection plate. After 4 h of electrospinning, CA fibrous meshes 400-

650 μm in thickness and with fiber diameters ranging from several hundred nanometers to a few micrometers were obtained (Fig. 3.1B).
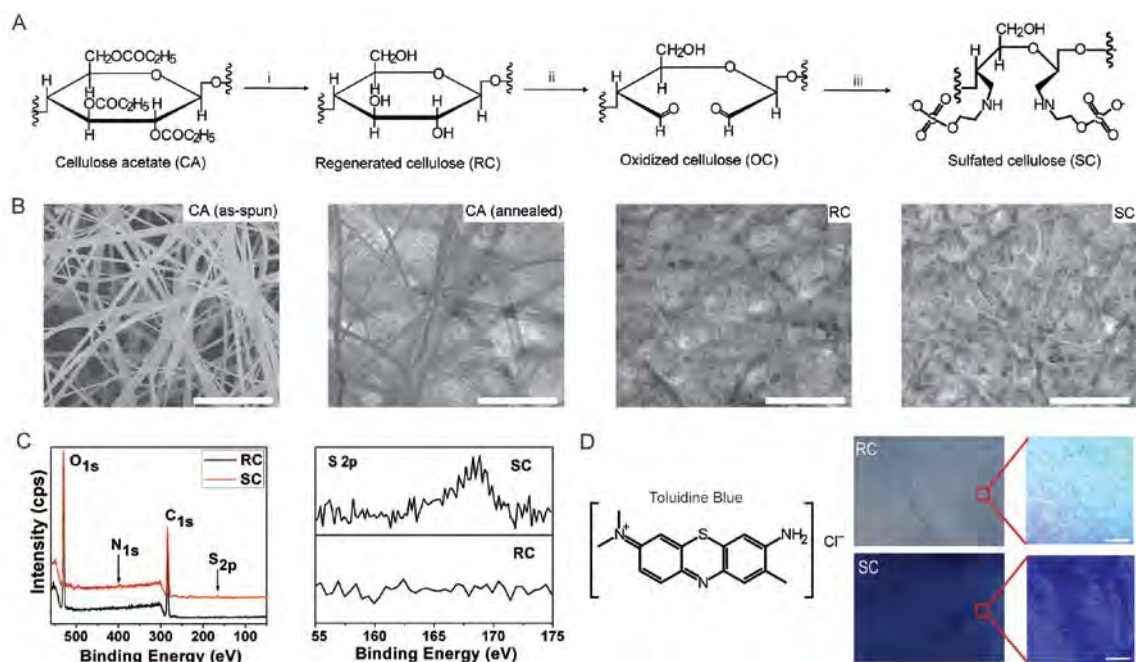
Figure 3.1. Chemical modification and characterization of modified cellulose acetate mesh. **A)** Synthetic scheme for chemical modification of thermal-mechanically annealed CA mesh. i) NaOH (0.1 N, 1:4/ EtOH:H_2O), rt, 12 h; ii) $NaIO_4$ (5 mg/mL, PBS), rt, 10 h; iii) 2-aminoethyl sulfate (0.05 g/mL, PBS), $NaBH_3CN$ (2.5 mg/mL, PBS), pH 7.4, rt, 12 h. All meshes were gently shaken on an orbital shaker during the chemical treatment and extensively washed in MilliQ water afterwards. **B)** SEM micrographs of as-spun, thermal-mechanically annealed, and chemically modified meshes. Scale bars = 40 µm. **C)** X-ray photoelectron spectroscopy scans of the RC and SC meshes. **D)** Optical micrographs of RC and SC meshes after being immersed in an aqueous solution of toluidine blue (4 wt%) for 1 min and thoroughly rinsed in MilliQ water. Scale bars = 500 µm.

The as-spun CA meshes were cut into 2" by 2" square pieces and annealed on a Carver hydraulic hot press under 25.85-MPa compressive loading for 10 min at either room temperature or 90 °C, which was >20 °C above the glass transition temperature of CA [150] and chosen to enhance the physical bonding of the CA fibers. The final thicknesses of the mechanically and thermal-mechanically annealed CA meshes were approximately 100☐ µm and 60 µm, respectively. SEM micrographs (Fig. 3.1B) confirmed that whereas the fiber dimensions remained unchanged upon thermal-mechanical annealing, the annealed mesh exhibited denser packing between fibrous layers. The annealed CA mesh was then deacetylated in aqueous base (Fig. 3.1A) to yield regenerated cellulose (RC), which was further oxidized by sodium periodate to obtain the aldehyde reactive handles for coupling with 2-aminoethyl sulfate under reductive amination conditions to generate the sulfated cellulose (SC) mesh. The complete deacetylation of the CA mesh and the subsequent oxidation and reductive amination were monitored and verified by Fourier transform infrared spectroscopy (Fig. 3.2). X-ray photoelectron spectroscopy analysis performed on the SC mesh detected the S and N signals that were absent from the RC mesh (Fig. 3.1C). The sulfated mesh was also readily stained by positively charged toluidine blue dye, which is commonly used for the histochemical detection of sulfated glycosaminoglycans in cartilage. By contrast, only a minimal amount of toluidine blue was absorbed on the uncharged RC mesh. Overall, these findings support successful sequential chemical modifications. The average thickness of RC mesh obtained from the mechanical compressed CA mesh was 103±6 µm, and the average thicknesses of the RC and SC meshes obtained from the thermal-mechanically annealed CA mesh were 65±5 µm and

58±5 μm, respectively, supporting minimal thinning resulting from the chemical modifications. SEM micrographs (Fig. 3.1B) revealed some degree of narrowing of the fiber diameters upon chemical treatment, although the overall packing density between fibrous layers of the RC and SC meshes were comparable to that of the thermal-mechanically annealed CA mesh.
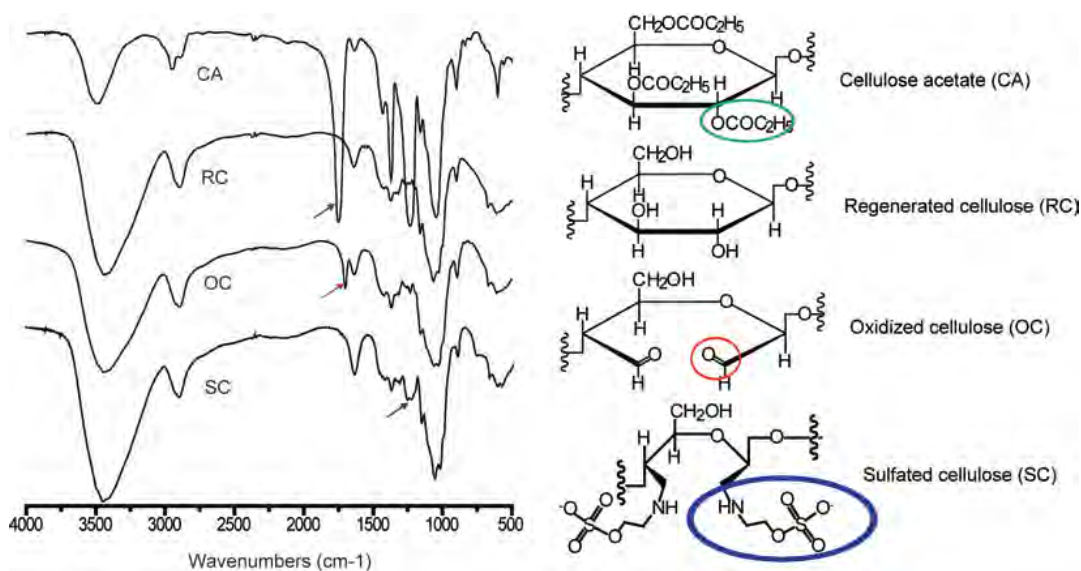
Figure 3.2. Fourier transform infrared spectroscopy (FTIR) supporting sequential chemical modifications. FTIR characterization of the regenerated cellulose (RC) mesh supported the complete removal of the acetyl groups (green arrow) from the cellulose acetate (CA) mesh upon base hydrolysis. The oxidized cellulose (OC) mesh exhibited a characteristic FTIR absorption at 1700 cm-1 corresponding to the aldehyde functionality (red arrow). After reductive amination with 2-aminoethyl sulfate, the sulfated cellulose (SC) mesh exhibited signals corresponding to aminoethyl sulfate (blue arrow).

Tensile mechanical testing of the meshes in hydrated state (Fig. 3.3) show that thermal-mechanical annealing is superior to mechanical compression alone for mesh processing. The RC mesh obtained from thermal-mechanically annealed CA exhibited significantly higher elastic modulus and ultimate tensile strength (~500% increases, $p < 0.05$) than those obtained from the mechanically compressed mesh. Without prior thermal-mechanical annealing, the SC mesh obtained after multi-step chemical modifications was not robust enough to withstand tensile mechanical testing. By contrast, the SC mesh functionalized from thermal-mechanically annealed CA mesh maintained megapascal-elastic modulus and ultimate tensile modulus in water. The thermal-mechanically annealed RC and SC meshes also exhibited >5% ultimate tensile strains. Overall, these meshes exhibit promising mechanical integrity for flexible manipulations as tissue engineering scaffolds (e.g. wrapping around a 3-dimensional scaffold, press-fitting in an area of defect, or covering an open wound surface with minor stretching).
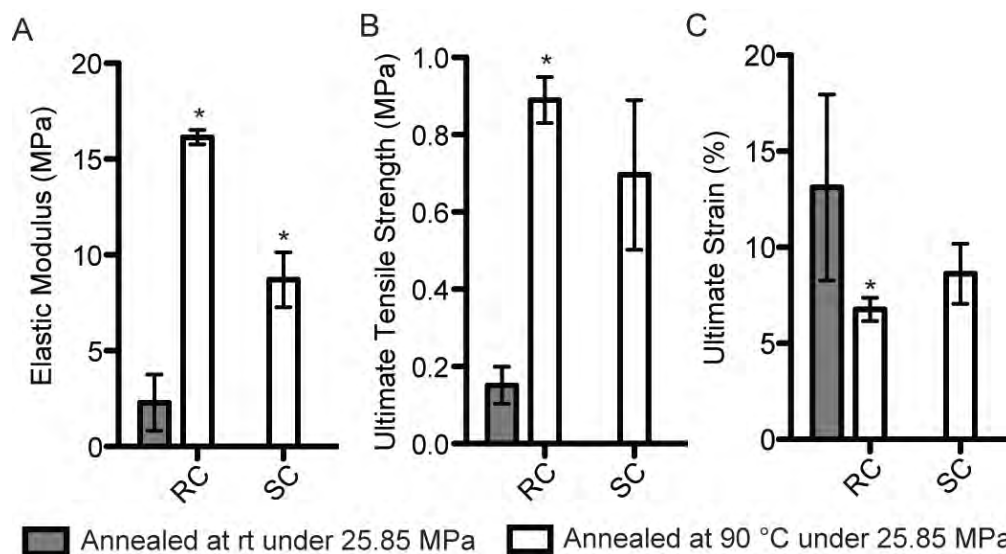
Figure 3.3. (A) Tensile elastic modulus, **(B)** ultimate tensile strength, and **(C)** ultimate tensile strain of hydrated RC and SC meshes as a function of annealing conditions. All testing was performed at rt on a Q800 dynamic mechanical analyzer (TA Instruments) equipped with a tensile submersion fixture filled with MilliQ water. Specimens (6-mm wide, 15-mm long, N=3) were preloaded with a tensile force of 0.01 N and ramped to failure at a rate of 0.1 N/min. Elastic modulus was calculated as the slope of the linear region of the stress-strain curve. Ultimate tensile strength and ultimate tensile strain were determined as the maximum stress and maximum strain at break, respectively. Error bars indicate standard deviation; * indicates $P < 0.05$ as determined by Student's t-test.

To examine the ability of RC and SC fibrous meshes to retain/release protein therapeutics, the meshes were absorbed with a single dose of rhBMP-2 (R&D Systems, pI = 9.3, 27-ng/cm^2) and incubated in PBS at 37 ºC for 7 days. The rhBMP-2 released from the meshes over time was quantified by an enzyme-linked immunosorbent assay (ELISA, R&D Systems). As shown in Figure 3.4A, both meshes released pre-absorbed rhBMP-2 in a sustained manner over 7 days. The SC mesh exhibited better retention of rhBMP-2 than the RC mesh, with >85% of the protein still retained on the sulfated mesh after 7 days. More importantly, the rhBMP-2 retained on both RC and SC meshes remained biologically active, as evidenced by their ability to induce the osteogenic trans-differentiation of myoblast C2C12 cells in culture. In the absence of rhBMP-2, C2C12 cells cultured on RC and SC meshes did not express osteogenic marker alkaline phosphatase (Fig. 3.4B, bottom). However, when they were seeded on the BMP-treated meshes retrieved after 7-day incubation in PBS, the expression of alkaline phosphatase (stained red) was detected on day 3 of the culture (Fig. 3.4B, top), supporting the osteoinductity[141] of the recombinant protein retained on the meshes.
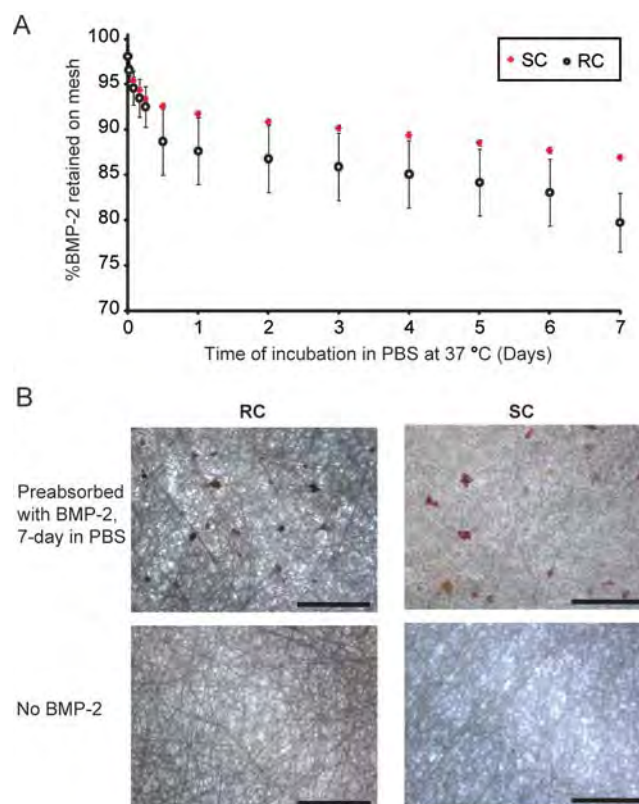
Figure 3.4. A) Retention/release profile of rhBMP-2 on/from SC vs. RC meshes. The mesh (N=3) was pre-absorbed with rhBMP-2 (27 ng/cm^2) and air-dried before being incubated in PBS at 37 °C for 7 days. The protein released in PBS at a given time was quantified by ELISA. **B)** Bioactivity of the rhBMP-2 retained on the mesh after 7-day incubation in PBS as indicated by their ability to induce osteogenic trans-differentiation of myoblast C2C12 cells. C2C12 cells were seeded (10,000 cells/cm^2) on either BMP-2 treated meshes retrieved after 7-day incubation in PBS (top) or those without rhBMP-2 treatment (bottom), and cultured in DMEM with 10% FBS without additional supplement of BMP-2. Alkaline phosphatase staining (red) was performed on day 3 of the culture. Scale bars = 200 μm.

Finally, to assess the suitability of these fibrous meshes for bone tissue engineering applications, the ability of RC and SC meshes to support the attachment and osteogenic differentiation of rat bone marrow stromal cells (MSCs) were examined in culture. MSCs have the ability to differentiate into multiple lineages of the mesenchyme including osteoblasts,[151-153] and have been widely used for scaffold-assisted repair of bony defects. Total bone marrow was isolated from the long bone of an 8-week old male Charles River SASCO SD rat and the MSCs were established through adherent culture and expanded as previously described.[118] Passage 1 MSCs were seeded on RC and SC meshes (25,000 cells/cm^2) with and without pre-absorbed rhBMP-2 (27-ng/cm^2) and allowed to attach in expansion media (αMEM without ascorbic acid, 20% FBS). MTT cell viability assay (Fig. 3.5A) performed 48 h after the initial cell seeding showed that significantly more viable cells (>100% increase) were attached to the SC mesh than to the uncharged RC mesh, and that the absorption of rhBMP-2 on the meshes prior to cell seeding had little effect on the cellular attachment / early proliferation. To examine whether or not the intrinsic osteogenic differentiation potential of MSCs was retained upon being attached to the fibrous meshes for 2 days, the MSC-seeded RC and SC meshes (without prior rhBMP-2 absorption) were continually cultured in osteogenic differentiation media (αMEM with L-glutamine, 15% FBS, 10 nM dexamethasone, 20 mM β-glycerol phosphate, 50 μM 1-ascorbic acid 2-phosphate) for 3 weeks, with the osteogenic media changed every 2 to 3 days. Alizarin red staining was performed on day 21 for the detection of mineralized matrix deposition resulting from osteogenic differentiation of MSCs. As shown in Figure 3.5B, both RC and SC meshes were able to support the

osteogenic differentiation of MSCs, with the MSCs cultured on the SC mesh stained more intensely for alizarin red than the RC mesh. Minimal alizarin red staining was detected from the MSCs cultured on RC or SC meshes in expansion media. And as expected, the meshes without seeded cells exhibited negligible non-specific absorption of the negatively charged alizarin red dye. The ability of the SC fibrous mesh to more readily support the attachment and osteogenic differentiation of MSCs than the uncharged RC mesh suggests a potential role of the charged sulfate residue in affecting the cellular fate of MSCs *in vitro* and *in vivo*. How such a chemical modification affects the multi-potency of MSCs, particularly osteogenesis, chondrogenesis and adipogenesis, in a temporally defined manner is the subject of on-going investigations.
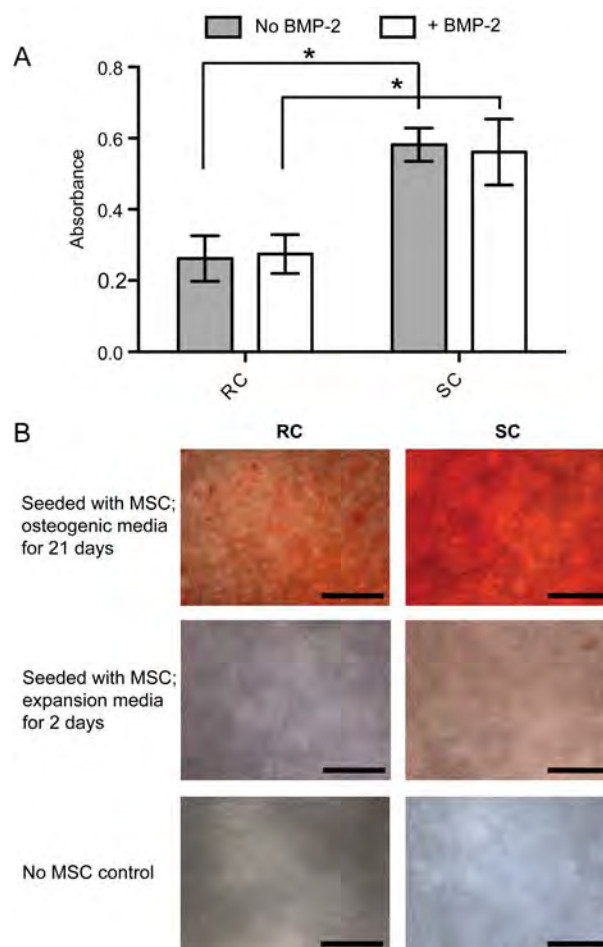
Figure 3.5. A) MTT cell viability assay performed 48 h after seeding rat MSCs on the RC and SC meshes with and without pre-absorbed rhBMP-2 in expansion media. **B)** Alizarin red staining of the MSCs cultured on RC and SC meshes in osteogenic differentiation media for 21 days (top) or in expansion media for 2 days (middle). Control meshes without cells were also stained (bottom). Scale bars = 200 μm. All meshes were equilibrated in PBS for 1 h prior to cell seeding. Seeding density for all experiments was 25,000 cells/cm^2. * $p \leq 0.01$ (student t-test)

In summary, using a combination of electrospinning, thermal-mechanical annealing, and sequential chemical modifications, water-stable sulfated cellulose fibrous mesh exhibiting good tensile mechanical strength was fabricated. The sulfated fibrous mesh exhibited better retention capacities for osteogenic growth factor rhBMP-2, and more readily supported the attachment and osteogenic differentiation of MSCs than the uncharged cellulose fibrous mesh. These fibrous meshes have great potential for bone tissue engineering applications.

Acknowledgments

Chapter IV: In vivo tissue responses to thermal-responsive shape memory polymer nanocomposites.

This chapter has been adapted from the following published manuscript:

Filion TM, XU J, Prasad ML and Song J. In vivo tissue responses to thermal-responsive shape memory polymer nanocomposites. *Biomaterials*, volume: 32, issue: 4, pages 985-991, 2011.

Abstract

To explore the safe use of thermal responsive shape memory polymers (SMPs) as minimally invasive "smart" tissue scaffolds, we recently developed a class of biodegradable POSS-SMP nanocomposites exhibiting stable temporary shape fixing and facile shape recovery within a narrow window of physiological temperature. The materials were covalently crosslinked from star-branched building blocks consisting a bioinert polyhedral oligomeric silsesquioxane (POSS) core and 8 degradable poly(D,L-lactide) (PLA) arms. Here we examine the degradation profiles and immunogenicity of POSS-SMPs as a function of the PLA chain lengths using a rat subcutaneous implantation model. We showed that POSS-SMPs elicited a mild foreign body type immune response upon implantation. The degradation rates of POSS-SMPs, both *in vitro* and *in vivo*, inversely correlated with the length of the PLA chains within the crosslinked amorphous network. Upon degradation, a second acute inflammatory response was elicited locally, and the inflammation was resolved over time without medical interventions. One year after the implantation of POSS-SMPs, no pathologic abnormities were detected from the vital / scavenger organs examined. These minimally immunogenic and biodegradable SMPs are promising candidates for scaffold-assisted tissue repair where both facile surgical delivery and controlled degradation are desired for improved clinical outcome.

1. Introduction

Thermal-responsive shape memory polymer (SMP) can be imparted with a permanent shape above a critical transition temperature (T_{trans}) when it is cast. Such a permanent shape, formed at the material's elastic state without external stress, can be retained or "memorized" as the material cools to a temperature below its T_{trans}. The material can be subsequently deformed into any desired temporary shape by force at $T>T_{trans}$, and be fixed as it cools down to $T<T_{trans}$. When a thermal stimulus ($T>T_{trans}$) is re-applied, the SMP can revert to its less strained permanent shape. These unique properties are attractive for tissue engineering applications as the SMP may be delivered in a minimally invasive temporary shape to an area of tissue defect, and subsequently revert to a permanent shape that precisely conforms to the defect upon thermal triggering.[154, 155] For safe clinical applications, a combination of stable temporary shape fixation at body temperature, a rapid and complete shape recovery at a T_{trans} slightly above physiological temperature, and suitable mechanical and biological properties of the SMP will be ideal.

Towards this end, we recently developed an amorphous SMP network cross-linked from a star-branched macromer (Fig. 4.1A) containing polyhedral oligomeric silsesquioxane (POSS) nanoparticle core and eight poly(*DL*-lactide) (PLA) arms.[156] The rigid POSS nanoparticle core facilitated maximal participation of the urethane-tethered PLA arms in the elastic deformation and recoiling process with reduced excessive chain-chain entanglement below and above T_{trans}, respectively. Consequently, the resulting

POSS-SMP nanocomposites, with cortical bone-like modulus (~ 2 GPa) at body temperature, could stably hold their temporary shape for > 1 year at room and body temperatures and achieve full shape recovery with a T_{trans}<50 °C in a matter of seconds. To fully explore the potential of POSS-SMPs as self-fitting tissue scaffolds and implants, biocompatibility of this new class of thermal responsive materials needs to be investigated.[157, 158]

Given the bioinert nature of the POSS core,[159] the established clinical use of PLA as bioresorbable sutures,[160, 161] and the prevalence of polyurethanes in medical implants,[155] we hypothesize that POSS-SMPs and their degradation products would elicit minimal immunogenic response *in vivo*. Here we examine both the *in vitro* and *in vivo* degradation behaviors of POSS-SMPs as a function of the PLA chain lengths of the macromer building blocks (Fig. 4.1A, n =10, 20, or 40) using a subcutaneous implantation model in rats. Tissue responses to POSS-SMPs and their degradation products over a course of 1 year were examined.

Figure 4.1. Chemical composition and in vitro hydrolytic degradation of POSS-SMPs. (A) Star-branched macromer building blocks of POSS-SMP; (B) %Mass residue of POSS-SMPs as a function of PLA arm length upon incubation in PBS (pH 7.4) at 37 °C. A qualitative illustration of the tissue repair kinetics is shown in purple. A sample size of 3 was applied; (C) SEM micrographs of POSS-SMPs before and after 73-day incubation in PBS at 37 °C.

A POSS-(PLA$_n$)8 → Diisocyanate crosslinker → POSS-SMP

$n = 10, 20, 40$

B

"Lag" phase

"Log" phase

"Plateau" phase

POSS-SMP-10
POSS-SMP-20
POSS-SMP-40

Mass residue (%) vs Time (day); Extent of tissue repair (%)

C Day 0 | POSS-SMP-10 Day 73 | POSS-SMP-20 Day 73 | POSS-SMP-40 Day 73

50 μm
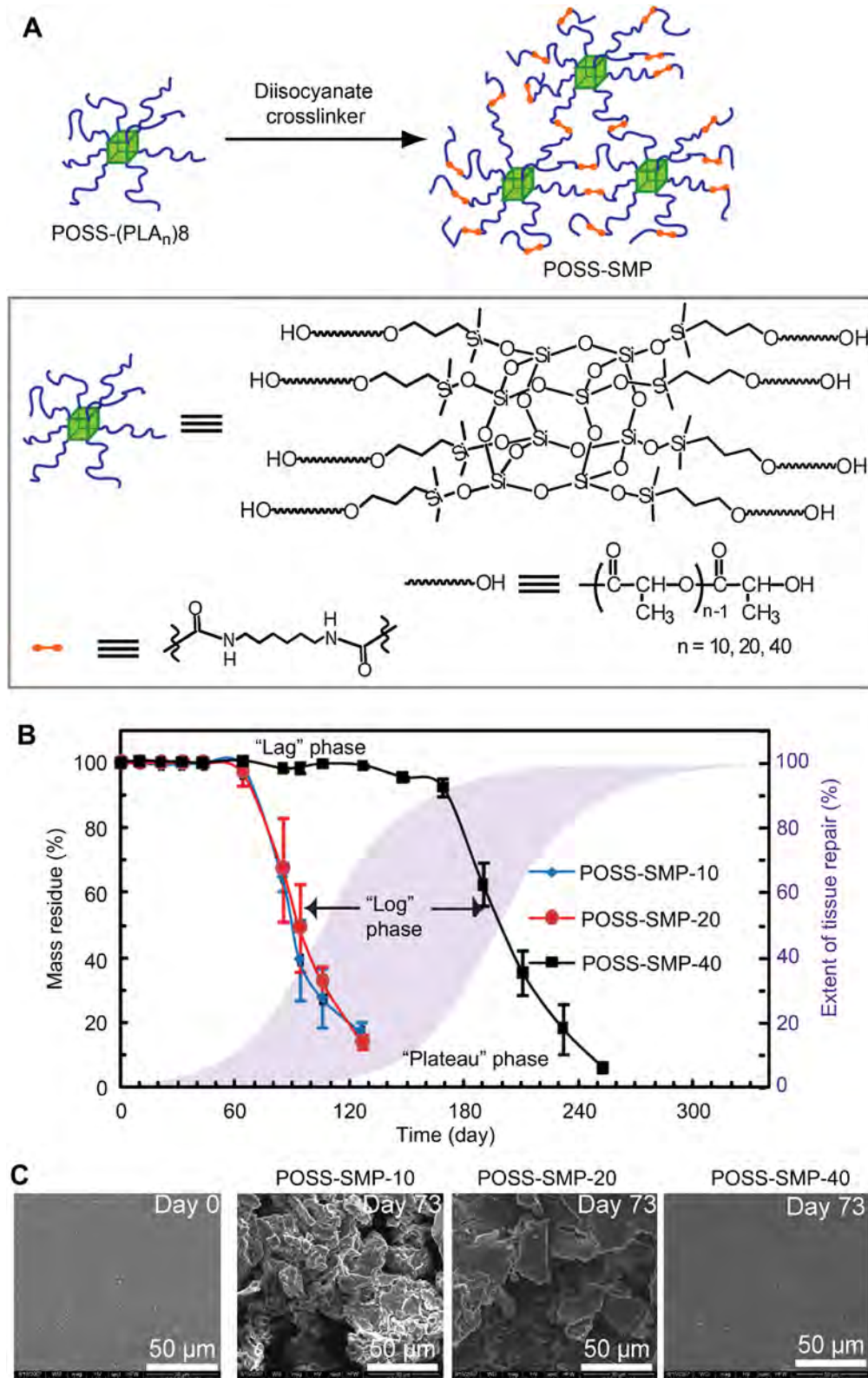
2. Materials and Methods

2.1. Sample preparation

POSS-SMP constructs were fabricated as previously described,[156] Briefly, macromer building block POSS-$(PLA_n)_8$ (n = 10, 20, 40) and crosslinker hexamethylene diisocyanate were mixed in 1:4 molar ratio in 2.5 times (wt/wt) dichloromethane. Catalytic amount (100 ppm) dibutyltin dilaurate (≥95%, Aldrich) was added. The solution was stirred for 2 h at rt before being poured into rectangular Teflon molds (30.0 mm × 6.0 mm). The solvent was evaporated at rt overnight under Argon, and the material was further crosslinked at 75 °C under Argon for 24 h. The final product was heated at 75 °C under vacuum for 48 h to remove residue volatiles. The POSS-SMP constructs were designated as POSS-SMP-10, POSS-SMP-20, and POSS-SMP-40 based on the PLA arm lengths of their respective macromer building blocks POSS-$(PLA_n)_8$ (n = 10, 20, 40). The glass transition temperatures (T_g) of POSS-SMPs, determined by differential calorimetry, were 42.8 °C (POSS-SMP-10), 45.4 °C (POSS-SMP-20), and 48.4 °C (POSS-SMP-40), respectively.[156] Detailed thermal dynamic mechanical characterizations and the quantification of the shape memory performances of POSS-SMPs as a function of their PLA arm lengths using a dynamic mechanical analyzer were reported elsewhere.[156] The POSS-SMPs (~0.5 mm in thickness) were cut into smaller pieces approximately 30 mg in weight for both the *in vitro* degradation study and the rat subcutaneous implantation study. Commercial *DL*-PLA pellets (MW 75-120kD, Aldrich) of the same weight were

used as a control. All POSS-SMPs and PLA control specimens were sterilized with 70%

ethanol and 254-nm UV irradiation prior to implantation.

2.2. In vitro hydrolytic degradation and scanning electron microscopy (SEM)

POSS-SMPs -10, -20 and -40 specimens (N=3) were incubated in PBS (pH 7.4,

100 mL/g) at 37 °C and retrieved at pre-determined time points. They were washed with

deionized water and freeze-dried to determine the residue masses. The samples were then

returned to a fresh PBS (100 mL/g) and incubated at 37 °C. The percentage (%) of mass

residue, defined as the residue dry mass at a given time point over the original dry weight

of the sample, was plotted over time. The microstructures of POSS-SMPs retrieved from

PBS at various time points were examined on a Quanta 200 FEG MKII SEM (FEI Inc.).

The samples were sputter-coated with Au and imaged under high vacuum at 10kV.

2.3 Study design and surgical procedure

All animal procedures were approved by the University of Massachusetts Medical

School Animal Care and Use Committee. Briefly, male Charles River SASCO-SD rats

(289-300 g) were sedated by 5% isoflurane-oxygen and then maintained by 2%

isoflurane-oxygen throughout the surgery. A small ventral incision (~1cm) was made to

create a subcutaneous pocket to place a thin piece of POSS-SMP of a given PLA arm

length (POSS-SMP-10, -20, or -40) or commercial amorphous *DL*-PLA pellets of the

same weight, then closed with a surgical staple. Up to 6 pockets were created in each rat

for implantation, and the implants were retrieved at 4-, 18-, 60-, or 164-day post-op for

histology (N = 3). A subset of POSS-SMP-10 was implanted for 1 year to examine the long-term effects of implantation. Heart, kidney, lung, liver, spleen and bone marrow from rib were collected from the rats receiving POSS-SMP-10 for 164-day and 1 year to examine potential systemic side effects of implant degradation to scavenger and vital organs. Note that no animals were lost or prematurely sacrificed due to substantial adverse reactions (e.g. tumor formation or unresolved infections) during the course of the study

2.4. Implant and organ retrieval and histological examinations

Subcutaneous implants and organs were retrieved from the rats sacrificed at pre-determined time points, and fixed in a periodate-lysine-paraformaldehyde fixative[123] at 4 °C for 1 and 2 days, respectively. The internal organs were grossly inspected at the time of sacrifice for tumor formation. Paraffin sections (5 μm) of the subcutaneous explants were stained for Ki67, a marker for cell proliferation, and with hematoxylin and eosin (H&E). Paraffin sections (5 μm) of the retrieved organs were stained with H&E. All histology slides were blind-assessed by a pathologist. A total of twenty-seven 5-μm sections of each sample (9 sections per specimen, three specimens per sample) per time point were stained for H&E or Ki67. Five randomly selected 400× fields of view (FOV) among the H&E sections were examined in detail to tally the number of lymphocytes, macrophages, mast cells, eosinophils, and neutrophils for each sample at each time point. Blood vessel counts were tallied in the most active 400× FOVs. All cell types and blood

vessels were quantified based on morphology. All cell and blood vessel counts were reported as average ranges per FOV in Tables 4.1 and 4.2.

3. Results

3.1 PLA chain length-dependant hydrolytic degradation kinetics

The choice of the racemic *DL*-PLA instead of the *L*-PLA in the design of POSS-SMP was based on the needs for both lowering the T_{trans} to a physiologically safe range and avoiding crystalline degradation products that may elicit undesired *in vivo* responses [162]. Here we show that by adjusting the length of the *DL*-PLA arms attached to the POSS core, the hydrolytic degradation rates of POSS-SMP nanocomposites can be engineered. As shown in Figure 4.1B, whereas POSS-SMP-10 and POSS-SMP-20 lost 50% of their original masses in 3 months in PBS (with substantial increase in scaffold porosity, Fig. 1C), POSS-SMP-40 reached 50% degradation in 7 months. It is worth noting that all POSS-SMPs examined exhibited a stable "lag" phase in mass reduction (2-6 months) before entering a rapid "log" phase of mass reduction leading to significant structural disintegration (Figs. 4.1B & C). Such a degradation profile is reciprocal to those exhibited by most soft and hard tissue repairs where a latent phase often precedes a more rapid increase in tissue structural integrity as qualitatively depicted by the purple trend line in Figure 4.1B [163, 164].

3.2 Immune responses 4 to 60 days post-implantation

All POSS-SMPs and PLA control elicited a mild foreign body type immune response upon subcutaneous implantation in rats prior to the onset of detectable degradation. As representatively shown in Figure 4.2A and Table 4.1, POSS-SMP-10 harvested 4 days post implantation was surrounded by a fibrous tissue capsule where macrophages, abundant and active capillaries (as indicated by the "plump" endothelial cells lining the vessels) and lymphocytes were detected, indicative of a typical foreign body response. Ki67 staining showed that >80% of the cells within the newly formed fibrous tissue capsule were proliferating at this early time point. The early tissue responses to POSS-SMP-10 appeared to be milder than those observed with the PLA control, with the tissue capsule of the latter characterized with more abundant macrophages and lymphocytes, as well as the presence of neutrophils (Fig. 4.2B; Table 4.1). No significant hypersensitivity reaction to either POSS-SMP-10 or the PLA control was detected, as supported by the presence of very few mast cells or eosinophils surrounding the implant.

Figure 4.2. Foreign body type responses to (A) POSS-SMP-10 and (B) PLA control at 4, 18 and 60 days post subcutaneous implantation as revealed by H&E (cellularity) and Ki67 (proliferation) immunostaining. Center rows are higher resolution images of the areas boxed in the top row. Birefringent images of the fibrous capsules surrounding POSS-SMP-10 are shown as insets. Scale bars: 200 μm. BV = blood vessel; L = lymphocyte; M = macrophage; F = fibroblast; N = neutrophil.

Table 4.1. Quantifications of immune responses to POSS-SMP-10 vs. PLA control at 4, 18 and 60 days post subcutaneous implantation. Each cell type was counted with H&E staining in five randomly selected 400× field-of-view (FOV) and reported as average ranges per FOV. Blood vessels were counted in the 400× FOVs with the most densely populated blood vessels.

Days	Implant	[1]Blood Vessel	[2]%Ki67^{+}	[3]Lymphocyte	[4]Macrophage	Mast	Eosinophil	Neutrophil	[5]Implant Degradation
4	POSS-SMP	++	+++	++	++	1-2	1-2	0	-
	PLA	++	+++	++	+++	1-2	1-2	>5	-
18	POSS-SMP	+	-	+	+	0	3-10	0	-
	PLA	++	+	+	++	0	0	0	-
60	POSS-SMP	++	++	+	++	0	0	0-1	+
	PLA	++	-	+	+	0-6	0	0	-

[1]Blood Vessels: <20/FOV (+), 20-50/FOV (++), >50/FOV (+++); [2]%Ki67^{+} cells: <5% (-), 5-20% (+), 20-50% (++), >50% (+++); [3]Lymphocytes: <5/FOV (-), 5-20/FOV (+), >20/FOV (++); [4]Macrophages: <5/FOV (-), 5-20/FOV (+), 20-50/FOV (++), >50/FOV (+++); [5]Implant degradation: no degradation (-), onset of degradation with minor microscopic structural changes (+), partial degradation with obvious macroscopic and microscopic structural disintegration (++), near to complete degradation (+++).

By 18 days post implantation, a more mature fibrous tissue capsule characterized by aligned extracellular collagen fibers embedded with spindly fibroblasts surrounding both POSS-SMP-10 and the PLA control. The numbers of proliferating (Ki67 positive) cells, macrophages, lymphocytes, and blood vessels within the fibrous capsules surrounding both implants significantly decreased, but the overall immune responses to PLA remained stronger (Fig. 4.2; Table 4.1). No acute inflammatory response was detected at this time point in either POSS-SMPs or the PLA control, as supported by the absence of neutrophils.

By 60 days, while the number of proliferating cells, macrophages and blood vessels surrounding the PLA control continued to decrease, the onset of the degradation of POSS-SMP-10, indicated by the opaque appearance of the once transparent material, elicited a second inflammatory response. The small number of macrophages, proliferating fibroblasts and blood vessels surrounding POSS-SMP-10, however, was not accompanied by lymphocytes or neutrophils (Fig. 4.2A; Table 4.1). The fibrous capsule also remained well-aligned (as indicated by the birefringence of collagen fibers, inset of Fig. 4.2A), suggesting that the increase in tissue activity was limited at this time point. Finally, while masts cells were observed surrounding the PLA, no allergic reaction to POSS-SMP-10 was detected by 60 days.

3.3 Degradation-induced immune responses at 164 days

By 164 days post implantation, all POSS-SMPs degraded, with the extent of the structural disintegration and the degree of the corresponding acute inflammatory tissue

response inversely correlated to the PLA chain length of the nanocomposite. Similar to the trend observed with the *in vitro* hydrolytic degradation, POSS-SMP-10 degraded the fastest *in vivo*. The second acute inflammatory response to the degradation was the most abundant surrounding POSS-SMP-10 at day 164, with significantly more actively proliferating capillaries, macrophages, and neutrophils detected within its tissue capsule (Fig. 4.3; Table 4.2). This second acute inflammatory response to the extensive degradation of POSS-SMP-10 was also accompanied by mild allergic/hypersensitivity reaction to the degradation products as indicated by the presence of a small number of mast cells and eosinophils. The more abundant inflammatory cell activities within the fibrous capsule of POSS-SMP-10 also led to a drop of the intensity of birefringence (in yellow) as its collagen alignment was more profoundly disrupted than those surrounding POSS-SMP-20 or POSS-SMP-40 (Fig. 4.3, first row insets).
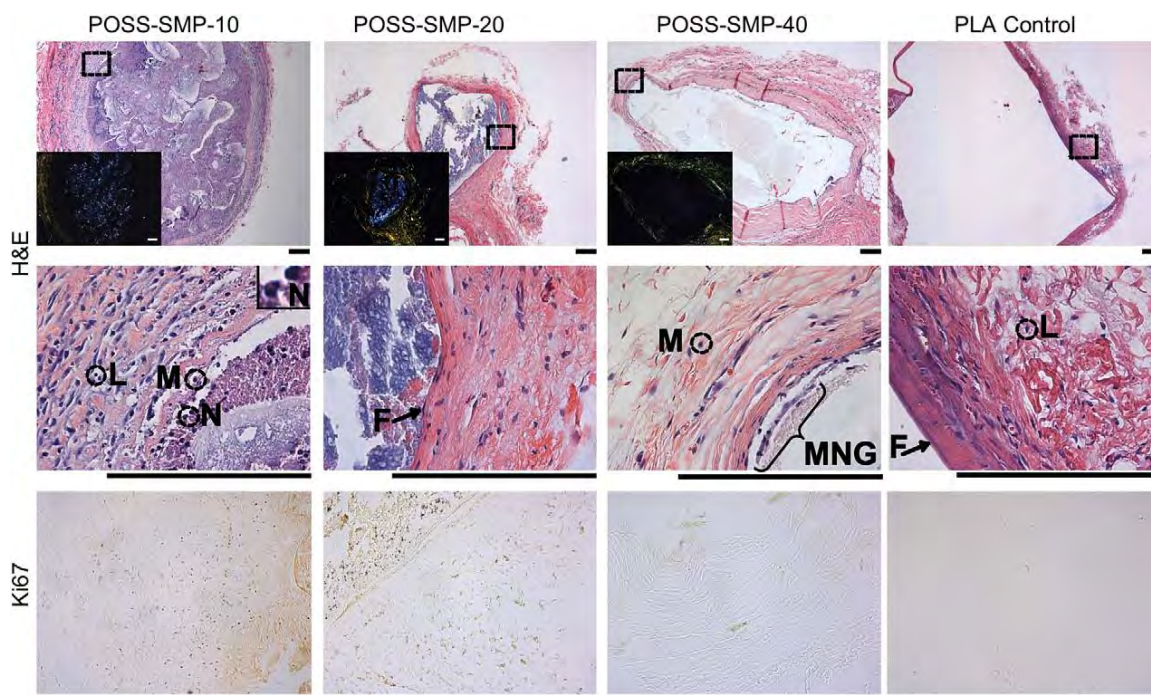
Figure 4.3. Inflammatory responses to POSS-SMP-10, POSS-SMP-20, POSS-SMP-40 and the PLA control at 164 days post subcutaneous implantation as revealed by H&E (cellularity) and Ki67 (proliferation) immunostaining. Center rows are higher resolution images of the areas boxed in the top row. Birefringent images of the fibrous capsules surrounding POSS-SMPs are shown as insets. Scale bars: 200 μm. BV = blood vessel; L = lymphocyte; M = macrophage; F = fibroblast; N = neutrophil; MNG = multi-nucleated giant cell.
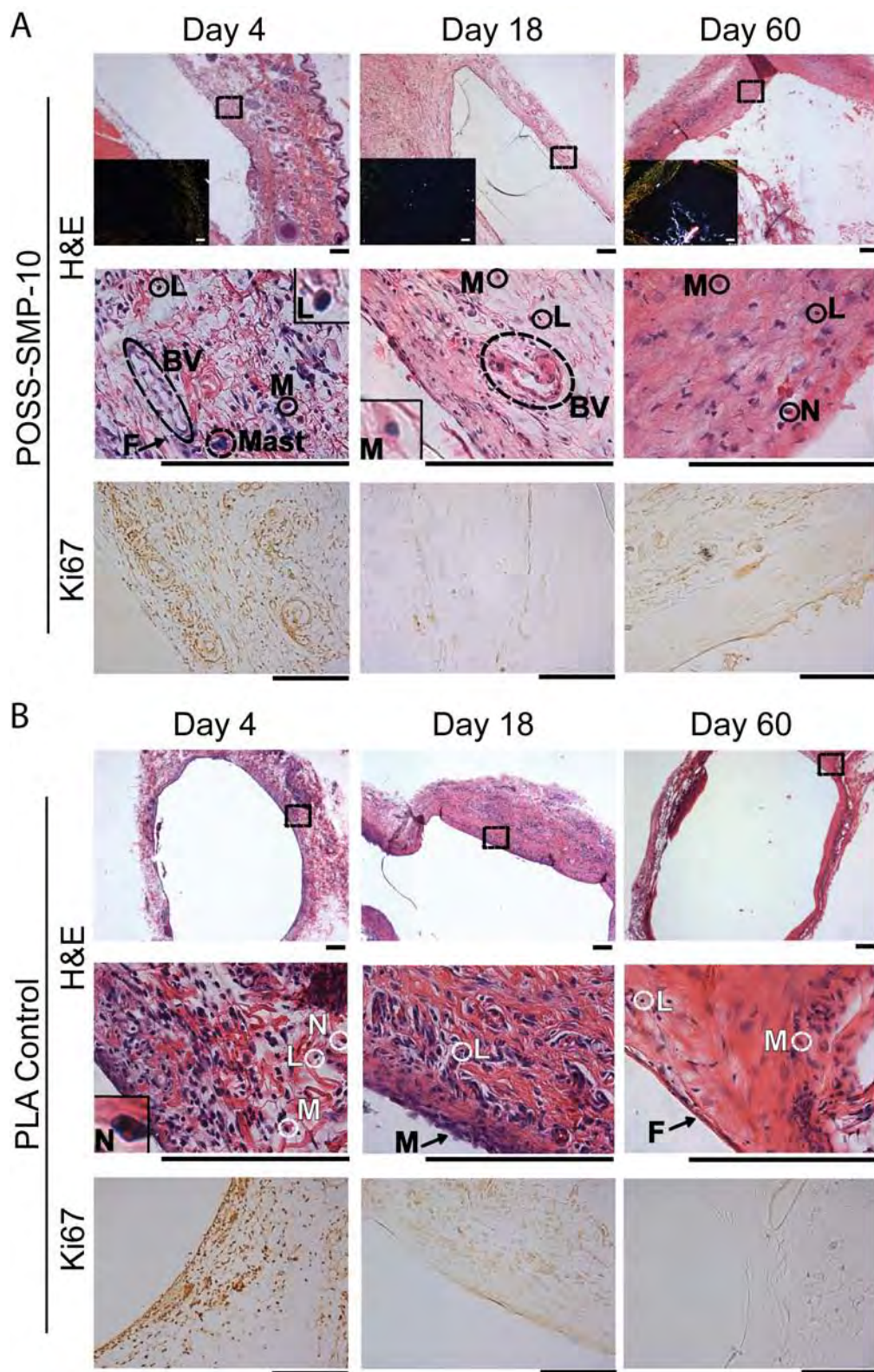
Table 4.2. Quantifications of immune responses to POSS-SMP-10, POSS-SMP-20, POSS-SMP-40 and PLA control at 164 days post subcutaneous implantation. Each cell type was counted with H&E staining in five randomly selected 400× field-of-view (FOV) and reported as average ranges per FOV. Blood vessels were counted in the 400× FOVs with the most densely populated blood vessels.

Implant	[1]Blood Vessel	[2]%Ki67^{+}	[3]Lymphocyte	[4]Macrophage	Mast	Eosinophil	Neutrophil	[5]Implant Degradation
POSS-SMP-10	+++	++	+	+++	0-2	0-1	>5	+++
POSS-SMP-20	+	-	+	-	0	0	0-1	++
POSS-SMP-40	+	-	-	+	0	0-1	0	+
PLA	++	-	+	-	0-3	0	0	+

[1]Blood Vessels: <20/FOV (+), 20-50/FOV (++), >50/FOV (+++); [2]%Ki67^{+} cells: <5% (-), 5-20% (+), 20-50% (++), >50% (+++); [3]Lymphocytes: <5/FOV (-), 5-20/FOV (+), >20/FOV (++); [4]Macrophages: <5/FOV (-), 5-20/FOV (+), 20-50/FOV (++), >50/FOV (+++); [5]Implant degradation: no degradation (-), onset of degradation with minor microscopic structural changes (+), partial degradation with obvious macroscopic and microscopic structural disintegration (++), near to complete degradation (+++).

3.4 Systemic effects on scavenger / vital organs

Despite the significant *in vivo* degradation of POSS-SMP-10 by 164 days, the rats did not exhibit any signs of distress or infection. The vital organs and scavenger organs retrieved from rats receiving the implantation of POSS-SMP-10 for 164 days and 1 year were pathologically unremarkable compared to age-matched normal control organs as assessed by gross (i.e. no visible tumor formation) and histological inspection (Fig. 4.4). None of the major viscera examined showed any evidence of chronic injury or chronic systemic immune response such as systemic foreign body type granulomatous inflammation.
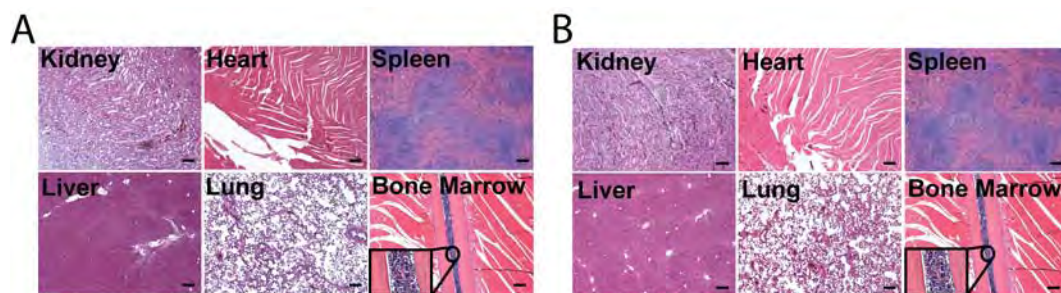
Figure 4.4. H&E stains of vital organs retrieved from rats receiving A) POSS-SMP-10 for 164 days (500×) revealing no systemic side effects, and B) from age-matched rats without implantation. Scale bars = 200 μm.

By 1 year, the POSS-SMP-10 implant was almost completely resorbed, with few immune cells present at the site of implantation and no signs of chronic inflammation. This finding suggests that the second acute immune response to the degradation of POSS-SMPs was able to resolve over time without therapeutic interventions.

4. Discussion

To evaluate the suitability of a degradable synthetic biomaterial for *in vivo* biomedical applications, both its degradation characteristics and the immunogenicities of the biomaterial and its degradation products[165-169] should be considered. Here we show that the hydrolytic degradation kinetics of POSS-SMPs could be tuned by adjusting the length of the PLA arms attached to the star-branched macromer building block. By increasing the number of lactide repeating units of each PLA arm from 10 to 40, the structural stability of the crosslinked POSS-SMP network (the "lag" phase of the mass reduction) could be extended from 2 months to 6 months, which was then followed by a rapid mass reduction phase (Fig. 4.1). This observation suggests that the more densely packed chain structure in POSS-SMP-40 as a result of longer PLA arms and less POSS disruption is more resistant to hydrolytic degradation. The *in vivo* degradation of POSS-SMPs, upon subcutaneous implantation in rats, also followed a similar PLA chain-length dependent profile, with the onset of a late acute inflammatory response to the degradation detected by 60 days for POSS-SMP-10 (Table 4.1) but not until 164 days for POSS-SMP-40 (Table 4.2). Such a tunable degradation profile is desired for their applications as synthetic tissue scaffolds where the structural stability of the scaffolds need to be

sustained for a tailored time period while the structural integrity of the damaged tissue is being restored. The rates of tissue repair often vary depending on the anatomic location of the tissue defect as well as the age and metabolic conditions of the patient. For instance, in children, long bone fractures are typically bridged in 5-14 weeks, with the remodeling of new bone peaking at 9 weeks.[170] The bridging of adult long bone fractures typically take up to 16 weeks with its remodeling lasting up to 1-4 year.[163] The tunable degradation rates of POSS-SMPs, along with their cortical bone-like mechanical strength at the body temperature prior to degradation,[156], make them appealing candidates as synthetic bone scaffolds for the treatment of hard-to-heal bony lesions.[171]

Four days after subcutaneous implantation, POSS-SMPs elicited a normal foreign body type immune response,[172] as characterized by proliferating fibroblasts and mononuclear macrophages and multinuclear giant cells at the implant/tissue interface. No acute (neutrophils) or notable allergic responses (few mast cells or eosinophils) were detected. By 18 days, as the initial immune response to the foreign material subsided and the fibrous tissue capsule matured, the number of inflammatory cells, proliferating fibroblast, and blood vessels significantly decreased (Table 4.1). In comparison, the PLA control elicited a stronger inflammatory response than the POSS-SMPs at these early time points, with more macrophages and the presence of neutrophils detected at day 4, and more abundant blood vessels and proliferating cells at day 18 (Table 4.1). Overall, POSS-SMPs appeared to be minimally immunogenic and did not elicit allergic reactions upon implantation.

The degradation products of POSS-SMPs elicited a late acute inflammatory response characterized with the presence of neutrophils and an increase in overall cellular activities within the fibrous tissue capsule. This newly activated immune response, elicited by the acidic degradation products (e.g. lactic acid), was also accompanied by a decrease in the intensity of the birefringence of the fibrous tissue capsule as the penetrating immune cells disrupted the packing and alignment of collagen fibers. No local tissue necrosis or negative systemic impact on scavenger organs such as lung, liver, kidney, bone marrow and spleen were observed as a result of the degradation of POSS-SMPs. This observation may suggest that the degradation products did not reach systemic circulation or distant organs, and were cleared *in-situ* at the site of implantation. More importantly, this late acute inflammatory response induced by the degradation products was able to resolve on its own without the need for medical interventions. Clinically, aseptic sinus / inflammatory abscess formations as a result of more severe acute inflammatory response will require treatment, but the late acute inflammatory response in the experimental animals in the current study did not reach this degree of severity. It is worth noting that by physically incorporating additives (such as calcium phosphates) that can neutralize the acidic degradation products of the polyester component, the acute inflammatory response induced by the degradation of POSS-SMPs may be further mitigated.

5. Conclusion

We have shown that POSS-SMPs, a class of biodegradable thermal responsive shape memory polymers derived from star-branched building blocks containing POSS nanoparticle cores and polyester arms, elicited a mild foreign body type immune response upon subcutaneous implantation in rats. The degradation rates of POSS-SMPs, both *in vitro* and *in vivo*, inversely correlated with the length of the polyester chains within the crosslinked amorphous network. Upon degradation, a secondary acute inflammatory response was elicited locally at the implantation site, and the inflammation was able to resolve over time without medical interventions. No systemic pathologic abnormities were detected, as supported by the normal examination of bone marrow, heart, kidney, lung, liver, or spleen even one year after the implantation of POSS-SMPs. Coupled with their tunable mechanical properties and chemical functionalizability, POSS-SMPs may be explored for a wide range of *in vivo* applications (e.g. as orthopedic implants, vascular stents or other tissue scaffolds). However, pre-clinical animal studies using surgical models relevant to the intended applications as well as a full toxicology analysis will be necessary. Immunological staining of tissue sections to identify specific immune cell populations is also desired.

Chapter V: Conclusions and Future Perspectives

1. Summary of thesis work

The previous chapters highlight a number of 2-D and 3-D scaffolds designed to mimic key structural and biochemical properties of target skeletal tissues in easy-to-fabricate and scalable biocompatible materials. In Chapter 2, a 3-dimensional elastomeric hydrogel – nHA scaffold named FlexBone was shown to enable the functional healing of 5-mm critical-size femoral segmental defects in rats by 8 – 12 weeks when it was press-fit within the defect with a single low dose of rhBMP-2/7. FlexBone locally delivered rhBMP-2/7, likely as a result of the physical adsorption/desorption of rhBMP-2/7 on/from the large surfaces of nHA, which could undergo dynamic surface charge changes as the pH within the tissue microenvironment fluctuates in response to cellular activities. Such unique surface properties of the nHA component also enabled FlexBone to sequester and enrich endogenous proteins, leading to partial healing of the defect in the absence of any exogenous growth factors. This work supports that FlexBone can be engineered to possess key properties of structural bone allografts such as osteoconductivity and structural stability, yet also exhibit attractive features that are commonly lacking in bone allografts. Among them, easy surgical handling due to its compressibility, ability to delivery growth factors to acquire osteoinductity, its inexpensive and scalable fabrication, and its convenient storage at ambient conditions

make it uniquely suited as an "off-the-shelf" product with excellent clinical translatability.

Comparing to 3-D tissue scaffolds, 2-D scaffolds have the advantages of ease of cell seeding and its complementary physical properties to 3-D scaffolds. They may be used in combination with 3-D scaffolds to deliver multiple cells or therapeutics to accomplish spatial and temporal control over the delivery/release kinetics. In Chapter 3, we demonstrated that a sulfated 2-D fibrous mesh scaffold can be fabricated by electrospinning cellulose acetate in combination with subsequent chemical modifications. The sulfated residues are inspired by sulfated polysaccharides richly present in the extracellular matrix environment of bone and cartilage tissues, which exhibit high affinity for many endogenous proteins. We showed that this sulfated fibrous mesh can serve as a delivery vehicle for several growth factors including rhBMP-2, VEGF and IGF-1 (Figs. 3.4 and 5.1) and retained their bioactivity after one week incubation in PBS. We also showed that bone marrow stromal cells could readily attach to the mesh surface, and undergo differentiation to osteogenic lineage under the induction of pre-absorbed osteogenic factors. These easy-to-fabricate cytocompatible meshes could be used for therapeutic and cellular delivery *in vivo* either as a stand-alone platform or in combination with other 3-D tissue grafts.

Figure 5.1. Retention/release profile of VEGF (top) and IGF-1 (bottom) on/from SC vs. RC meshes. The mesh (N=3) was pre-absorbed with VEGF or IGF-1 (27 ng/cm^2) and air-dried before being incubated in PBS at 37 °C for 7 days. The protein released in PBS at a given time was quantified by ELISA.
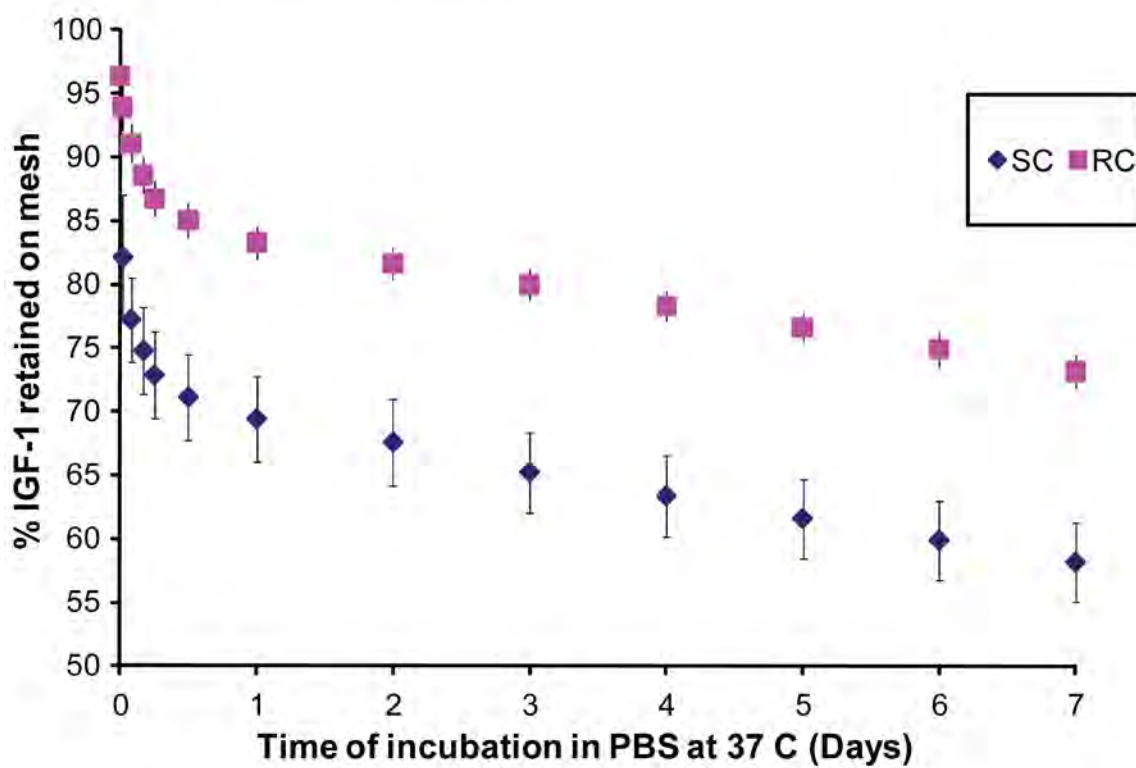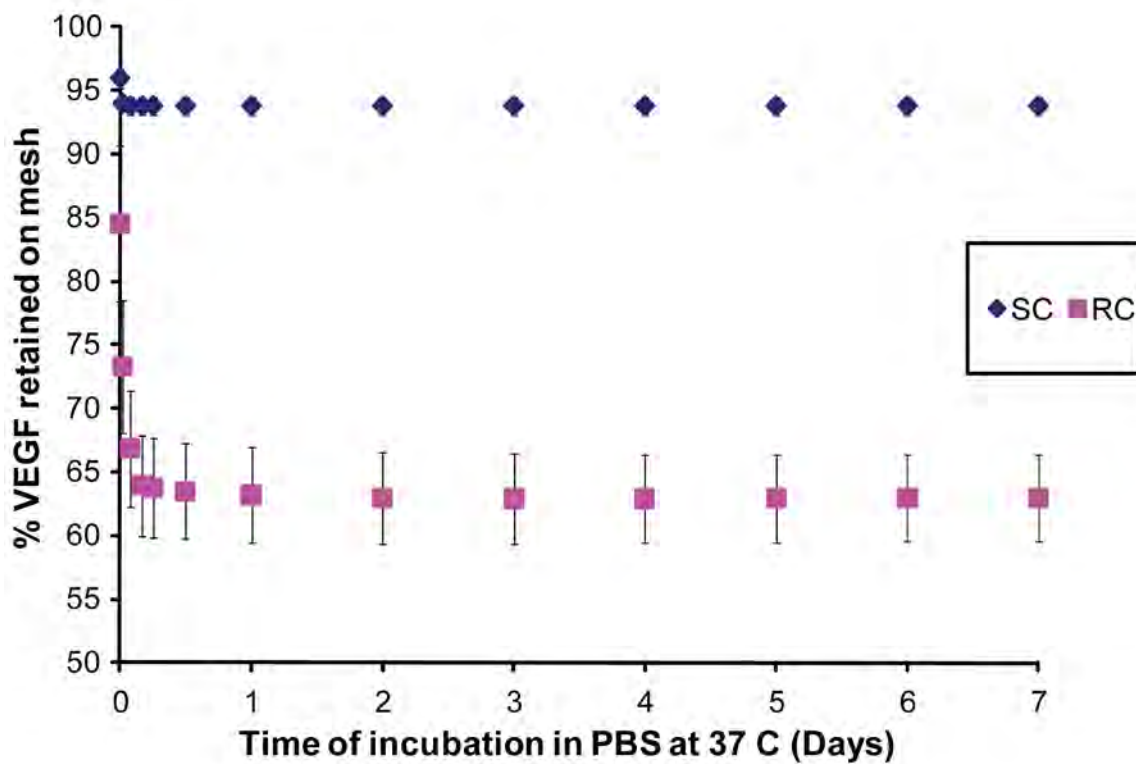
In Chapter 4, we describe a method for evaluating the biocompatibility of a novel 3-D scaffold developed in our lab for minimally invasive surgical use.[156] Using a rat subcutaneous implantation model, a thermal-responsive shape memory polymer (POSS-SMP) crosslinked from macromers containing a polyhedral oligomeric silsesquioxane (POSS) core and 8 biodegradable poly(D,L-lactide) (PLA) arms was evaluated for its immunogenicity as a function of its PLA arm lengths. We showed that all POSS-SMPs elicited normal foreign body immune responses upon initial implantation and a secondary acute immune response upon their in vivo degradation. The severity of the secondary acute immune response increased with those with shorter PLA arms (thus faster degradation rates) but could resolve on its own over time without need for any medical intervention. No systemic side effects were observable one year after the implantation when vital and scavenger organs were inspected both grossly and microscopically. This study has established a much-needed method for examining the biocompatibility of degradable biomaterials that can benefit subsequent novel biomaterials development and characterizations.

2. Ongoing work and future directions

Two major directions we are currently pursuing towards the translation of FlexBone and the sulfated fibrous mesh for treating challenging orthopedic conditions are the use of FlexBone to treat hard-to-heal diabetic bony lesion and the use of the 2-D sulfated fibrous

cellulose mesh as a "synthetic periosteum" to augment the healing of structural bone allografts.

With the success of FlexBone as a 3-D synthetic bone graft in facilitating the healing of critical-size long bone defects in normal rats, we are seeking to extend its use to aid healing in clinically relevant hard-to-heal defects as a result of an interfering metabolic condition. g. Diabetes is a metabolic disease which affects approximately 25.8 million, or 8.3% of the population in the United States, costing the US economy approximately $174 billion per year.[173] A well-known complication with diabetes is impaired wound healing, which is likely the result of several complex factors, such as risk for infections, poor circulation, peripheral neuropathy, and lack of growth factors needed for wound healing and vessel growth.[174-176] Bony healing in diabetic patients is especially challenging.[177] Many theories for impaired bone healing are being studied. For example, the role of accumulated advanced glycation end products (AGEs) seen in some diabetic tissues may play a role in impairing bony healing.[178] A role for insulin in regulating fracture healing in type 1 diabetes has been suggested by a mouse study. The diabetic femoral fractures showed increased chondrocyte apoptosis and increased osteoclastic activity at the site of fracture, which were linked to the impaired healing, and was shown to be rescued to some extent by insulin treatment.[179, 180] Insulin regulation was also shown by others to aid bone healing in type 1 diabetic rats.[181] Lin and coworkers have shown that locally delivered insulin therapy led to more robust fracture healing in type 1 diabetic rats.[182, 183] Some evidence for decreased osteoblastic differentiation has also been presented in a type

1 diabetic mouse model.[184] Delivery of osteogenic protein BMP-7 has been shown to enhance fracture healing in diabetic rats, supporting this theory.[185] Further, low levels of endogenous growth factor IGF-1 in diabetic patients may also compromise the healing of bone, as low IGF-1 has been associated with reduced collagen deposition, angiogenesis and leukocyte infiltration – all processes critical for healing – and local administration of exogenous IGF-1 has been shown to aid both diabetic soft tissue repair and bone repair in diabetic rats.[186, 187] Finally, local delivery of VEGF that is known to be deficient in diabetic wounds has also been shown to expedite soft tissue repair via neovascularization and stem cell recruitment.[188] We hypothesize that a combination delivery of IGF-1,VEGF along with an osteogenic factor, such as BMP-2/7, could significantly expedite repair of bone in diabetic rats.

To test this hypothesis, we chose to use Diabetic Prone Bio-Breeding/Worcester (BBDP) rats. BBDP rats are the most extensively studied strain of spontaneous type I diabetic rat model characterized by a predisposition to autoimmune beta cell destruction and T cell lymphopenia.[189] These rats experience an average onset of diabetes between 50 and 90 days of age, at an incidence of 85 – 90%.[190] To our knowledge, the bone phenotype of BBDP rats has not been well-characterized; however, there has been some work performed with BBDP soft tissue wound and bone repairs. Our ongoing and future work with this type 1 diabetic rat model involves the validation of the retarded bone healing in BBDP rats, the characterization of the bone phenotype of BBDP rats, and the use of FlexBone in combination with multiple factors to "rescue" its bony healing.

We performed a series of pilot surgeries to create 5-mm femoral segmental defects in BBDP rats with poorly controlled blood glucose levels (BG maintained by an insulin implant at 250-400 mg/dL) and press-fit FlexBone with or without a single dose of 400-ng BMP-2/7 within the surgical defect as previously described.[67] In contrast to previous findings with non-diabetic SASCO SD rats where FlexBone led to partial or complete healing of the femoral defect in combination with 0 or 400-ng BMP-2/7, these diabetic bony lesion did not heal at all when press-fit with FlexBone regardless whether 400-ng BMP-2/7 was supplemented, as shown by histology, X-ray and microCT analyses. Supplementing FlexBone with 300-ng IGF-1 also did not lead to any detectable healing. To understand this impaired healing and to justify the choice of exogenous factors to supplement in subsequent experiments, we examined if any endogenous crucial factors needed for the initiation of bone healing are recruited to the defect site in a delayed or compromised manner in BBDP rats. To do this, we press-fit FlexBone into the site of femoral defect and retrieved FlexBone at various time points over a period of 1 week following the surgery. These samples were then histologically stained for key inflammatory (VEGF, IL-1β, TNFα, TGFβ), bone remodeling (BMP-7, BMP-2, RANKL, VEGF), stem cell recruitment (SDF-1) and growth/differentiation (IGF-1) factors. When comparing the endogenous factors recruited to/absorbed by FlexBone in diabetic BBDP rats vs. in SASCO SD rats, not only is there an observable decrease in the amount of proteins detected at earlier time points, but also a delayed "peak" in detecting all the proteins examined (**Fig. 5.2**). Of particular interest is the expression of TGF-β,

which plays a critical role in triggering early healing, peaks at 2 days in SASCO SD rats but not until one week in diabetic BBDP rats. These results give clues as to how complex rescuing diabetic bony healing can be. Currently, we are searching for growth factor combinations that can lead to synergistic enhancement of osteogenesis of MSCs *in vitro.* Preliminary results using the C2C12 osteogenic trans-differentiation model and osteogenic differentiation of rat bone marrow stromal cells show that combinations of BMP-2/7 with VEGF had a synergistic effect at a number of dose combinations, especially with 100-ng/mL BMP-2/7 plus 5-15-ng/mL VEGF in rat bone marrow stromal cell culture. The combination of BMP-2/7 with IGF-1 appeared to have little synergistic or inhibitory effect with bone marrow stromal cells, but appeared to be synergistic with the osteogenic trans-differentiation of C2C12 cells at certain dose combinations, most notably with 40-ng/mL BMP-2/7 plus 10-ng/mL IGF-1. Future work will also explore the supplementation of other factors that were expressed in a retarded manner at the defect site in diabetic BBDP rats as shown in Figure 5.2.
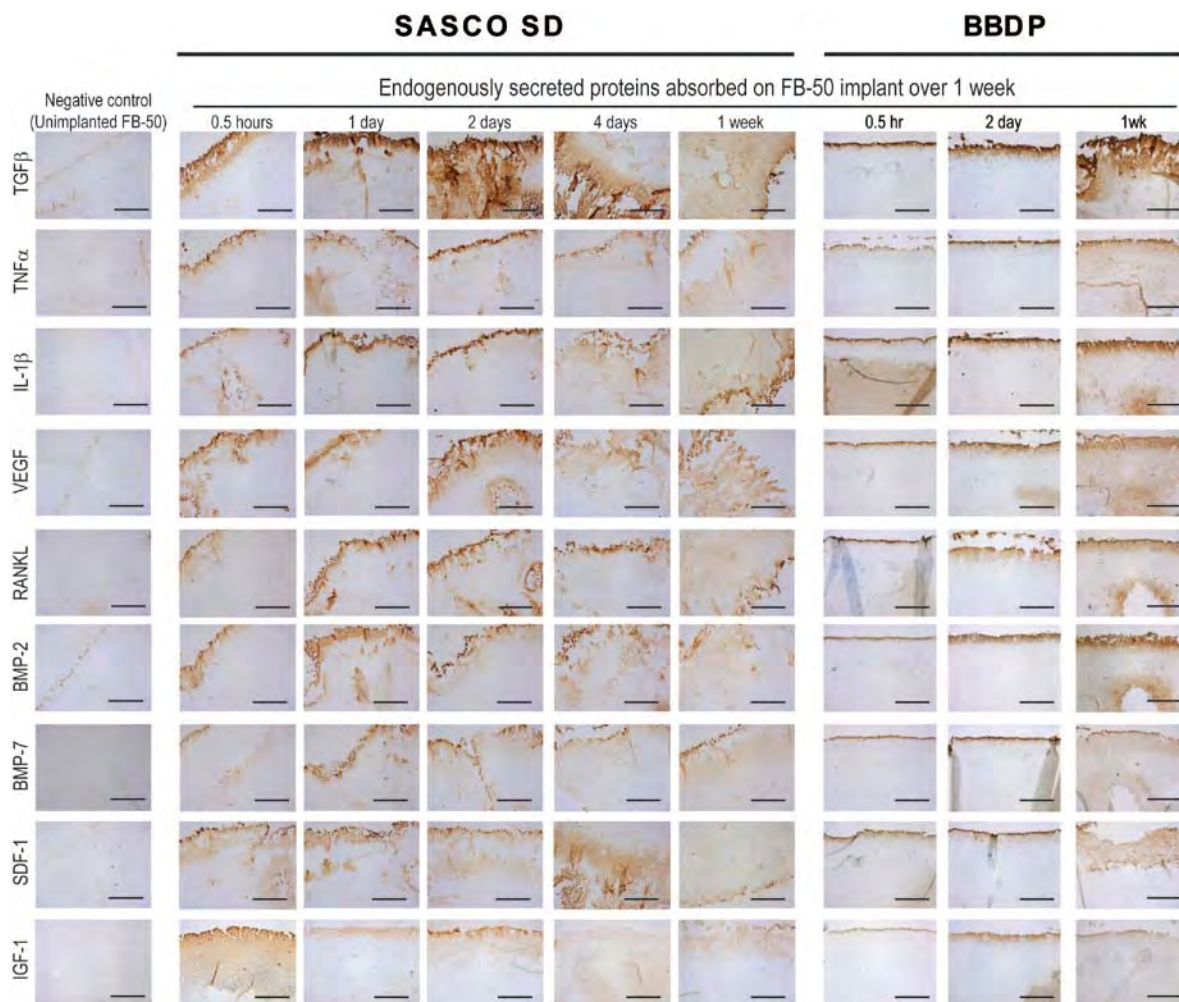
Figure 5.2. Immunohistological detection for endogenous proteins absorbed on FlexBone retrieved at various time points over 1 week after being press-fit into 5-mm femoral segmental defects in non-diabetic SASCO SD or diabetic BBDP rats. Scale bars = 200 μm.

A combination of microCT and torsion testing is being performed on explanted femurs collected from various-aged (up to 1 year old) diabetic and non-diabetic BBDP rats. In addition, we are performing ELISAs to characterize serum markers of bone turnover, TRAP as a readout for osteoclast number and collagen fragments as a readout for osteoclastic activity; pro-collagen synthesis as a readout for osteoblastic activity (Catalog numbers AC-33F1, SB-TR103, AC-06F1, Immuno Diagnostic Systems, Scottsdale, AZ). Preliminary results with a sample size of 4 did not reveal any significant difference in cortical bone volume, thickness, density and bone volume fraction between diabetic and non-diabetic BBDP rats. Non-diabetic BBDP rats appear to have slightly higher trabecular bone volume and thickness as compared to the diabetic BBDP rats while no differences in trabecular bone density and bone volume fraction. Larger sample sizes applied to both the microCT analysis and subsequent torsional tests will be necessary to draw statistically significant conclusions.

Another on-going effort is to explore the use of 2-D sulfated fibrous mesh as a "synthetic periosteum" to augment structural bone allograft healing. Periosteum is a thin membrane covering bone which plays a critical role in bone growth and healing. It is divided into 2 distinct layers: an outer fibrous layer consisting of fibroblasts, collagen, elastin fibers, nerves and blood vessels and an inner cambium layer consisting of nerves, blood vessels, and periosteal stem cells.[191, 192] Devitalized structural bone allografts lose this important component of bone, making their incorporation with surround tissue hard to achieve and resulting in high (50%) graft failure rates. Methods for augmenting bone allograft-

mediated healing include gene therapy approaches, local delivery of protein therapeutics, and the use of pluripotent stem cells.[193-197 77 198]

We hypothesize that a synthetic periosteum recapitulating some of the key components of periosteum can be wrapped around allograft to improve their graft healing. Indeed, prior studies have shown that wrapping devitalized bone allografts with live periosteum transplants did improve graft healing,[199] and that the periosteal stem cells were likely responsible for the majority of the rescued allograft incorporation.[200] A tissue-engineered periosteum fabricated from a porcine small intestinal submucosa scaffold seeded with rabbit mesenchymal stem cells was also reported to augment segmental defect healing.[201] Guldberg and colleagues showed that devitalized mice bone allograft incorporation and healing can be aided when the grafts were wrapped with gelfoam strips pre-seeded with BMP-2 producing bone marrow cells, suggesting an opportunity for a synthetic version of periosteum in bony tissue repair.[200]

Bone allograft healing occurs through a combination of endochondral ossification and intramembranous bone formation.[193] Sulfated glycosaminoglycan (GAG) chondroitin sulfate has been previously shown to enhance bone healing.[202] Other studies from our lab have shown that sulfated residues decorated on polymeric scaffolds may be advantageous in promoting the chondrogenesis of MSCs. We hypothesize that the sulfated cellulose mesh described in Chapter 3 may be used to augment the allograft graft healing by more effectively inducing the endochondral ossification process. In addition, we hypothesize

that the addition of growth factor therapeutics and pluripotent bone marrow stromal cells, both supported by the sulfated fibrous mesh, could further enhance the graft healing.

All allografts used in the pilot study were devitalized by removing the periosteum and bone marrow, followed by rinses in PBS and 70% ethanol and freezing at -80 ℃ for at least 24 hours prior to use. A 5-mm femoral segmental defect was surgically created in SASCO SD rats, which was then tight-fit with a devitalized femoral allograft and wrapped with the 2-D synthetic periosteum as shown in Figure 5.3.
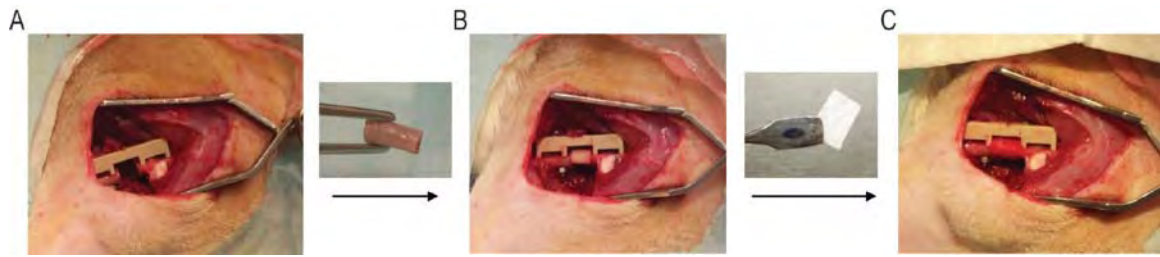
Figure 5.3. Surgical scheme for a femoral segmental defect fit with a devitalized bone allograft wrapped with synthetic periosteum. A) A radiolucent PEEK plate fixator was attached with bicortical screws to the exposed femur (periosteum was circumferentially removed) and a 5-mm mid-diaphyseal defect was generated under the plate fixator with an oscillating Hall saw with parallel blades. B) A devitalized bone allograft was tight-fit into the site of defect without additional support. C) A 9-mm × 7-mm film of synthetic periosteum was wrapped around the allograft with or without the addition of exogenous protein therapeutics or MSCs. Devitalized allografts wrapped with the synthetic periosteum pre-loaded with various doses of rhBMP-2 (0-ng, n=3; 750-ng, n=1; 1500-ng, n=2; and 3000-ng, n=2) showed that while limited bony bridging was observed without the addition of BMP-2 at 8 week post-operation, extensive bridging by healing callus occurred with the addition of 1500- and 3000-ng BMP-2 (Fig. 5.4).
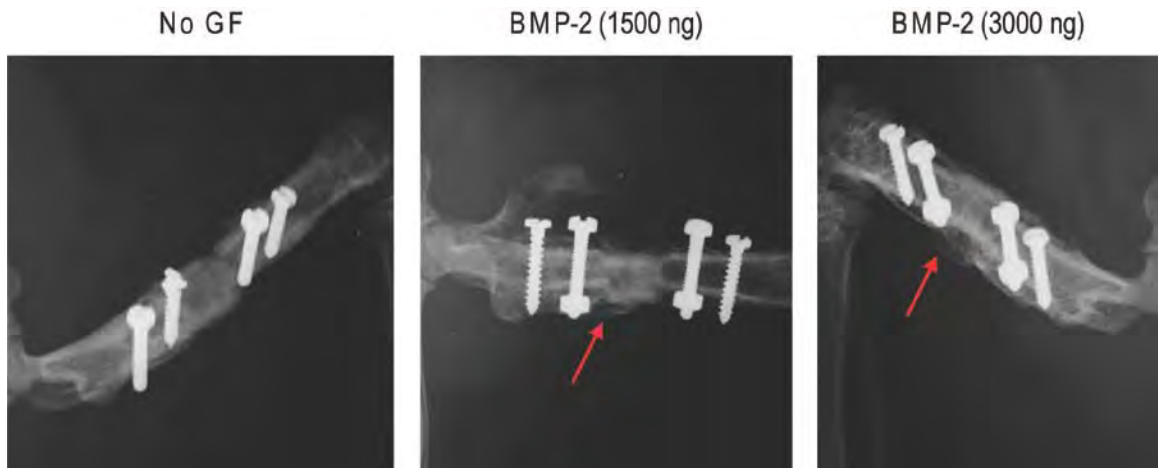
Figure 5.4. At 8 weeks post-operation, x-ray radiography revealed varying levels of bony bridging (red arrows) over the femoral defects filled with devitalized allografts wrapped with synthetic periosteum pre-loaded with 0 (no growth factor), 1500-ng, or 3000-ng rhBMP-2.

The sample size of these experiments are being increased to N=7 to ensure that subsequent analyses by histology, microCT and torsional tests can be carried out to reach statistically significant conclusions. Future experiments will also involve addition of other growth factors (i.e. VEGF) and rat bone marrow stromal cells (rMSCs) to the 2-D scaffold to further expedite the graft healing. Immunogenicity of the synthetic periosteum will also be examined.

3. Concluding remarks

There has been many exciting developments in the orthopedic biomaterial community. However, very few of these biomaterials has been translated to clinical use, as they tend to be either too complicated in design or lack key properties needed for resulting in successful bone healing clinically (i.e. biocompatibility, suitable structural and biochemical properties, ideal surgical handling properties). The work presented in this dissertation illustrates that by recapitulating the multifaceted roles that key extracellular matrix components of bone play in defining bone-specific structural and biochemical properties, easy-to-prepare biomaterials can be designed to facilitate the functional repair of critical-size bony defects. Such biomaterials have the potential to outperform structural bone allografts, providing much-needed viable synthetic bone graft alternatives. Our work supports the notion that functional sophistication of synthetic tissue grafts is not synonymous with complicated chemical/engineering designs. We believe that by

pursuing such a biomaterial design strategy, bench-to-bedside translation can be expedited to benefit patients.

References

1.   Weinstein, S. 2000-2010: The Bone and Joint Decade. . J Bone Joint Surg Am **82**, 1, 2000.

2.   Bostrom, M.P., and Seigerman, D.A. The clinical use of allografts, demineralized bone matrices, synthetic bone graft substitutes and osteoinductive growth factors: a survey study. Hss J **1**, 9, 2005.

3.   Blokhuis, T.J., and Lindner, T. Allograft and bone morphogenetic proteins: an overview. Injury-International Journal of the Care of the Injured **39**, S33, 2008.

4.   Goldberg, V.M., and Stevenson, S. Bone-Graft Options - Fact and Fancy. Orthopedics **17**, 809, 1994.

5.   Eagan, M.J., and McAllister, D.R. Biology of Allograft Incorporation. Clinics in Sports Medicine **28**, 203, 2009.

6.   Mankin, H.J., Gebhardt, M.C., Jennings, L.C., Springfield, D.S., and Tomford, W.W. Long-term results of allograft replacement in the management of bone tumors. Clinical Orthopaedics and Related Research, 86, 1996.

7.   Salgado, A.J., Coutinho, O.P., and Reis, R.L. Bone tissue engineering: State of the art and future trends. Macromolecular Bioscience **4**, 743, 2004.

8.   Carson, J.S., and Bostrom, M.P.G. Synthetic bone scaffolds and fracture repair. Injury-International Journal of the Care of the Injured **38**, S33, 2007.

9.   Place, E.S., Evans, N.D., and Stevens, M.M. Complexity in biomaterials for tissue engineering. Nat Mater **8**, 457, 2009.

10.   Stevens, M.M. Biomaterials for bone tissue engineering. Materials Today **11**, 18, 2008.

11.   Burg, K.J.L., Porter, S., and Kellam, J.F. Biomaterial developments for bone tissue engineering. Biomaterials **21**, 2347, 2000.

12.   De Long, W.G., Einhorn, T.A., Koval, K., McKee, M., Smith, W., Sanders, R., and Watson, T. Bone, grafts and bone graft substitutes in orthopedic trauma surgery - A critical analysis. Journal of Bone and Joint Surgery-American Volume **89A**, 649, 2007.

13.   Seal, B.L., Otero, T.C., and Panitch, A. Polymeric biomaterials for tissue and organ regeneration. Materials Science & Engineering R-Reports **34**, 147, 2001.

14.   Chan, C.K., Kumar, T.S.S., Liao, S., Murugan, R., Ngiam, M., and Ramakrishman, S. Biomimetic nanocomposites for bone graft applications. Nanomedicine **1**, 177, 2006.

15.   Murugan, R., and Ramakrishna, S. Development of nanocomposites for bone grafting. Composites Science and Technology **65**, 2385, 2005.

16.   Eschbach, L. Nonresorbable polymers in bone surgery. Injury **31 Suppl 4**, 22, 2000.

17.   Kim, M.M., Boahene, K.D.O., and Byrne, P.J. Use of Customized Polyetheretherketone (PEEK) Implants in the Reconstruction of Complex Maxillofacial Defects. Archives of Facial Plastic Surgery **11**, 53, 2009.

18.   Kulkarni, A.G., Hee, H.T., and Wong, H.K. Solis cage (PEEK) for anterior cervical fusion: preliminary radiological results with emphasis on fusion and subsidence. Spine Journal **7**, 205, 2007.

19.   Wang, M. Developing bioactive composite materials for tissue replacement. Biomaterials **24**, 2133, 2003.

20.   Mano, J.F., Sousa, R.A., Boesel, L.F., Neves, N.M., and Reis, R.L. Bloinert, biodegradable and injectable polymeric matrix composites for hard tissue replacement: state of the art and recent developments. Composites Science and Technology **64**, 789, 2004.

21.   Tan, K.H., Chua, C.K., Leong, K.F., Cheah, C.M., Cheang, P., Abu Bakar, M.S., and Cha, S.W. Scaffold development using selective laser sintering of polyetheretherketone-hydroxyapatite biocomposite blends. Biomaterials **24**, 3115, 2003.

22.   Fini, M., Giavaresi, G., Aldini, N.N., Torricelli, P., Botter, R., Beruto, D., and Giardino, R. A bone substitute composed of polymethylmethacrylate and alpha-tricalcium phosphate: results in terms of osteoblast function and bone tissue formation. Biomaterials **23**, 4523, 2002.

23.   Zhang, K., Ma, Y., and Francis, L.F. Porous polymer/bioactive glass composites for soft-to-hard tissue interfaces. J Biomed Mater Res **61**, 551, 2002.

24.   Tanner, K.E. Bioactive ceramic-reinforced composites for bone augmentation. Journal of the Royal Society Interface **7**, S541, 2010.

25.   Aparecida, A.H., Guastaldi, A.C., and Fook, M.V.L. Development of Ultra High Molecular Weight Polyethylene (UHMWPE) Porous Supports for Use as Biomaterial in Osseous Replacement and Regeneration. Polimeros **18**, 277, 2008.

26.   Nandi, S.K., Roy, S., Mukherjee, P., Kundu, B., De, D.K., and Basu, D. Orthopaedic applications of bone graft & graft substitutes: a review. Indian Journal of Medical Research **132**, 15, 2010.

27.   Tanner, K.E. Bioactive composites for bone tissue engineering. Proceedings of the Institution of Mechanical Engineers Part H-Journal of Engineering in Medicine **224**, 1359, 2010.

28.   Rezwan, K., Chen, Q.Z., Blaker, J.J., and Boccaccini, A.R. Biodegradable and bioactive porous polymer/inorganic composite scaffolds for bone tissue engineering. Biomaterials **27**, 3413, 2006.

29.   Miranda, P., Martinez-Vazquez, F.J., Perera, F.H., Pajares, A., and Guiberteau, F. Improving the compressive strength of bioceramic robocast scaffolds by polymer infiltration. Acta Biomaterialia **6**, 4361, 2010.

30.   Kim, S.S., Park, M.S., Jeon, O., Choi, C.Y., and Kim, B.S. Poly(lactide-co-glycolide)/hydroxyapatite composite scaffolds for bone tissue engineering. Biomaterials **27**, 1399, 2006.

31.   Wang, M., and Bonfield, W. Chemically coupled hydroxyapatite-polyethylene composites: structure and properties. Biomaterials **22**, 1311, 2001.

32.   Zhang, R.Y., and Ma, P.X. Poly(alpha-hydroxyl acids) hydroxyapatite porous composites for bone-tissue engineering. I. Preparation and morphology. J Biomed Mater Res **44**, 446, 1999.

33.   Lu, L., Peter, S.J., Lyman, M.D., Lai, H.L., Leite, S.M., Tamada, J.A., Uyama, S., Vacanti, J.P., Langer, R., and Mikos, A.G. In vitro and in vivo degradation of porous poly(DL-lactic-co-glycolic acid) foams. Biomaterials **21**, 1837, 2000.

34.   Ma, P.X., and Choi, J.W. Biodegradable polymer scaffolds with well-defined interconnected spherical pore network. Tissue Engineering **7**, 23, 2001.

35.   Mooney, D.T., Mazzoni, C.L., Breuer, C., McNamara, K., Hern, D., Vacanti, J.P., and Langer, R. Stabilized polyglycolic acid fibre based tubes for tissue engineering. Biomaterials **17**, 115, 1996.

36.   Ishaug, S.L., Crane, G.M., Miller, M.J., Yasko, A.W., Yaszemski, M.J., and Mikos, A.G. Bone formation by three-dimensional stromal osteoblast culture in biodegradable polymer scaffolds. J Biomed Mater Res **36**, 17, 1997.

37.   Wang, Y.W., Wu, Q.O., and Chen, G.Q. Attachment, proliferation and differentiation of osteoblasts on random biopolyester poly(3-hydroxybutyrate-co-3-hydroxyhexanoate) scaffolds. Biomaterials **25**, 669, 2004.

38.   Yoshimoto, H., Shin, Y.M., Terai, H., and Vacanti, J.P. A biodegradable nanofiber scaffold by electrospinning and its potential for bone tissue engineering. Biomaterials **24**, 2077, 2003.

39.   Peter, S.J., Kim, P., Yasko, A.W., Yaszemski, M.J., and Mikos, A.G. Crosslinking characteristics of an injectable poly(propylene fumarate)/beta-tricalcium phosphate paste and mechanical properties of the crosslinked composite for use as a biodegradable bone cement. J Biomed Mater Res **44**, 314, 1999.

40.   Liao, S., Watari, F., Zhu, Y., Uo, M., Akasaka, T., Wang, W., Xu, G., and Cui, F. The degradation of the three layered nano-carbonated hydroxyapatite/collagen/PLGA composite membrane in vitro. Dental Materials **23**, 1120, 2007.

41.   Song, J., Saiz, E., and Bertozzi, C.R. A new approach to mineralization of biocompatible hydrogel scaffolds: An efficient process toward 3-dimensional bonelike composites. Journal of the American Chemical Society **125**, 1236, 2003.

42.   Song, J., Saiz, E., and Bertozzi, C.R. Preparation of pHEMA-CP composites with high interfacial adhesion via template-driven mineralization. Journal of the European Ceramic Society **23**, 2905, 2003.

43.   Song, J., Malathong, V., and Bertozzi, C.R. Mineralization of synthetic polymer scaffolds: A bottom-up approach for the development of artificial bone. Journal of the American Chemical Society **127**, 3366, 2005.

44.   Yoshinari, M., Oda, Y., Ueki, H., and Yokose, S. Immobilization of bisphosphonates on surface modified titanium. Biomaterials **22**, 709, 2001.

45.   Licata, A.A. Discovery, clinical development, and therapeutic uses of bisphosphonates. Ann Pharmacother **39**, 668, 2005.

46.   Bertozzi, C.R., Song, J., and Lee, S.-W. HYDROXYAPATITE-BINDING PEPTIDES FOR BONE GROWTH AND INHIBITION World Intellectual Property Organization, 2006.

47.   Chung, W.J., Kwon, K.Y., Song, J., and Lee, S.W. Evolutionary Screening of Collagen-like Peptides That Nucleate Hydroxyapatite Crystals. Langmuir, dx.doi.org/10.1021/la104757g, 2011.

48.   Bonzani, I.C., George, J.H., and Stevens, M.M. Novel materials for bone and cartilage regeneration. Current Opinion in Chemical Biology **10**, 568, 2006.

49.   Patterson, J., and Hubbell, J.A. Enhanced proteolytic degradation of molecularly engineered PEG hydrogels in response to MMP-1 and MMP-2. Biomaterials **31**, 7836, 2010.

50.   Hartgerink, J.D., Beniash, E., and Stupp, S.I. Self-assembly and mineralization of peptide-amphiphile nanofibers. Science **294**, 1684, 2001.

51.   Jeon, O., Song, S.J., Kang, S.W., Putnam, A.J., and Kim, B.S. Enhancement of ectopic bone formation by bone morphogenetic protein-2 released from a heparin-conjugated poly(L-lactic-co-glycolic acid) scaffold. Biomaterials **28**, 2763, 2007.

52.   Lutolf, M.P., Lauer-Fields, J.L., Schmoekel, H.G., Metters, A.T., Weber, F.E., Fields, G.B., and Hubbell, J.A. Synthetic matrix metalloproteinase-sensitive hydrogels for the conduction of tissue regeneration: Engineering cell-invasion characteristics. Proceedings of the National Academy of Sciences of the United States of America **100**, 5413, 2003.

53.   Lutolf, M.R., Weber, F.E., Schmoekel, H.G., Schense, J.C., Kohler, T., Muller, R., and Hubbell, J.A. Repair of bone defects using synthetic mimetics of collagenous extracellular matrices. Nature Biotechnology **21**, 513, 2003.

54.   Cui, H.G., Webber, M.J., and Stupp, S.I. Self-Assembly of Peptide Amphiphiles: From Molecules to Nanostructures to Biomaterials. Biopolymers **94**, 1, 2010.

55.   Palmer, L.C., and Stupp, S.I. Molecular Self-Assembly into One-Dimensional Nanostructures. Accounts of Chemical Research **41**, 1674, 2008.

56.   Palmer, L.C., Newcomb, C.J., Kaltz, S.R., Spoerke, E.D., and Stupp, S.I. Biomimetic Systems for Hydroxyapatite Mineralization Inspired By Bone and Enamel. Chemical Reviews **108**, 4754, 2008.

57.   Bahney, C.S., Hsu, C.-W., Yoo, J.U., West, J.L., and Johnstone, B. A bioresponsive hydrogel tuned to chondrogenesis of human mesenchymal stem cells. FASEB J **25**, fj.10, 2011.

58.   Weiner, S., Traub, W., and Wagner, H.D. Lamellar bone: Structure-function relations. Journal of Structural Biology **126**, 241, 1999.

59.   Tong, W., Glimcher, M.J., Katz, J.L., Kuhn, L., and Eppell, S.J. Size and shape of mineralites in young bovine bone measured by atomic force microscopy. Calcified Tissue International **72**, 592, 2003.

60.   Follet, H., Boivin, G., Rumelhart, C., and Meunier, P.J. The degree of mineralization is a determinant of bone strength: a study on human calcanei. Bone **34**, 783, 2004.

61.   El-Ghannam, A. Bone reconstruction: from bioceramics to tissue engineering. Expert Review of Medical Devices **2**, 87, 2005.

62.   George, A., Bannon, L., Sabsay, B., Dillon, J.W., Malone, J., Veis, A., Jenkins, N.A., Gilbert, D.J., and Copeland, N.G. The carboxyl-terminal domain of phosphophoryn contains unique extended triplet amino acid repeat sequences forming ordered carboxyl-phosphate interaction ridges that may be essential in the biomineralization process. J Biol Chem **271**, 32869, 1996.

63. Gilbert, M., Shaw, W.J., Long, J.R., Nelson, K., Drobny, G.P., Giachelli, C.M., and Stayton, P.S. Chimeric peptides of statherin and osteopontin that bind hydroxyapatite and mediate cell adhesion. J Biol Chem **275**, 16213, 2000.

64. Stubbs, J.T., 3rd, Mintz, K.P., Eanes, E.D., Torchia, D.A., and Fisher, L.W. Characterization of native and recombinant bone sialoprotein: delineation of the mineral-binding and cell adhesion domains and structural analysis of the RGD domain. J Bone Miner Res **12**, 1210, 1997.

65. Abarrategi, A., Moreno-Vicente, C., Ramos, V., Aranaz, I., Casado, J.V.S., and Lopez-Lacomba, J.L. Improvement of porous beta-TCP scaffolds with rhBMP-2 chitosan carrier film for bone tissue application. Tissue Engineering Part A **14**, 1305, 2008.

66. Le Nihouannen, D., Hacking, S.A., Gbureck, U., Komarova, S.V., and Barralet, J.E. The use of RANKL-coated brushite cement to stimulate bone remodelling. Biomaterials **29**, 3253, 2008.

67. Filion, T.M., Li, X., Mason-Savas, A., Kreider, J.M., Goldstein, S.A., Ayers, D.C., and Song, J. Elastomeric osteoconductive synthetic scaffolds with acquired osteoinductivity expedite the repair of critical femoral defects in rats. Tissue Eng Part A **17**, 503, 2011.

68. Xu, J., Li, X., Lian, J.B., Ayers, D.C., and Song, J. Sustained and localized in vitro release of BMP-2/7, RANKL, and tetracycline from FlexBone, an elastomeric osteoconductive bone substitute. J Orthop Res **27**, 1306, 2009.

69.   Scharnweber, D., Born, R., Flade, K., Roessler, S., Stoelzel, M., and Worch, H. Mineralization behaviour of collagen type I immobilized on different substrates. Biomaterials **25**, 2371, 2004.

70.   Heino, J. The collagen receptor integrins have distinct ligand recognition and signaling functions. Matrix Biology **19**, 319, 2000.

71.   Zhang, H.L., Simpson, D., Kumar, S., and Smart, R.S.C. Interaction of hydroxylated PACVD silica coatings on titanium with simulated body fluid. Colloids and Surfaces a-Physicochemical and Engineering Aspects **291**, 128, 2006.

72.   Murphy, W.L., and Mooney, D.J. Bioinspired growth of crystalline carbonate apatite on biodegradable polymer substrata. Journal of the American Chemical Society **124**, 1910, 2002.

73.   Einhorn, T.A. The cell and molecular biology of fracture healing. Clin Orthop Relat Res, S7, 1998.

74.   Dunn, C.A., Jin, Q.M., Taba, M., Franceschi, R.T., Rutherford, R.B., and Giannobile, W.V. BMP gene delivery for alveolar bone engineering at dental implant defects. Molecular Therapy **11**, 294, 2005.

75.   Little, D.G., McDonald, M., Bransford, R., Godfrey, C.B., and Amanat, N. Manipulation of the anabolic and catabolic responses with OP-1 and zoledronic acid in a rat critical defect model. Journal of Bone and Mineral Research **20**, 2044, 2005.

76.   Gautschi, O.P., Frey, S.P., and Zellweger, R. Bone morphogenetic proteins in clinical applications. ANZ J Surg **77**, 626, 2007.

77.   Ito, H., Koefoed, M., Tiyapatanaputi, P., Gromov, K., Goater, J.J., Carmouche, J., Zhang, X.P., Rubery, P.T., Rabinowitz, J., Samulski, R.J., Nakamura, T., Soballe, K., O'Keefe, R.J., Boyce, B.F., and Schwarz, E.M. Remodeling of cortical bone allografts mediated by adherent rAAV-RANKL and VEGF gene therapy. Nature Medicine **11**, 291, 2005.

78.   Murphy, W.L., Simmons, C.A., Kaigler, D., and Mooney, D.J. Bone regeneration via a mineral substrate and induced angiogenesis. Journal of Dental Research **83**, 204, 2004.

79.   Leach, J.K., Kaigler, D., Wang, Z., Krebsbach, P.H., and Mooney, D.J. Coating of VEGF-releasing scaffolds with bioactive glass for angiogenesis and bone regeneration. Biomaterials **27**, 3249, 2006.

80.   Patel, Z.S., Young, S., Tabata, Y., Jansen, J.A., Wong, M.E.K., and Mikos, A.G. Dual delivery of an angiogenic and an osteogenic growth factor for bone regeneration in a critical size defect model. Bone **43**, 931, 2008.

81.   Oest, M.E., Dupont, K.M., Kong, H.J., Mooney, D.J., and Guldberg, R.E. Quantitative assessment of scaffold and growth factor-mediated repair of critically sized bone defects. J Orthop Res **25**, 941, 2007.

82.   Vehof, J.W.M., Fisher, J.P., Dean, D., van der Waerden, J., Spauwen, P.H.M., Mikos, A.G., and Jansen, J.A. Bone formation in transforming growth factor beta-1-coated porous poly(propylene fumarate) scaffolds. J Biomed Mater Res **60**, 241, 2002.

83.   Israel, D.I., Nove, J., Kerns, K.M., Kaufman, R.J., Rosen, V., Cox, K.A., and Wozney, J.M. Heterodimeric bone morphogenetic proteins show enhanced activity in vitro and in vivo. Growth Factors **13**, 291, 1996.

84.   Zheng, Y.N., Wu, G., Zhao, J., Wang, L.H., Sun, P., and Gu, Z.Y. rhBMP2/7 Heterodimer: An Osteoblastogenesis Inducer of Not Higher Potency but Lower Effective Concentration Compared with rhBMP2 and rhBMP7 Homodimers. Tissue Eng Part A **16**, 879, 2010.

85.   Zhu, W., Kim, J., Cheng, C., Rawlins, B.A., Boachie-Adjei, O., Crystal, R.G., and Hidaka, C. Noggin regulation of bone morphogenetic protein (BMP) 2/7 heterodimer activity in vitro. Bone **39**, 61, 2006.

86.   Zhu, W., Rawlins, B.A., Boachie-Adjei, O., Myers, E.R., Arimizu, J., Choi, E., Lieberman, J.R., Crystal, R.G., and Hidaka, C. Combined bone morphogenetic protein-2 and -7 gene transfer enhances osteoblastic differentiation and spine fusion in a rodent model. Journal of Bone and Mineral Research **19**, 2021, 2004.

87.   Koh, J.T., Zhao, Z., Wang, Z., Lewis, I.S., Krebsbach, P.H., and Franceschi, R.T. Combinatorial gene therapy with BMP2/7 enhances cranial bone regeneration. Journal of Dental Research **87**, 845, 2008.

88.   Kirker-Head, C., Karageorgiou, V., Hofmann, S., Fajardo, R., Betz, O., Merkle, H.P., Hilbe, M., von Rechenberg, B., McCool, J., Abrahamsen, L., Nazarian, A., Cory, E., Curtis, M., Kaplan, D., and Meinel, L. BMP-silk composite matrices heal critically sized femoral defects. Bone **41**, 247, 2007.

89.   Bessa, P.C., Casal, M., and Reis, R.L. Bone morphogenetic proteins in tissue engineering: the road from laboratory to clinic, part II (BMP delivery). J Tissue Eng Regen Med **2**, 81, 2008.

90.   Kolambkar, Y.M., Boerckel, J.D., Dupont, K.M., Bajin, M., Huebsch, N., Mooney, D.J., Hutmacher, D.W., and Guldberg, R.E. Spatiotemporal delivery of bone morphogenetic protein enhances functional repair of segmental bone defects. Bone, 2011.

91.   Barnes, B., Boden, S.D., Louis-Ugbo, J., Tomak, P.R., Park, J.S., Park, M.S., and Minamide, A. Lower dose of rhBMP-2 achieves spine fusion when combined with an osteoconductive bulking agent in non-human primates. Spine **30**, 1127, 2005.

92.   Filion, T.M., Xu, J.W., Prasad, M.L., and Song, J. In vivo tissue responses to thermal-responsive shape memory polymer nanocomposites. Biomaterials **32**, 985, 2011.

93.   Lutolf, M.P., Weber, F.E., Schmoekel, H.G., Schense, J.C., Kohler, T., Muller, R., and Hubbell, J.A. Repair of bone defects using synthetic mimetics of collagenous extracellular matrices. Nat Biotechnol **21**, 513, 2003.

94.   Young, S., Wong, M., Tabata, Y., and Mikos, A.G. Gelatin as a delivery vehicle for the controlled release of bioactive molecules. Journal of Controlled Release **109**, 256, 2005.

95.   Baldwin, A.D., and Kiick, K.L. Polysaccharide-Modified Synthetic Polymeric Biomaterials. Biopolymers **94**, 128, 2010.

96.   Patterson, J., Siew, R., Herring, S.W., Lin, A.S.P., Guldberg, R., and Stayton, P.S. Hyaluronic acid hydrogels with controlled degradation properties for oriented bone regeneration. Biomaterials **31**, 6772, 2010.

97.	Kim, J., Kim, I.S., Cho, T.H., Lee, K.B., Hwang, S.J., Tae, G., Noh, I., Lee, S.H., Park, Y., and Sun, K. Bone regeneration using hyaluronic acid-based hydrogel with bone morphogenic protein-2 and human mesenchymal stem cells. Biomaterials **28**, 1830, 2007.

98.	Engstrand, T., Veltheim, R., Arnander, C., Docherty-Skogh, A.C., Westermark, A., Ohlsson, C., Adolfsson, L., and Larm, O. A novel biodegradable delivery system for bone morphogenetic protein-2. Plast Reconstr Surg **121**, 1920, 2008.

99.	Benoit, D.S.W., and Anseth, K.S. Heparin functionalized PEG gels that modulate protein adsorption for hMSC adhesion and differentiation. Acta Biomater **1**, 461, 2005.

100.	Lutolf, M.P., and Hubbell, J.A. Synthetic biomaterials as instructive extracellular microenvironments for morphogenesis in tissue engineering. Nature Biotechnology **23**, 47, 2005.

101.	Holmes, T.C. Novel peptide-based biomaterial scaffolds for tissue engineering. Trends in Biotechnology **20**, 16, 2002.

102.	Chatterjee, K., Lin-Gibson, S., Wallace, W.E., Parekh, S.H., Lee, Y.J., Cicerone, M.T., Young, M.F., and Simon, C.G. The effect of 3D hydrogel scaffold modulus on osteoblast differentiation and mineralization revealed by combinatorial screening. Biomaterials **31**, 5051, 2010.

103.	Fisher, O.Z., Khademhosseini, A., Langer, R., and Peppas, N.A. Bioinspired Materials for Controlling Stem Cell Fate. Accounts of Chemical Research **43**, 419, 2010.

104.	Srouji, S., Ben-David, D., Lotan, R., Livne, E., Avrahami, R., and Zussman, E. Slow-Release Human Recombinant Bone Morphogenetic Protein-2 Embedded Within

Electrospun Scaffolds for Regeneration of Bone Defect: In Vitro and In Vivo Evaluation. Tissue Eng Part A **17**, 269, 2011.

105. Seyedjafari, E., Soleimani, M., Ghaemi, N., and Shabani, I. Nanohydroxyapatite-Coated Electrospun Poly(L-lactide) Nanofibers Enhance Osteogenic Differentiation of Stem Cells and Induce Ectopic Bone Formation. Biomacromolecules **11**, 3118, 2010.

106. Cho, W.J., Kim, J.H., Oh, S.H., Nam, H.H., Kim, J.M., and Lee, J.H. Hydrophilized polycaprolactone nanofiber mesh-embedded poly(glycolic-co-lactic acid) membrane for effective guided bone regeneration. Journal of Biomedical Materials Research Part A **91A**, 400, 2009.

107. Venugopal, J.R., Dev, V.R.G., Senthilram, T., Sathiskumar, D., Gupta, D., and Ramakrishna, S. Osteoblast mineralization with composite nanofibrous substrate for bone tissue regeneration. Cell Biology International **35**, 73, 2011.

108. Li, C.M., Vepari, C., Jin, H.J., Kim, H.J., and Kaplan, D.L. Electrospun silk-BMP-2 scaffolds for bone tissue engineering. Biomaterials **27**, 3115, 2006.

109. Liao, J.H., Guo, X.A., Nelson, D., Kasper, F.K., and Mikos, A.G. Modulation of osteogenic properties of biodegradable polymer/extracellular matrix scaffolds generated with a flow perfusion bioreactor. Acta Biomater **6**, 2386, 2010.

110. Kolambkar, Y.M., Dupont, K.M., Boerckel, J.D., Huebsch, N., Mooney, D.J., Hutmacher, D.W., and Guldberg, R.E. An alginate-based hybrid system for growth factor delivery in the functional repair of large bone defects. Biomaterials **32**, 65, 2011.

111. Yeo, M., Lee, H., and Kim, G. Three-Dimensional Hierarchical Composite Scaffolds Consisting of Polycaprolactone, beta-Tricalcium Phosphate, and Collagen

Nanofibers: Fabrication, Physical Properties, and In Vitro Cell Activity for Bone Tissue Regeneration. Biomacromolecules **12**, 502, 2011.

112.   Tsuji, K., Bandyopadhyay, A., Harfe, B.D., Cox, K., Kakar, S., Gerstenfeld, L., Einhorn, T., Tabin, C.J., and Rosen, V. BMP2 activity, although dispensable for bone formation, is required for the initiation of fracture healing. Nat Genet **38**, 1424, 2006.

113.   Wang, F.S., Yang, K.D., Kuo, Y.R., Wang, C.J., Sheen-Chen, S.M., Huang, H.C., and Chen, Y.J. Temporal and spatial expression of bone morphogenetic proteins in extracorporeal shock wave-promoted healing of segmental defect. Bone **32**, 387, 2003.

114.   Onishi, T., Ishidou, Y., Nagamine, T., Yone, K., Imamura, T., Kato, M., Sampath, T.K., ten Dijke, P., and Sakou, T. Distinct and overlapping patterns of localization of bone morphogenetic protein (BMP) family members and a BMP type II receptor during fracture healing in rats. Bone **22**, 605, 1998.

115.   Liao, S.S., Cui, F.Z., Zhang, W., and Feng, Q.L. Hierarchically biomimetic bone scaffold materials: Nano-HA/collagen/PLA composite. J Biomed Mater Res Part B **69B**, 158, 2004.

116.   Nair, L.S., Bhattacharyya, S., and Laurencin, C.T. Development of novel tissue engineering scaffolds via electrospinning. Expert Opinion on Biological Therapy **4**, 659, 2004.

117.   Pham, Q.P., Sharma, U., and Mikos, A.G. Electrospinning of polymeric nanofibers for tissue engineering applications: A review. Tissue Engineering **12**, 1197, 2006.

118. Song, J., Xu, J., Filion, T., Saiz, E., Tomsia, A.P., Lian, J.B., Stein, G.S., Ayers, D.C., and Bertozzi, C.R. Elastomeric high-mineral content hydrogel-hydroxyapatite composites for orthopedic applications. J Biomed Mater Res A **89**, 1098, 2009.

119. Fang, J.M., Zhu, Y.Y., Smiley, E., Bonadio, J., Rouleau, J.P., Goldstein, S.A., McCauley, L.K., Davidson, B.L., and Roessler, B.J. Stimulation of new bone formation by direct transfer of osteogenic plasmid genes. Proc Natl Acad Sci U S A **93**, 5753, 1996.

120. Gautschi, O.P., Frey, S.P., and Zellweger, R. Bone morphogenetic proteins in clinical applications. ANZ J Surg **77**, 626, 2007.

121. White, A.P., Vaccaro, A.R., Hall, J.A., Whang, P.G., Friel, B.C., and McKee, M.D. Clinical applications of BMP-7/OP-1 in fractures, nonunions and spinal fusion. International Orthopaedics **31**, 735, 2007.

122. Tang, R.K., Wu, W.J., Haas, M., and Nancollas, G.H. Kinetics of dissolution of beta-tricalcium phosphate. Langmuir **17**, 3480, 2001.

123. Miao, D., and Scutt, A. Histochemical localization of alkaline phosphatase activity in decalcified bone and cartilage. J Histochem Cytochem **50**, 333, 2002.

124. Vanhoof, V.O., and Debroe, M.E. Interpretation and Clinical-Significance of Alkaline-Phosphatase Isoenzyme Patterns. Critical Reviews in Clinical Laboratory Sciences **31**, 197, 1994.

125. Farley, J.R., Hall, S.L., Herring, S., Libanati, C., and Wergedal, J.E. Reference-Standards for Quantification of Skeletal Alkaline-Phosphatase Activity in Serum by Heat Inactivation and Lectin Precipitation. Clinical Chemistry **39**, 1878, 1993.

126.   Schell, H., Lienau, J., Epari, D.R., Seebeck, P., Exner, C., Muchow, S., Bragulla, H., Haas, N.P., and Duda, G.N. Osteoclastic activity begins early and increases over the course of bone healing. Bone **38**, 547, 2006.

127.   Cool, S.M., Forwood, M.R., Campbell, P., and Bennett, M.B. Comparisons between bone and cementum compositions and the possible basis for their layered appearances. Bone **30**, 386, 2002.

128.   Schindeler, A., McDonald, M.M., Bokko, P., and Little, D.G. Bone remodeling during fracture repair: The cellular picture. Semin Cell Dev Biol **19**, 459, 2008.

129.   Lieberman, J.R., Daluiski, A., Stevenson, S., Wu, L., McAllister, P., Lee, Y.P., Kabo, J.M., Finerman, G.A., Berk, A.J., and Witte, O.N. The effect of regional gene therapy with bone morphogenetic protein-2-producing bone-marrow cells on the repair of segmental femoral defects in rats. J Bone Joint Surg Am **81**, 905, 1999.

130.   Kitaori, T., Ito, H., Schwarz, E.M., Tsutsumi, R., Yoshitomi, H., Oishi, S., Nakano, M., Fujii, N., Nagasawa, T., and Nakamura, T. Stromal cell-derived factor 1/CXCR4 signaling is critical for the recruitment of mesenchymal stem cells to the fracture site during skeletal repair in a mouse model. Arthritis Rheum **60**, 813, 2009.

131.   Kidder, L.S., Chen, X., Schmidt, A.H., and Lew, W.D. Osteogenic Protein-1 Overcomes Inhibition of Fracture Healing in the Diabetic Rat: A Pilot Study. Clin Orthop Relat Res, 2008.

132.   Hsu, W.K., Sugiyama, O., Park, S.H., Conduah, A., Feeley, B.T., Liu, N.Q., Krenek, L., Virk, M.S., An, D.S., Chen, I.S., and Lieberman, J.R. Lentiviral-mediated

BMP-2 gene transfer enhances healing of segmental femoral defects in rats. Bone **40**, 931, 2007.

133.   Pelker, R.R., McKay, J., Jr., Troiano, N., Panjabi, M.M., and Friedlaender, G.E. Allograft incorporation: a biomechanical evaluation in a rat model. J Orthop Res **7**, 585, 1989.

134.   Reynolds, D.G., Hock, C., Shaikh, S., Jacobson, J., Zhang, X., Rubery, P.T., Beck, C.A., O'Keefe R, J., Lerner, A.L., Schwarz, E.M., and Awad, H.A. Micro-computed tomography prediction of biomechanical strength in murine structural bone grafts. J Biomech **40**, 3178, 2007.

135.   Baroli, B. From Natural Bone Grafts to Tissue Engineering Therapeutics: Brainstorming on Pharmaceutical Formulative Requirements and Challenges. J Pharm Sci **98**, 1317, 2009.

136.   Blokhuis, T.J., and Lindner, T. Allograft and bone morphogenetic proteins: an overview. Injury **39 Suppl 2**, S33, 2008.

137.   Huang, Z.M., Zhang, Y.Z., Kotaki, M., and Ramakrishna, S. A review on polymer nanofibers by electrospinning and their applications in nanocomposites. Composites Science and Technology **63**, 2223, 2003.

138.   Li, D., and Xia, Y.N. Electrospinning of nanofibers: Reinventing the wheel? Advanced Materials **16**, 1151, 2004.

139.   Uludag, H., Kousinioris, N., Gao, T., and Kantoci, D. Bisphosphonate conjugation to proteins as a means to impart bone affinity. Biotechnol Prog **16**, 258– 267, 2000.

140.   Gittens, S.A., Bagnall, K., Matyas, J.R., Lobenberg, R., and Uludag, H. Imparting bone mineral affinity to osteogenic proteins through heparin-bisphosphonate conjugates. Journal of Controlled Release **98**, 255, 2004.

141.   Katagiri, T., Yamaguchi, A., Komaki, M., Abe, E., Takahashi, N., Ikeda, T., Rosen, V., Wozney, J.M., Fujisawasehara, A., and Suda, T. Bone Morphogenetic Protein-2 Converts the Differentiation Pathway of C2C12 Myoblasts into the Osteoblast Lineage. Journal of Cell Biology **127**, 1755, 1994.

142.   Uludag, H., Golden, J., Palmer, R., and Wozney, J.M. Biotinated bone morphogenetic protein-2: in vivo and in vitro activity. Biotechnol Bioeng **65**, 668– 672, 1999.

143.   Vukicevic, S., Latin, V., Chen, P., Batorsky, R., Reddi, A.H., and Sampath, T.K. Localization of osteogenic protein-1 (bone morphogenetic protein-7) during human embryonic development: high affinity binding to basement membranes. Biochem Biophys Res Commun **198**, 693– 700, 1994.

144.   Irie, A., Habuchi, H., Kimata, K., and Sanai, Y. Heparan sulfate is required for bone morphogenetic protein-7 signaling. Biochem Biophys Res Commun **308**, 858–865, 2003.

145.   Ruppert, R., Hoffmann, E., and Sebald, W. Human bone morphogenetic protein 2 contains a heparin-binding site which modifies its biological activity. Eur J Biochem **237**, 295– 302, 1996.

146.   Takada, T., Katagiri, T., Ifuku, M., Morimura, N., Kobayashi, M., Hasegawa, K., Ogamo, A., and Kamijo, R. Sulfated polysaccharides enhance the biological activities of bone morphogenetic proteins. Journal of Biological Chemistry **278**, 43229, 2003.

147.   Schneiders, W., Reinstorf, A., Biewener, A., Serra, A., Grass, R., Kinscher, M., Heineck, J., Rehberg, S., Zwipp, H., and Rammelt, S. In vivo effects of modification of hydroxyapatite/collagen composites with and without chondroitin sulphate on bone remodeling in the sheep tibia. Journal of Orthopaedic Research, DOI 10.1002/jor.20719, 2008.

148.   Hansson, S., Ostmark, E., Carlmark, A., and Malmstrom, E. ARGET ATRP for Versatile Grafting of Cellulose Using Various Monomers. Acs Applied Materials & Interfaces **1**, 2651, 2009.

149.   Kriegel, C., Arrechi, A., Kit, K., McClements, D.J., and Weiss, J. Fabrication, functionalization, and application of electrospun biopolymer nanofibers. Critical Reviews in Food Science and Nutrition **48**, 775, 2008.

150.   Han, M.-J., and Bhattacharyya, D. Thermal annealing effect on cellulose acetate reverse osmosis membrane structure. Desalination **101**, 195, 1995.

151.   Caplan, A.I. Mesenchymal Stem-Cells. Journal of Orthopaedic Research **9**, 641, 1991.

152.   Friedenstein, A.J., Gorskaja, U.F., and Kulagina, N.N. Fibroblast Precursors in Normal and Irradiated Mouse Hematopoietic Organs. Experimental Hematology **4**, 267, 1976.

153. Prockop, D.J. Marrow stromal cells as steam cells for nonhematopoietic tissues. Science **276**, 71, 1997.

154. Karp, J.M., and Langer, R. Development and therapeutic applications of advanced biomaterials. Curr Opin Biotechnol **18**, 454, 2007.

155. Sokolowski, W., Metcalfe, A., Hayashi, S., Yahia, L., and Raymond, J. Medical applications of shape memory polymers. Biomed Mater **2**, S23, 2007.

156. Xu, J., and Song, J. High performance shape memory polymer networks based on rigid nanoparticle cores. Proc Natl Acad Sci U S A **107**, 7652, 2010.

157. Pearce, A.I., Richards, R.G., Milz, S., Schneider, E., and Pearce, S.G. Animal models for implant biomaterial research in bone: A review. European Cells & Materials **13**, 1, 2007.

158. Williams, D.F. On the mechanisms of biocompatibility. Biomaterials **29**, 2941, 2008.

159. Kannan, R.Y., Salacinski, H.J., Butler, P.E., and Seifalian, A.M. Polyhedral oligomeric silsesquioxane nanocomposites: the next generation material for biomedical applications. Acc Chem Res **38**, 879, 2005.

160. Cutright, D.E., and Hunsuck, E.E. Tissue reaction to the biodegradable polylactic acid suture. Oral Surg Oral Med Oral Pathol **31**, 134, 1971.

161. Athanasiou, K.A., Agrawal, C.M., Barber, F.A., and Burkhart, S.S. Orthopaedic applications for PLA-PGA biodegradable polymers. Arthroscopy **14**, 726, 1998.

162.   Ingham, E., and Fisher, J. Biological reactions to wear debris in total joint replacement. Proceedings of the Institution of Mechanical Engineers Part H-Journal of Engineering in Medicine **214**, 21, 2000.

163.   Baroli, B. From natural bone grafts to tissue engineering therapeutics: Brainstorming on pharmaceutical formulative requirements and challenges. J Pharm Sci **98**, 1317, 2009.

164.   Midwood, K.S., Williams, L.V., and Schwarzbauer, J.E. Tissue repair and the dynamics of the extracellular matrix. Int J Biochem Cell Biol **36**, 1031, 2004.

165.   Ho, E.A., Vassileva, V., Allen, C., and Piquette-Miller, M. In vitro and in vivo characterization of a novel biocompatible polymer-lipid implant system for the sustained delivery of paclitaxel. J Control Release **104**, 181, 2005.

166.   Hoene, A., Walschus, U., Patrzyk, M., Finke, B., Lucke, S., Nebe, B., Schroeder, K., Ohl, A., and Schlosser, M. In vivo investigation of the inflammatory response against allylamine plasma polymer coated titanium implants in a rat model. Acta Biomaterialia **6**, 676.

167.   Hu, W., and Huang, Z.M. Biocompatibility of braided poly(L-lactic acid) nanofiber wires applied as tissue sutures. Polymer International **59**, 92.

168.   Lam, C.X.F., Hutmacher, D.W., Schantz, J.T., Woodruff, M.A., and Teoh, S.H. Evaluation of polycaprolactone scaffold degradation for 6 months in vitro and in vivo. Journal of Biomedical Materials Research Part A **90A**, 906, 2009.

169.   Williams, D.F. A Model for Biocompatibility and Its Evaluation. J Biomed Eng **11**, 185, 1989.

170. Islam, O., Soboleski, D., Symons, S., Davidson, L.K., Ashworth, M.A., and Babyn, P. Development and duration of radiographic signs of bone healing in children. AJR Am J Roentgenol **175**, 75, 2000.

171. Herrmann, M., Klitscher, D., Georg, T., Frank, J., Marzi, I., and Herrmann, W. Different kinetics of bone markers in normal and delayed fracture healing of long bones. Clinical Chemistry **48**, 2263, 2002.

172. Gogolewski, S., Jovanovic, M., Perren, S.M., Dillon, J.G., and Hughes, M.K. Tissue response and in vivo degradation of selected polyhydroxyacids: polylactides (PLA), poly(3-hydroxybutyrate) (PHB), and poly(3-hydroxybutyrate-co-3-hydroxyvalerate) (PHB/VA). J Biomed Mater Res **27**, 1135, 1993.

173. Clearinghouse., N.D.I. National Diabetes Statistics, 2011. National Institute of Diabetes and Digestive and Kidney Diseases; http://diabetes.niddk.nih.gov/dm/pubs/statistics/.

174. Falanga, V. Wound healing and its impairment in the diabetic foot. Lancet **366**, 1736, 2005.

175. Brem, H., and Tomic-Canic, M. Cellular and molecular basis of wound healing in diabetes. J Clin Invest **117**, 1219, 2007.

176. Ekmektzoglou, K.A., and Zografos, G.C. A concomitant review of the effects of diabetes mellitus and hypothyroidism in wound healing. World J Gastroenterol **12**, 2721, 2006.

177. Retzepi, M., and Donos, N. The effect of diabetes mellitus on osseous healing. Clinical Oral Implants Research **21**, 673, 2010.

178. Santana, R.B., Xu, L., Chase, H.B., Amar, S., Graves, D.T., and Trackman, P.C. A role for advanced glycation end products in diminished bone healing in type 1 diabetes. Diabetes **52**, 1502, 2003.

179. Kayal, R., Alblowi, J., McKenzie, E., Krothapalli, N., Silkman, L., Gerstenfeld, L., Einhorn, T.A., and Graves, D.T. Diabetes causes the accelerated loss of cartilage during fracture repair which is reversed by insulin treatment. Bone **44**, 357, 2009.

180. Kayal, R.A., Siqueira, M., Alblowi, J., McLean, J., Krothapalli, N., Faibish, D., Einhorn, T.A., Gerstenfeld, L.C., and Graves, D.T. TNF-alpha Mediates Diabetes-Enhanced Chondrocyte Apoptosis During Fracture Healing and Stimulates Chondrocyte Apoptosis Through FOX01. Journal of Bone and Mineral Research **25**, 1604, 2010.

181. Follak, N., Kloting, I., and Merk, H. Influence of diabetic metabolic state on fracture heating in spontaneously diabetic rats. Diabetes-Metabolism Research and Reviews **21**, 288, 2005.

182. Gandhi, A., Beam, H.A., O'Connor, J.P., Parsons, J.R., and Lin, S.S. The effects of local insulin delivery on diabetic fracture healing. Bone **37**, 482, 2005.

183. Beam, H.A., Parsons, J.R., and Lin, S.S. The effects of blood glucose control upon fracture healing in the BB Wistar rat with diabetes mellitus. J Orthop Res **20**, 1210, 2002.

184. Lu, H.F., Kraut, D., Gerstenfeld, L.C., and Graves, D.T. Diabetes interferes with the bone formation by affecting the expression of transcription factors that regulate osteoblast differentiation. Endocrinology **144**, 346, 2003.

185. Kidder, L.S., Chen, X.Q., Schmidt, A.H., and Lew, W.D. Osteogenic Protein-1 Overcomes Inhibition of Fracture Healing in the Diabetic Rat: A Pilot Study. Clinical Orthopaedics and Related Research **467**, 3249, 2009.

186. Korolkiewicz, R.P., Tashima, K., Fujita, A., Kato, S., and Takeuchi, K. Exogenous insulin-like growth factor (IGF)-1 improves the impaired healing of gastric mucosal lesions in diabetic rats. Pharmacological Research **41**, 221, 2000.

187. Thaller, S.R., Lee, T.J., Armstrong, M., Tesluk, H., and Stern, J.S. Effect of Insulin-Like Growth-Factor Type-1 on Critical-Size Defects in Diabetic Rats. Journal of Craniofacial Surgery **6**, 218, 1995.

188. Galiano, R.D., Tepper, O.M., Pelo, C.R., Bhatt, K.A., Callaghan, M., Bastidas, N., Bunting, S., Steinmetz, H.G., and Gurtner, G.C. Topical vascular endothelial growth factor accelerates diabetic wound healing through increased angiogenesis and by mobilizing and recruiting bone marrow-derived cells. American Journal of Pathology **164**, 1935, 2004.

189. Mordes, J.P., Bortell, R., Blankenhorn, E.P., Rossini, A.A., and Greiner, D.L. Rat models of type 1 diabetes: genetics, environment, and autoimmunity. Institute for Laboratory Animal Research Journal **45**, 278, 2004.

190. Guberski, D.L. Diabetes-Prone and Diabetes-Resistant BB Rats: Animal Models of Spontaneous and Virally Induced Diabetes Mellitus, Lymphocytic Thyroiditis, and Collagen-Induced Arthritis. Institute for Laboratory Animal Research Journal **35**, 29, 1993.

191.   Mckibbin, B. Biology of Fracture Healing in Long Bones. Journal of Bone and Joint Surgery-British Volume **60**, 150, 1978.

192.   Allen, M.R., Hock, J.M., and Burr, D.B. Periosteum: biology, regulation, and response to osteoporosis therapies. Bone **35**, 1003, 2004.

193.   Rubery, P.T. Enhancing Allograft Bone Healing Through Gene Therapy. Spine **35**, 1640, 2010.

194.   Awad, H.A., Zhang, X., Reynolds, D.G., Guldberg, R.E., O'Keefe, R.J., and Schwarz, E.M. Recent advances in gene delivery for structural bone allografts. Tissue Engineering **13**, 1973, 2007.

195.   Breitbart, E.A., Meade, S., Azad, V., Yeh, S., Al-Zube, L., Lee, Y.S., Benevenia, J., Arinzeh, T.L., and Lin, S.S. Mesenchymal Stem Cells Accelerate Bone Allograft Incorporation in the Presence of Diabetes Mellitus. J Orthop Res **28**, 942, 2010.

196.   Golden, J.D., Jones, A.L., Bucholz, R.W., Bosse, M.J., Lyon, T.R., Webb, L.X., and Valentin-Opran, A. Recombinant human BMP-2 and allograft compared with autogenous bone graft for reconstruction of diaphyseal tibial fractures with cortical defects. Journal of Bone and Joint Surgery-American Volume **90A**, 1168, 2008.

197.   Dedania, J., Borzio, R., Paglia, D., Breitbart, E.A., Mitchell, A., Vaidya, S., Wey, A., Mehta, S., Benevenia, J., O'Connor, J.P., and Lin, S.S. Role of Local Insulin Augmentation upon Allograft Incorporation in a Rat Femoral Defect Model. J Orthop Res **29**, 92, 2011.

198.   Yazici, C., Takahata, M., Reynolds, D.G., Xie, C., Samulski, R.J., Samulski, J., Beecham, E.J., Gertzman, A.A., Spilker, M., Zhang, X., O'Keefe, R.J., Awad, H.A., and

Schwarz, E.M. Self-complementary AAV2.5-BMP2-coated Femoral Allografts Mediated Superior Bone Healing Versus Live Autografts in Mice With Equivalent Biomechanics to Unfractured Femur. Mol Ther, 2011.

199.   Chang, D.W., Satterfield, W.C., Son, D., Neto, N., Madewell, J.E., Raymond, A.K., Patrick, C.W., Miller, M.J., Costelloe, C.M., and Weber, K.L. Use of Vascularized Periosteum or Bone to Improve Healing of Segmental Allografts after Tumor Resection: An Ovine Rib Model. Plast Reconstr Surg **123**, 71, 2009.

200.   Zhang, X.P., Xie, C., Lin, A.S.P., Ito, H., Awad, H., Lieberman, J.R., Rubery, P.T., Schwarz, E.M., O'Keefe, R.J., and Guldberg, R.E. Periosteal progenitor cell fate in segmental cortical bone graft transplantations: Implications for functional tissue engineering. Journal of Bone and Mineral Research **20**, 2124, 2005.

201.   Zhao, L., Zhao, J.L., Wang, S.K., Wang, J.S., and Liu, J. Comparative study between tissue-engineered periosteum and structural allograft in rabbit critical-sized radial defect model. Journal of Biomedical Materials Research Part B-Applied Biomaterials **97B**, 1, 2011.

202.   Schneiders, W., Reinstorf, A., Biewener, A., Serra, A., Grass, R., Kinscher, M., Heineck, J., Rehberg, S., Zwipp, H., and Rammelt, S. In Vivo Effects of Modification of Hydroxyapatite/Collagen Composites with and without Chondroitin Sulphate on Bone Remodeling in the Sheep Tibia. J Orthop Res **27**, 15, 2009.

A p p e n d i x I : Survival Responses of Human Embryonic Stem Cells to DNA Damage

This appendix has been adapted from the published manuscript: Filion TM, Qiao M, Ghule PN, Mandeville M, Wijnen AJ, Stein JL, Lian JB, Altieri DC, Stein GS. Survival Responses of Human Embryonic Stem Cells to DNA Damage. *J Cell Physio.* volume: 220, issue: 3, pages 586-592, Sept 2009.

ABSTRACT

Pluripotent human embryonic stem (hES) cells require mechanisms to maintain genomic integrity in response to DNA damage that could compromise competency for lineage-commitment, development and tissue-renewal. The mechanisms that protect the genome in rapidly proliferating hES cells are minimally understood. Human ES cells have an abbreviated cell cycle with a very brief G1 period suggesting that mechanisms mediating responsiveness to DNA damage may deviate from those in somatic cells. Here, we investigated how hES cells react to DNA damage induced by ionizing radiation (IR) and whether genomic insult evokes DNA repair pathways and/or cell death. We find that hES cells respond to DNA damage by rapidly inducing Caspase-3 and -8, phospho-H2AX foci, phosphorylation of p53 on Ser15 and p21 mRNA levels, as well as concomitant cell cycle arrest in G2 based on Ki67 staining and FACS analysis. Unlike normal somatic cells, hES cells and cancer cells robustly express the anti-apoptotic protein Survivin, consistent with the immortal growth phenotype. SiRNA depletion of Survivin diminishes hES survival post-irradiation. Thus, our findings provide insight into pathways and processes that are activated in human embryonic stem cells upon DNA insult to support development and tissue regeneration.

INTRODUCTION

Human embryonic stem (hES) cells are pluripotent progenitors that can produce the three embryonic germ layers and support post-natal tissue renewal. Thus, it is important for these cells to have mechanisms to protect genomic integrity and avoid proliferative defects that may debilitate development or cause lethality. Human ES cells exhibit an abbreviated cell cycle due to a brief G1 period (Becker et al, 2006). These cells lack a traditional Restriction point in late G1 (reviewed in (Blagosklonny and Pardee, 2002)), but maintain stringent control of histone gene expression at the G1/S phase transition (Becker et al, 2007). Regulatory mechanisms for transcriptional control at the onset of S phase are operative. The regulatory machinery for histone gene expression is spatially organized in discrete foci immediately following completion of mitosis (Ghule et al, 2007), and this organization is distinct from that observed in normal somatic cells (Ghule et al, 2008) or tumor cells (Ghule et al, 2009). Human ES cells exhibit a robust induction of components of the DNA damage response (Becker et al, 2007), but mechanisms that mediate cell survival have not been examined.

The pathways controlled by the ataxia telangiectasia-mutated (ATM) and ATM-related (ATR) proteins represent the principal pathways by which cells react to DNA damage in somatic cells. ATM is activated upon γ-ionizing radiation (IR)-induced DNA double strand breaks, phosphorylates p53 on serine 15, followed by upregulation of p21 mRNA levels in somatic human cells (reviewed in (Gartel and Radhakrishnan, 2005)). This induction of p21 mRNA has also been observed in hES cells (Becker et al, 2007),

suggesting that hES cells are capable of blocking CDK levels to ensure a cell cycle arrest. A key question that remains to be addressed is how hES cells regulate cell survival following DNA damage and whether the cell cycle is inhibited. Although DNA damage response mechanisms have been examined in mouse ES cells (Aladjem et al, 1998; Lavin and Kozlov, 2007; Schmidt-Kastner et al, 1998; Hong and Stambrook, 2004; Hirao et al, 2000), mouse and human cells differ in their ability to be immortalized and thus survival mechanisms may be fundamentally distinct.

In somatic cells, mechanisms are operative that enable cells to stop cell cycle progression and to make molecular decisions to repair DNA and promote cell survival, or to undergo apoptosis to ensure genomic integrity within the organism (reviewed in (Altieri, 2008b; Altieri, 2008a; Salz et al, 2005; Luo and Altieri, 2008)). ES cells exhibit an immortalized phenotype that resembles the growth phenotype of cancer cells, which prevent apoptosis through induction of the anti-apoptotic protein survivin, while normal somatic cells have minimal survivin expression (Altieri, 2006; Altieri, 2003). In this study, we have characterized the cell survival response of human ES cells following IR-induced DNA damage, in relation to expression of survivin. Using a combination of biochemical and cellular approaches, we show that DNA-damaged human ES cells have decreased cell survival, are able to block in the G2 phase of the cell cycle, have a functionally activated ATM pathway, and express survivin.

MATERIALS AND METHODS

Cell lines and Irradiation

The H1 hES line (WA01, WiCell Research Institute, Madison, WI; http://www.wicell.org/) was used in this study. The control cell lines WI-38 (normal somatic lung fibroblast) and MDA-MB-231 (metastatic breast cancer) were used for comparison. A ^{137}Cs source irradiator was used to apply 5 Gy of IR to the cells.

H1 Cell Culture Conditions

Human embryonic stem (hES) cells were cultured under non-differentiating conditions according to WiCell Research Institute (Madison, WI) protocols in hES cell culture medium (80% DMEM/F12, 20% KnockOut-Serum Replacement, 2 mM L-glutamine, 1% non-essential amino acids (NEAA), 0.1 mM 2-mercaptoethanol (all from Invitrogen, Carlsbad, CA), 4 ng/mL basic fibroblast growth factor (R+D Systems, Minneapolis, MN)) at 37 ºC, 5% CO_2 and high humidity. Irradiated mouse embryonic fibroblasts (iMEF), isolated from day 13.5 embryos of CF-1 mice (Charles River Laboratories, Wilmington, MA), were used as feeder cells for the H1 culture. iMEFs were cultured until passage 3 in DMEM (Hyclone, Logan, UT) supplemented with 10% heat inactivated fetal bovine serum (Hyclone) and 1% NEAA (Invitrogen). Cells were then mitotically inactivated by irradiation at 5 Gy (Cesium 137) before seeding on a 0.1% Type A gelatinized (Sigma, St. Louis, MO) 6-well place at 1.75×10^6 cells/plate.

At approximately 80% confluence (day 6) the H1 culture was collected using Collagenase Type IV (Invitrogen) at a concentration of 1 mg/mL. This solution (1 mL)

was added to each well of a 6-well plate and incubated at 37°C and 5% CO_2 for 5 min. When the edges of the hES cell colonies began to detach, the plate was removed from the incubator and transferred to a sterile biological safety cabinet. The collagenase was removed and 2 mL fresh hES cell culture medium was added to each well. A 5 mL glass pipette was used to further dislodge the H1 colonies from the plate and the contents of each well were collected and transferred to a sterile 50 mL conical tube. Fresh hES cell culture medium (3 mL) was used to rinse any remaining cells from the wells and was added to the same tube. The cells were centrifuged at 1000 rpm and 23°C for 5 min, after which the supernatant was removed and the pellet was resuspended in 24 mL fresh hES cell culture medium.

After removing the iMEF culture medium from new feeder cells and rinsing with 2 mL/well Dulbecco's Phosphate Buffered Saline without calcium and magnesium chloride (Invitrogen), each well was preloaded with 1.5 mL fresh hES cell culture medium, followed by the addition of 1 mL of the H1 suspension previously collected. This 1:4 seeding ratio provided two 6-well plates at approximately 15% confluence 24 h later. At this time, the exhausted hES cell culture medium was removed and replaced with 2.5 mL/well fresh medium. This procedure was repeated at 48 and 72 h, concluding with the H1 cell irradiation 2 h after the final feeding (day 3).

Survival and Apoptotic Activity

Adherent H1 cells were collected at 0 h without IR and at 7 h both with and without IR and stained with Trypan Blue to determine H1 survival post-IR. Caspase-3 and 8

activities were then measured via colorimetric enzyme activation assays (Chemicon/Millipore, Billerica, MA) at 0 h without IR and at 2, 3, and 4 h time points with IR to examine activation of apoptotic pathways according to the manufacturer specifications.

Flow Cytometry

H1 cells were collected at 0, 2, and 7-h, with IR at 2 and 7 h and without IR at 0 and 7 h and processed for cell cycle flow cytometry to examine cell cycle distribution. Cells were trypsinized, washed with phosphate-buffered saline, fixed in 95% ethanol overnight at 4°C, stained with propidium iodide and analyzed using FACSCalibur (Becton, Dickinson Biosciences, San Jose, CA) and ModFit software (Verity Software House, Topsham, ME).

Protein Analysis

Protein and immunohistochemistry samples were collected at 2, 7, 14 and 24 h time points after IR, with unirradiated controls also being collected at 0, 7 and 24 h. Protein was used to analyze by western blot analysis the ATM pathway-related proteins γH2A.X (Upstate/Millipore, Billerica, MA), p53 (Santa Cruz, Santa Cruz, CA), p53 ser15 (Cell Signaling, Danvers, MA), p21 (Santa Cruz), and Chk2 ser68 (Cell Signaling), as well as survivin (Novus Biologicals, Littleton, CO). Alpha tubulin (Santa Cruz) was used as an internal control. Immunohistochemistry was used to analyze γH2A.X, p53 ser-16, and Ki67 (Abcam, Cambridge, MA). Ki67 yields staining patterns specific to different

phases of the cell cycle and was used to determine whether H1 cells block in cell cycle in response to IR to support flow cytometry data.

Reverse transcription-quantitative PCR (RT-qPCR)

mRNA levels were analyzed as described previously described (Becker et al, 2007). Briefly, total mRNA was extracted from hES cells using TRIzol reagent according to the manufacturer specifications (Invitrogen) and subjected to DNase I digestion, followed by column purification using the DNA Free RNA Kit (Zymo Research, Orange, CA). Reverse transcription was performed using iScript cDNA synthesis kit (Bio-Rad Laboratories, Hercules, CA). Quantification was performed on ABI PRISM 7000 sequence detection system with SYBR Green supermix (Applied Biosystems, Foster City, CA). Human-specific p21 sequence was used as previously reported (Becker et al, 2007). Mitochondrial cytochrome c oxidase *(*m-COX) was used as an internal control (reverse: 5'-CGG GAA TTG CAT CTG TTT TT-3', forward: 5'-GGC CAC CAA TGG TAC TGA AC-3').

Cell Proliferation Assay

An MTS [3-(4,5-dimethylthiazol-2-yl)-5-(3-carboxymethoxyphenyl)-2-(4-sulfophenyl)-2H-tetrazolium, inner salt] assay was used to analyze cell viability. For each time point, H1 cells in a 6-well plate were washed with PBS twice. The total number of surviving cells was assessed by determining the absorbance at A490 nm of the dissolved formazan

product after addition of MTS for 1 h, as described by the manufacturer (Promega, Madison, WI).

siRNA Transfection

Twenty-four hours before transfection, 70-80% confluent H1 cells were split 1:5 and plated on top of MEF cells in a 6-well plate. Cells were transfected with oligofectamin (Invitrogen) according to the manufacture's instruction. The final concentration of control or survivin siRNA is 50 nM. The medium was replaced 6 h later, and the cells were analyzed for survivin expression 48 h after transfection.

RESULTS

Survival of human ES cells is significantly decreased by ionizing radiation

To address cell survival of human ES cells in response to DNA damage, we initially determined the number of viable adherent H1 human ES cells following γ radiation (5 Gy). IR treatment of human ES cells decreases cell viability by approximately 65% at 7 h after treatment (Fig. 1A). Populations of adherent cells at 2, 3 and 4 h were subjected to molecular analyses of pathways activated in response to IR. The induction of apoptotic mechanisms was monitored by assessing the activities of Caspase-3 and Caspase-8 (Fig. 1B). While both Caspase-3 and -8 are induced by ~2 fold

at 2 h post-radiation, Caspase-3 levels remain modestly elevated at 3 and 4 h, while Caspase-8 levels continue to increase to ~9-10 fold over control levels by 4 h. Thus, at 4 h after DNA damage, mechanisms supporting programmed cell death have been initiated (Fig. 1A).
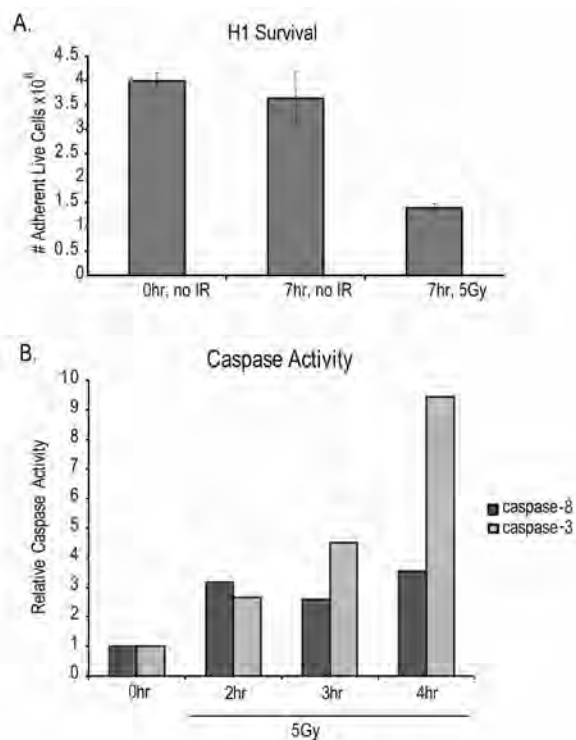
Fig. 1. Decreased cell survival of human ES cells upon γ-irradiation. A. Survival of H1 cells was determined by assessing the number of adherent live cells (as determined by trypan blue staining) per well of a 6-well plate before and at 7 h after IR with 5 Gy. Values represent the average of three determinations within a representative experiment and the error bars are based on the standard error. B. Induction of apoptosis was determined by monitoring the activities of Caspase-3 and Caspase-8 by enzymatic assays at 2, 3 and 4 h after IR. Values represent the average of sample duplicates. Standard error was determined, but this error is minimal and not readily visible in the graph).

**Human ES cells arrest in G2 upon γ-irradiation**

To determine whether human ES cells are capable of blocking cell cycle progression after IR, we used a combination of Ki67 nuclear staining and cell cycle analysis by flow cytometry. Ki67 immunofluorescence staining gives distinct nuclear patterns for different stages of the human ES cell cycle (Solovei et al, 2005; Becker et al, 2006; Ghule et al, 2007). Using Ki67, we find that H1 human ES cell populations are deficient for both G1 and M phase cells after irradiation (Fig. 2A). For example, mitotic cells represent ~5% of the actively proliferating population that did not receive radiation but are undetectable at 2 h after irradiation, indicating that irradiation prevents new mitotic divisions. Mitotic cells gradually increase during the subsequent time-points (7, 14 and 24 h) as cells recover from DNA damage and resume mitosis (Fig.2A). Consistent with an irradiation induced cell cycle block by 2 h, we find that the distribution of cells in late G1 and S versus G2 phase is significantly altered (Fig. 2A). The disappearance of G1 and M phase cells, along with increased representation of cells in G2 (at 2 hr), suggests a block in the G2 phase of the cell cycle.

Given the abbreviated G1 period in human ES cells and the Ki67 nuclear staining patterns we observed, the possibility arises that these pluripotent cells may not undergo a G1 block upon IR and may move into S phase or undergo cell death. To examine this possibility, we performed cell cycle analysis by flow cytometry. At 2 h post irradiation there is evidence of significant cell death as indicated by the accumulation of a sub-G1 cell population (Fig. 2B). The data reveal an increase of G2 cells after IR, with 14% before irradiation increasing to 24% by 7 h after irradiation. These data are consistent

with the findings obtained with Ki67 (see Fig. 2A) and indicate that DNA-damaged hES

cells can undergo apoptosis and/or arrest in G2.

Fig. 2. γ-Irradiation induces a G2 phase related cell cycle arrest in human ES cells. A. Immunofluorescence microscopy was used to examine Ki67 staining patterns (n=200; bar graph in upper portion), which reflect different stages of the cell cycle (lower portion), as a time-course after γ-irradiation (5 Gy). Values represent the average of three independent determinations of 200 cells per sample within a representative experiment and the error bars are based on the standard error. B. Fluorescence activated cell sorting was used to assess the distribution of hES cells in different cell cycle stages following γ-irradiation. We note that the fraction of cells in G1 may be over-estimated due to the presence of inactivated mouse embryonic fibroblasts that are arrested in G1.
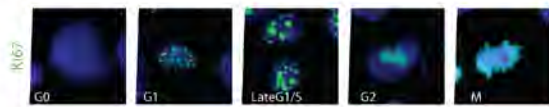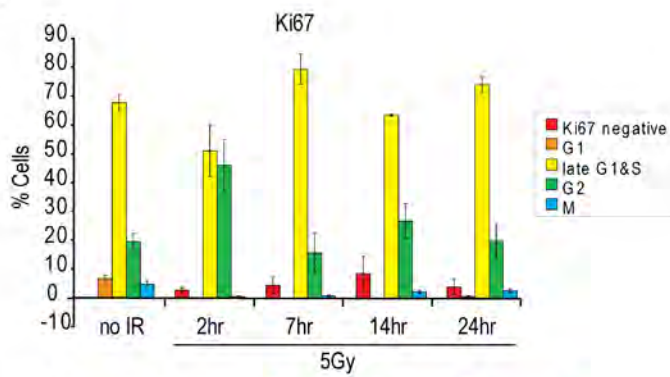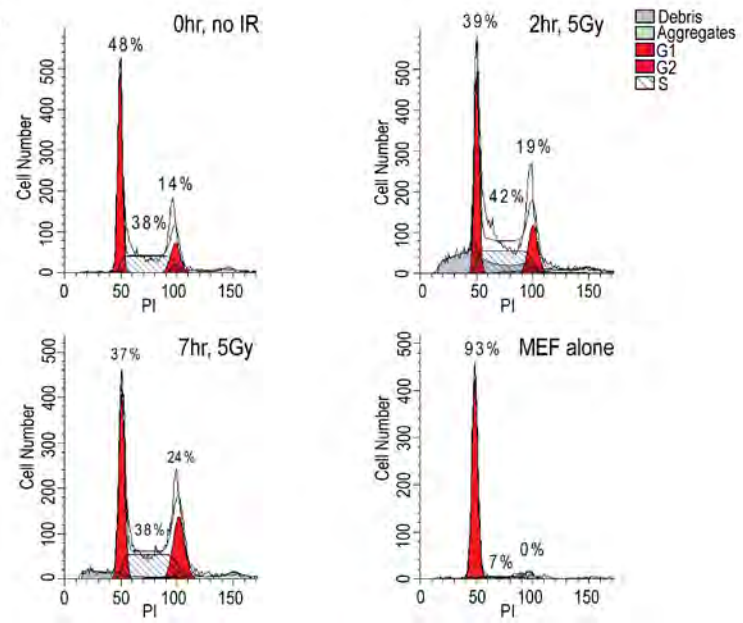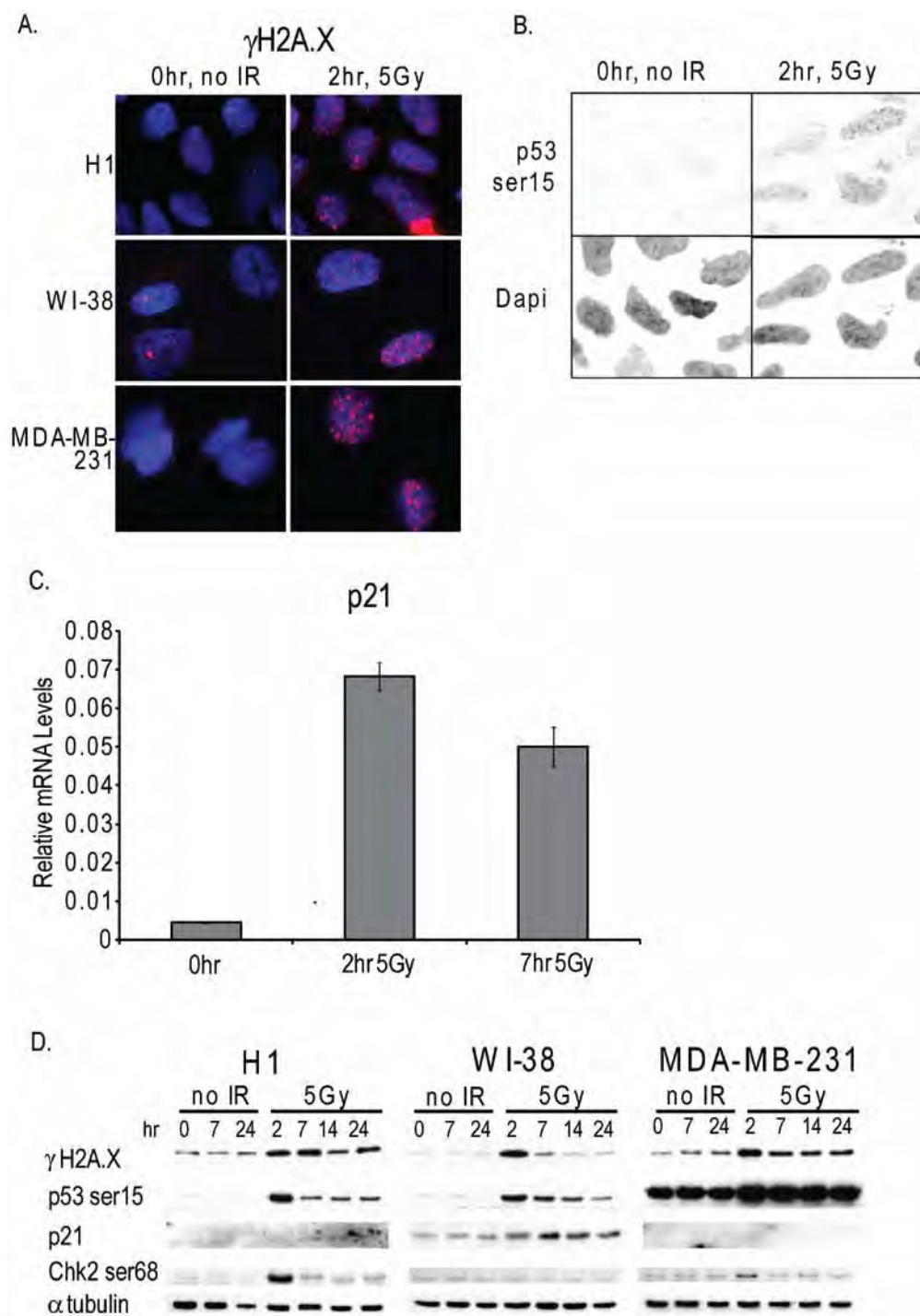
The ATM pathway is activated in human ES cells in response to IR

To determine if the ATM pathway is functionally activated in human ES cells in response to IR, we analyzed several major components of the ATM pathway. Immunofluorescence microscopy reveals that irradiated human ES cells have an increased number of foci containing ATM-phosphorylated H2A.X (γH2A.X foci), which reflect double-stranded DNA breaks (Fig. 3A), as well as an increase of p53 phosphorylated on serine 15 (Fig. 3B). This activation of p53 occurs within 2 h after IR and results in approximately 15-fold upregulation of p21 mRNA levels (Fig. 3C). Western blot analysis of ATM pathway-related proteins corroborates the immunofluorescence data (Fig. 3D). For example, γH2A.X, p53-phosphoSer15, and Chk2-phosphoSer68 are all increased by 2 h after IR. Although phosphorylation of p53 and Chk2 has subsided by 7 h, phosphorylation of H2A.X is sustained until at least 24 h. This transient induction of phospho-Chk2 in hES cells is consistent with the observed G2/M block at 2 h and its partial resolution by 7 h after IR based on Ki67 staining (see Fig. 2A). Interestingly, p21 protein levels in hES cells are barely elevated post-irradiation (Fig.3D) despite a robust induction at the mRNA level (see Fig. 3C). Thus, H1 human ES cells exhibit an activated ATM pathway after IR treatment.

Fig. 3.   Activation of the ATM pathway activation by IR in hES cells. A. Immunofluorescence microscopy was used to examine the in situ appearance of γH2A.X foci (red), which reflect phosphorylation of H2A.X by ATM at sites of double-stranded DNA breaks after IR.   Nuclei were stained with DAPI (blue).   B. Same as A, but assessing phosphorylation of p53 at Ser-15 (dark gray in upper panels) by in situ immunofluorescence microscopy after IR. C. Quantitative real-time PCR analysis was used to show that in situ activation of the ATM pathway after IR results in the expected p53 mediated induction of p21 mRNA levels at 2 and 7 h after radiation with 5 Gy. Error bars represent standard deviation of sample duplicates.   D. Western blot analysis was used to show activation of components of the ATM pathway in human H1 embryonic stem cells, normal diploid WI-38 fibroblasts and MDA-MB-231 breast cancer cells upon γ-irradiation. Blots were prepared with antibodies probing ATM dependent phosphorylation of H2A.X (γH2A.X) and Ser-15 phosphorylation of p53, as well as the levels of the CDK inhibitor p21 and Chk2, using α-tubulin as an internal control for protein loading.

A. γH2A.X

B.

C. p21

D. H1   WI-38   MDA-MB-231

The DNA damage response of human ES cells differs from responses in somatic cells

The DNA damage response has been well characterized in both normal somatic and tumor-derived human cells. Therefore we compared activation of the ATM pathway in H1 embryonic stem cells with normal diploid WI-38 fibroblasts and MDA-MB-231 breast cancer cells (Fig. 3A and 3D). Notably, γH2A.X protein levels in both H1 and MDA-MB-231 cells decrease more slowly than in normal somatic WI-38 cells, indicating possible delay in or decreased ability to repair double-stranded DNA breaks. In contrast, p53 phosphorylation peaks by 2 h and decreases by 7 h after IR in both H1 and WI-38 cells, while elevated p53 phosphorylation is maintained for at least 24 h in MDA-MB-231 cells, perhaps due in part to high basal levels of phospho-p53. Chk2-Ser-68 phosphorylation is transiently induced at 2 h in both H1 and MDA-MB-231 cells but not detectable in WI-38 cells under our experimental conditions. Protein levels of p21 are barely detectable in irradiated H1 cells, while p21 is clearly detected and induced by p53 activation as expected in WI-38 cells; p21 is not expressed in the tumor-derived MDA-MB-231 cells. Taken together, these results indicate both differences and similarities in the molecular mechanisms by which human ES cells mitigate deleterious effects of DNA damage compared to normal and tumor-derived somatic cells.
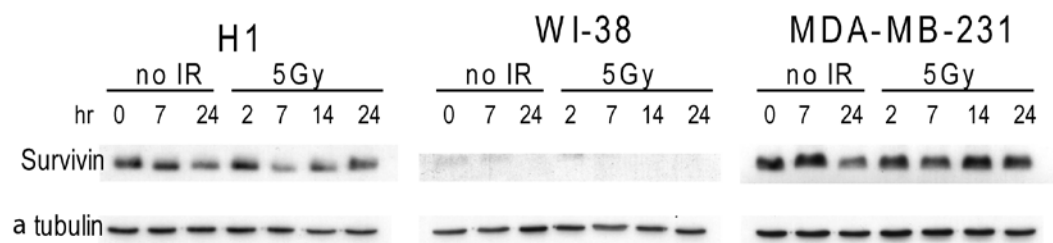
Expression and siRNA-mediated depletion of survivin during the DNA damage response in human ES cells

Both control and irradiated H1 human embryonic stem cells have substantial levels of survivin, although at lower levels than in MDA-MB-231 cancer cells, as
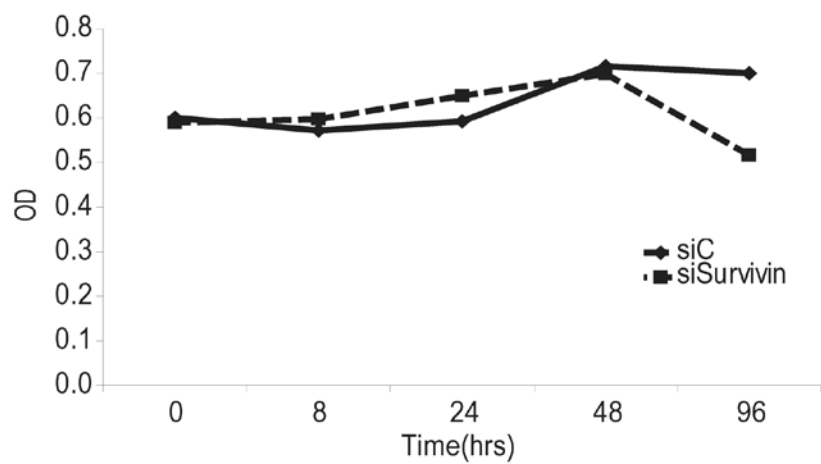
determined by western blot analysis (Fig. 4A). These high levels of survivin that are indicative of resistance to apoptosis are largely sustained for at least 24 h in both cell types, but survivin is not detected in WI-38 fibroblasts irrespective of irradiation. Although levels of survivin are significantly lower in pluripotent human ES cells following subcultivation, there is a stress induced response (data not shown). To test whether survivin is required for hES cell survival after induction of DNA damage, we generated survivin-depleted ES cells using RNA interference. Survivin siRNA treatment results in a >3-fold decrease in survivin protein levels in non-irradiated cells (Figs. 4B and 4C). This reduction in survivin levels does not impinge on survival during the first 24 h after IR (Fig. 4B), but appears to reduce cell fitness modestly at later times (96 h) (Fig. 4C). We conclude that survivin is at least in part dispensable for hES cell survival after gamma radiation, suggesting a novel role in human ES related regulatory mechanisms.

Fig. 4. Expression and function of survivin upon γ-irradiation in human ES cells. A. Western blot analysis was used to monitor survivin protein levels in human H1 embryonic stem cells, normal diploid WI-38 fibroblasts and MDA-MB-231 breast cancer cells upon γ-irradiation (5 Gy) at the indicated time-points. Levels of α-tubulin were determined as an internal control for protein loading. B and C. Effect of siRNA-mediated depletion of survivin during the DNA damage response in human ES cells. Cells were transfected with either control or survivin siRNA for 48 hours and then exposed to 5Gy of γ-irradiation. B. Cell survival was measured by MTS assay as function of time after treatment. C. siRNA treatment is effective as revealed by reduced survivin levels throughout a 96 h time course after IR.

A.

H1   WI-38   MDA-MB-231
no IR   5Gy   no IR   5Gy   no IR   5Gy
hr   0   7 24   2   7 14 24   0   7 24   2   7 14 24   0   7 24   2   7 14 24

Survivin

a tubulin

B.

C.

siC   siSurvivin

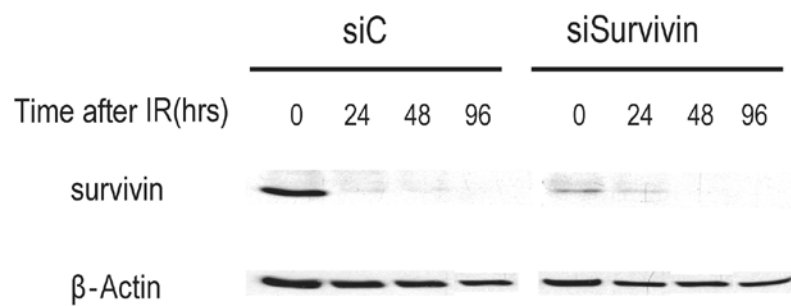Time after IR(hrs)   0   24   48   96   0   24   48   96

survivin

β-Actin

DISCUSSION

In this study we have shown that human ES cells lack a G1 checkpoint in response to ionizing radiation. We find that the ATM pathway is activated in hES cells in response to IR, but there is essentially no p21 protein to support a cell cycle arrest. However, these cells activate Chk2 and express survivin, thus providing p21-independent mechanisms to recuperate from DNA-damage.

Following DNA damage human ES cells will not divide but instead initiate apoptosis. Indeed, we find that the majority of hES cells are undergoing cell death via Caspase-related mitochondrial apoptosis following induction of DNA damage. This apoptotic mechanism may ensure that genomic integrity is not compromised in human ES cells. Our results show that surviving human ES cells enter a cell cycle block after IR. Human ES cells do not arrest in G1, but block in the G2 phase of the cell cycle.

The induction of p53 phosphorylation in response to IR would be expected to inhibit survivin expression through a direct mechanism of transcriptional repression (Dumaz and Meek, 1999). Survivin is a well characterized downstream target of p53, which is transcriptionally silenced in a pathway that may enhance p53-dependent apoptosis. Given that it is unclear how survivin is regulated after IR in ES cells, this response may involve post-transcriptional mechanisms that include protein stabilization and reduced destruction.

The strong induction of Chk2 in response to DNA damage in the hES cells is consistent with previous studies that Chk2 activation induces survivin expression in

tumor cells (Ghosh et al, 2006). This was not a transcriptional response but a redistribution of survivin from mitochondria into the cytosol. The response may contribute to inhibition of apoptosis after IR and may be analogous to the response we observe with the human ES cells.

Survivin is expressed in hES cells, but its depletion does not have a major impact on hES cell survival after DNA damage. This finding suggests that survivin may perform another function that is not necessarily coupled to canonical cell survival pathways. Survivin function is associated with inhibition of mitochondrially-mediated and Caspase-related programmed cell death (Altieri, 2008b; Altieri, 2008a; Salz et al, 2005; Luo and Altieri, 2008; Altieri, 2006; Altieri, 2003). Recent studies have shown that Caspases are transiently expressed in human ES cells during the transition when ES cells relinquish pluripotency and initiate lineage commitment (Abdul-Ghani and Megeney, 2008; Janzen et al, 2008; Fujita et al, 2008). This increased Caspase activity is required to degrade the complement of transcription factors that establish and/or sustain the pluripotent state. The possibility arises that survivin may attenuate the activity of Caspases to permit cell survival while allowing the degradation of the regulatory factors that determine stemness.

In this study we have revealed some of the previously unknown fundamental differences between human ES cells and normal somatic cells in response to IR. We have shown that human ES cells lack a G1 checkpoint and have a p21–independent G2 checkpoint. Further elucidation of the mechanisms governing the G2 checkpoint in human ES cells will give us insight into how these cells are protecting their genomic integrity. In addition, our data suggest that human ES cells may invoke a novel role for

survivin. Dissecting the role of survivin in human ES cells may contribute to understanding mechanisms associated with cellular differentiation.

ACKNOWLEDGMENTS

REFERENCES

Abdul-Ghani M, Megeney LA. 2008. Rehabilitation of a contract killer: caspase-3 directs stem cell differentiation. Cell Stem Cell 2:515-516.

Aladjem MI, Spike BT, Rodewald LW, Hope TJ, Klemm M, Jaenisch R, Wahl GM. 1998. ES cells do not activate p53-dependent stress responses and undergo p53-independent apoptosis in response to DNA damage. Curr Biol 8:145-155.

Altieri DC. 2003. Survivin, versatile modulation of cell division and apoptosis in cancer. Oncogene 22:8581-8589.

Altieri DC. 2006. The case for survivin as a regulator of microtubule dynamics and cell-death decisions. Curr Opin Cell Biol 18:609-615.

Altieri DC. 2008a. New wirings in the survivin networks. Oncogene 27:6276-6284.

Altieri DC. 2008b. Survivin, cancer networks and pathway-directed drug discovery. Nat Rev Cancer 8:61-70.

Becker KA, Ghule PN, Therrien JA, Lian JB, Stein JL, van Wijnen AJ, Stein GS. 2006. Self-renewal of human embryonic stem cells is supported by a shortened G1 cell cycle phase. J Cell Physiol 209:883-893.

Becker KA, Stein JL, Lian JB, van Wijnen AJ, Stein GS. 2007. Establishment of histone gene regulation and cell cycle checkpoint control in human embryonic stem cells. J Cell Physiol 210:517-526.

Blagosklonny MV, Pardee AB. 2002. The restriction point of the cell cycle. Cell Cycle 1:103-110.

Dumaz N, Meek DW. 1999. Serine15 phosphorylation stimulates p53 transactivation but does not directly influence interaction with HDM2. EMBO J 18:7002-7010.

Fujita J, Crane AM, Souza MK, Dejosez M, Kyba M, Flavell RA, Thomson JA, Zwaka TP. 2008. Caspase activity mediates the differentiation of embryonic stem cells. Cell Stem Cell 2:595-601.

Gartel AL, Radhakrishnan SK. 2005. Lost in transcription: p21 repression, mechanisms, and consequences. Cancer Res 65:3980-3985.

Ghosh JC, Dohi T, Raskett CM, Kowalik TF, Altieri DC. 2006. Activated checkpoint kinase 2 provides a survival signal for tumor cells. Cancer Res 66:11576-11579.

Ghule PN, Becker KA, Harper JW, Lian JB, Stein JL, van Wijnen AJ, Stein GS. 2007. Cell cycle dependent phosphorylation and subnuclear organization of the histone gene regulator p220^{NPAT} in human embryonic stem cells. J Cell Physiol 213:9-17.

Ghule PN, Dominski Z, Lian JB, Stein JL, van Wijnen AJ, Stein GS. 2009. The subnuclear organization of histone gene regulatory proteins and 3' end processing factors of normal somatic and embryonic stem cells is compromised in selected human cancer cell types. J Cell Physiol [Epub ahead of print].

Ghule PN, Dominski Z, Yang XC, Marzluff WF, Becker KA, Harper JW, Lian JB, Stein JL, van Wijnen AJ, Stein GS. 2008. Staged assembly of histone gene expression machinery at subnuclear foci in the abbreviated cell cycle of human embryonic stem cells. Proc Natl Acad Sci U S A 105:16964-16969.

Hirao A, Kong YY, Matsuoka S, Wakeham A, Ruland J, Yoshida H, Liu D, Elledge SJ, Mak TW. 2000. DNA damage-induced activation of p53 by the checkpoint kinase Chk2. Science 287:1824-1827.

Hong Y, Stambrook PJ. 2004. Restoration of an absent G1 arrest and protection from apoptosis in embryonic stem cells after ionizing radiation. Proc Natl Acad Sci U S A 101:14443-14448.

Janzen V, Fleming HE, Riedt T, Karlsson G, Riese MJ, Lo CC, Reynolds G, Milne CD, Paige CJ, Karlsson S, Woo M, Scadden DT. 2008. Hematopoietic stem cell responsiveness to exogenous signals is limited by caspase-3. Cell Stem Cell 2:584-594.

Lavin MF, Kozlov S. 2007. ATM activation and DNA damage response. Cell Cycle 6:931-942.

Luo J, Altieri DC. 2008. SIRTing through breast cancer is just a survivin' game. Mol Cell 32:159-160.

Salz W, Eisenberg D, Plescia J, Garlick DS, Weiss RM, Wu XR, Sun TT, Altieri DC. 2005. A survivin gene signature predicts aggressive tumor behavior. Cancer Res 65:3531-3534.

Schmidt-Kastner PK, Jardine K, Cormier M, McBurney MW. 1998. Absence of p53-dependent cell cycle regulation in pluripotent mouse cell lines. Oncogene 16:3003-3011.

Solovei I, Schermelleh L, Albiez H, Cremer T. 2005. Detection of the cell cycle stages in situ in growing cell populations. In: Celis J, editor. Cell Biology Handbook: A Laboratory Manual.San Diego:Academic Press NYP.

Appendix II: Publications completed during graduate education

Song J, Xu J, <u>Filion T</u>, Saiz E, Tomsia AP, Lian JB, Stein GS, Ayers DC, Bertozzi CR. Elastomeric high-mineral content hydrogel-hydroxyapatite composites for orthopedic applications. *J Biomed Mater Res A*., volume: 89A, Issue: 4, pages 1098-1107, Jun 2009.

<u>Filion TM</u>, Li X, Kreider JM, Goldstein SA, Ayers DC, Song J. A Synthetic Alternative to Structural Bone Allograft. Elastomeric osteoconductive synthetic scaffolds with acquired osteoinductivity expedite the repair of critical femoral defects in rats. *Tissue Eng. Part A*, volume: 17, issue: 3-4, pages 503-511, 2011.

<u>Filion TM</u>, XU J, Prasad ML and Song J. In vivo tissue responses to thermal-responsive shape memory polymer nanocomposites. *Biomaterials*, volume: 32, issue: 4, pages 985-991, 2011.

<u>Filion TM</u>, Kutikov A, Song J. Chemically modified cellulose fibrous meshes for use as tissue engineering scaffolds. *Bioorg Med Chem Lett.*, volume: 21, issue: 17, pages 5067-70, 2011.

Filion TM and Song J. Scalable Functional Bone Substitutes: Strategic Integration of Key Structural Elements of Bone in Synthetic Biomaterials, Biomedical Engineering - Frontiers and Challenges, Reza Fazel-Rezai (Ed.), ISBN: 978-953-307-309-5, InTech, 2011.

Filion TM, Qiao M, Ghule PN, Mandeville M, Wijnen AJ, Stein JL, Lian JB, Altieri DC, Stein GS. Survival Responses of Human Embryonic Stem Cells to DNA Damage. *J Cell Physio.* volume: 220, issue: 3, pages 586-592, 2009.

Xu J, Filion TM, Prifti F, Song J. Cytocompatible Poly(ethylene glycol)-co-polycarobonate Hydrogels Crosslinked by Copper-free, Strain-promoted "Click" Chemistry. *Chem Asian J.* 2011 (in press).

Li X, Xu J, Filion TM, Ayers DC, Song J. Sustained and Localized *In Vitro* Release of Vancomycin and Human Recombinant Bone Morphogenetic Protein-2 (rhBMP-2) from an Osteoconductive Synthetic Bone Substitute. *J Bone Joint Surg Am* (to be submitted).